12-2023

Synergistic strategies in sinter-based material extrusion (MEX) 3D printing of copper: process development, product design, predictive maps and models.

SYNERGISTIC STRATEGIES IN SINTER-BASED MATERIAL EXTRUSION (MEX) 3D PRINTING OF COPPER: PROCESS DEVELOPMENT, PRODUCT DESIGN, PREDICTIVE MAPS AND MODELS

By

Kameswara Pavan Kumar Ajjarapu

A Dissertation
Submitted to the Faculty of the
J.B. Speed School of Engineering of the University of Louisville
in Fulfilment of the Requirements
for the Degree of

Doctor of Philosophy
in Mechanical Engineering

Department of Mechanical Engineering
University of Louisville
Louisville, Kentucky, United States

December 2023

SYNERGISTIC STRATEGIES IN SINTER-BASED MATERIAL EXTRUSION (MEX) 3D PRINTING OF COPPER: PROCESS DEVELOPMENT, PRODUCT DESIGN, PREDICTIVE MAPS AND MODELS

By
Kameswara Pavan Kumar Ajjarapu

A Dissertation Approved on

November 30th, 2023

By the following Dissertation Committee

Dr. Kunal H. Kate
Dissertation Chair

Dr. Sundar V. Atre
Committee member

Dr. Bikram Bhatia
Committee member

Dr. Gautam Gupta
Committee member

ACKNOWLEDGEMENTS

First and foremost, I would like to express my utmost gratitude to my Ph.D. advisor, Dr. Kunal H. Kate, for providing me with an opportunity to learn and grow as an individual and as a researcher. I sincerely appreciate his patience, and his dedication to helping students achieve their goals. His neoteric style of advising resonates with me and keeps me inspired to think outside the box while solving real world problems. I will always be thankful to him for believing in me and supporting me through all my endeavors.

I would also like to acknowledge Dr. Sundar Atre, for his guidance and support with my academic and career goals. His ever-joyful demeanor and his ability to maintain an optimistic attitude through difficult time is something I will take with me going forward. Dr. Bikram Bhatia and Dr. Gautam Gupta have been instrumental in shaping my dissertation and channeling the work that I was doing into meaningful, application-oriented studies. I hold high regards for the dedication and work ethic of Dr. Bhatia. His zeal for quality research and effective time-management is something I aspire to inculcate in me. Dr. Gautam Gupta's exhilarating personality on the other hand, brought life to work. Additionally, I cherish the time and collaborative projects I worked on, with Dr. Cindy Harnett, Dr. Tommy Roussel, Dr. Jagannadh Satyavolu, Dr. Jacek Jasinksi, and Douglas Jackson. Further, I consider myself fortunate to have developed a close relationship with the UofL Office of Research and Innovation. A special thanks to Will Metcalf, Laurie Young, and Scott Broughton, for providing me with ample opportunities to present my

ABSTRACT

SYNERGISTIC STRATEGIES IN SINTER-BASED MATERIAL EXTRUSION (MEX) 3D PRINTING OF COPPER: PROCESS DEVELOPMENT, PRODUCT DESIGN, PREDICTIVE MAPS AND MODELS

Kameswara Pavan Kumar Ajjarapu

November 30th, 2023

3D printing pure copper with high electrical conductivity and exceptional density has long been challenging. While laser-based additive manufacturing technologies suffered due to copper's highly reflective nature towards laser beams, parts printed via binder-assisted technologies failed to reach over 90% IACS (International Annealed Copper Standard), electrical conductivity. Although promising techniques such as binder jetting, filament, and pellet-based 3D printing that can print copper exist, they however still face difficulties in achieving both high sintered densities and electrical conductivity values. This is due to a lack of comprehensive understanding of property evolution from green to sintered states and the strategies that can be used to enhance the density and electrical properties of Sinter-Based Material Extrusion (MEX) 3D printed copper parts. This dissertation presents an in-depth investigation into the advancements and challenges of 3D printing pure copper, specifically focusing on Material Extrusion (MEX) processes.

It emphasizes the viability of bound powder copper feedstocks for Material Extrusion 3D printing. It highlights the importance of achieving 100% density in the green stage to ensure over 93% sintered density and 98% Hot Isostatic Pressing (HIP) density. The study delves into the difficulties of 3D printing, sintering, and Hot Isostatic Pressing (HIP) of copper parts, addressing the gap in understanding the scaling of mechanical and electrical properties from the green to the sintered state in the MEX metal 3D printing process. The insights and knowledge gained from this section are then utilized to improve the thermal performance of bound metal MEX 3D printed copper heat sinks. This research explores the uncharted territory of lattice structures for heat sinks, investigating three types of lattice structures through experimental analysis and simulations to explore the potential advantages of lattice structure-based bound metal MEX 3D printing for fabricating high-performance copper heat sinks. Finally, the research focuses on understanding the intricate interplay of material viscosity, mechanical properties, and printing speed in bound-powder-polymer MEX 3D printing. Exploring PLA, TPU, and bronze-filled metal powder-bound filaments, the study investigates their impact on achieving a printed part density of $100\pm5\%$. Process maps of density and viscosity were created for each material type, and a full factorial design of experiments was conducted to identify the effects of print conditions on various variables. This section provides crucial insights into the 3D printing process of polymer filaments, offering guidance for new material design and discovery for bound metal filaments. Overall, this dissertation contributes to understanding the challenges and advancements in 3D printing, providing insights into the scaling of mechanical properties, the thermal performance of copper heat sinks, and the complexities of achieving full part density in 3D printed components.

TABLE OF CONTENTS

LIST OF FIGURES

LIST OF TABLES

CHAPTER 1: BACKGROUND & INTRODUCTION

Copper, celebrated for its versatility, has gained increased attention in 3D printing due to its remarkable blend of outstanding electrical and thermal conductivity, high strength, and corrosion resistance. This material holds the potential to revolutionize applications across diverse industries, particularly in three key areas. First, electronic components can benefit significantly from copper's superior electrical conductivity and efficient heat dissipation. Second, advancements in thermal management systems, including heat exchangers and heat sinks, are possible through the utilization of copper. Lastly, the aerospace and aviation industry can substantially enhance spacecraft propulsion and thermal management systems by integrating copper components.

However, 3D printing pure copper with exceptional density and high electrical conductivity has been a persistent challenge, particularly when employing laser-based technologies like Laser Powder Bed Fusion (LPBF). Copper's inherent reflective nature towards laser beams hinders uniform melting during LPBF, leading to difficulties in achieving accurate prints. Moreover, copper's rapid heat dissipation during printing contributes to warping and distortion of the final parts. In response, binder-assisted technologies have emerged as the preferred choice for 3D printing copper. Despite achieving impressive, sintered densities exceeding 99% after Hot Isostatic Pressing (HIP), surpassing the 90% IACS (International Annealed Copper Standard) electrical conductivity threshold with binder jetting remains elusive.

Various techniques, such as binder jetting and pellet-based 3D printing, have shown promise but present challenges in achieving both high sintered densities and electrical conductivity values. Metal Injection Molding (MIM) of copper, serving as the basis for pellet-based and bound metal material extrusion (MEX) processes, has demonstrated comparable results but has yet to fully realize >90% IACS values. In the filament-based bound metal MEX 3D printing realm, although commercial copper filaments have achieved 95% density, the electrical conductivity has hovered between 82% and 86%, posing a gap in reaching beyond the 90% IACS threshold. The finer Powder Size Distribution (PSD) used in most MEX processes impacts the final properties of the printed copper parts, making it challenging to attain 100% IACS. Additionally, there is a need to focus on the density transition from the green (un-sintered) to the sintered state, a critical factor influencing the final properties of copper parts.

Chapter II, titled "Advancements in 3D Printing and Hot Isostatic Pressing of Copper: Bridging the Gap between Green and Sintered States for Enhanced Mechanical and Electrical Properties," explores the progress and challenges in 3D printing, sintering, and hot isostatic pressing (HIP) of copper parts. This chapter highlights the viability of using bound powder copper feedstocks in Material Extrusion (MEX) 3D printing, achieving properties comparable to conventional metal injection molding. The incorporation of pre-sintering holds in a reducing atmosphere alongside HIP results in remarkable mechanical and electrical properties, offering a pathway for crafting high-performance copper components across electronics, aerospace, and automotive sectors.

As the groundwork is laid for high-performance copper components through 3D printing, the application of lattice structures in creating heat sinks using bound metal MEX

3D printing emerges as a promising avenue. While topology optimization, generative design, and lattice structures have found extensive use in various additive manufacturing methods, their application in bound metal extrusion (MEX) 3D printing remains underexplored. Chapter III, titled "Copper Heat Sinks: Design and Fabrication via Sinter Based Material Extrusion (MEX) 3D Printing," investigates the advantages of lattice structure-based bound metal MEX 3D printing for crafting high-performance copper heat sinks. This chapter explores three types of lattice structures—planar, strut, and surface lattices—focusing on how their design impacts heat transfer efficiency.

This chapter discusses the potential of lattice structures in the context of bound metal MEX 3D printing, offering insights into their design and fabrication for high-performance copper heat sinks. The research utilizes finite element analysis (FEA) simulations and heat transfer experiments, providing a comprehensive exploration of lattice-based heat sinks' thermal performance while maintaining consistency in parameters such as unit cell size, periodicity, and lattice thickness to prioritize the resolution of lattice parts, and surpass the capabilities of the bound metal MEX 3D printer. The aim of this study is to accurately assess the heat transfer efficiency of lattice structures, opening new possibilities for their application as heat sinks.

In tandem, Chapter IV, titled "Mapping 3D Printed Part Density and Filament Flow Characteristics in the Material Extrusion (MEX) Process for Filled and Unfilled Polymers," delves into the complex interplay of material viscosity, mechanical properties, and printing speed in bound powder-polymer MEX 3D printing. The study acknowledges the critical need for achieving nearly 100% part density, a challenge due to the low mechanical and unfavorable rheological properties of highly loaded powder-polymer filaments. The

research creates process maps of density and viscosity, comparing bound metal filaments with unfilled PLA and TPU systems. The investigation employs regression analysis to understand the relationships between material viscosity, mechanical properties, and printing speed, shedding light on the intricate dynamics of the 3D printing process. By addressing this knowledge gap, the study paves the way for optimized, high-density 3D printed components, unlocking new possibilities in material design and discovery for bound metal filaments.

In conclusion, this thesis presents a comprehensive exploration of challenges and advancements in 3D printing of pure copper, its applications in heat sink design, and the intricate relationships governing the 3D printing process for highly filled filament extrusion. Through detailed investigations, the research contributes to the understanding of material-process interactions, the potential of lattice structures in bound metal MEX 3D printing, and the complexities of achieving full part density in 3D printed components. These insights provide a foundation for further advancements in the field, offering new perspectives on material design, process optimization, and the practical applications of high-performance copper components across industries.

CHAPTER 2: ADVANCEMENTS IN 3D PRINTING AND HOT ISOSTATIC PRESSING OF COPPER: BRIDGING THE GAP BETWEEN GREEN AND SINTERED STATES FOR ENHANCED MECHANICAL AND ELECTRICAL PROPERTIES

2.1 Introduction

Copper, renowned for its versatility and widespread use, has garnered increasing attention in the realm of 3D printing, thanks to its remarkable combination of outstanding electrical and thermal conductivity, high strength, and resistance to corrosion. This valuable material holds the potential to revolutionize a multitude of innovative applications across diverse industries. Notably, there are three key areas where 3D-printed copper could prove truly groundbreaking. Firstly, electronic components stand to benefit greatly from copper's superior electrical conductivity and efficient heat dissipation capabilities [1]. Secondly, thermal management systems, including heat exchangers and heat sinks, could witness significant advancements through the utilization of copper [2]. Lastly, the aerospace and aviation industry could substantially enhance spacecraft propulsion and thermal management systems with the integration of copper components [3].

However, achieving 3D printing of pure copper poses challenges due to its high thermal conductivity and melting point, particularly with laser-based technologies like Laser Powder Bed Fusion (LPBF) [4,5]. Copper's reflective nature towards laser beams hampers uniform melting and energy absorption during LPBF, leading to difficulties in

5

producing accurate prints. Moreover, the rapid heat dissipation characteristic of copper during printing can result in warping and distortion of the final part. To optimize sintered density and electrical properties, a reducing atmosphere (hydrogen gas) is required during copper powder sintering. Unfortunately, this is not viable in laser-assisted technology due to safety concerns. As a result, binder-assisted technologies, detailed in *Table 2.1*, have emerged as the preferred choice for 3D printing copper. Among binder-assisted technologies, binder jetting of copper has become the leading industrial technology for metal additive manufacturing due to its high production rate. However, achieving parts with >90% IACS (International Annealed Copper Standard) values has remained a challenge. While reported results indicate impressive sintered density reaching 99% after HIP (Hot Isostatic Pressing), the corresponding electrical conductivity (IACS) value was not provided. Nonetheless, achieving electrical conductivity values exceeding 90% IACS with binder jetting of copper parts remains a hurdle. Direct ink writing (DIW) for copper has also shown mixed outcomes, with one study achieving a high sintered density of 91% but only resulting in 15% IACS [6]. In contrast, the highest reported %IACS for DIW was 52%, but with a sintered density of 89% [7]. This indicates the challenge of achieving over 90% IACS while maintaining high sintered density with DIW. Conversely, pellet-based 3D printing of copper has shown some promise, delivering sintered densities ranging from 91% to 95%. However, %IACS values for this method were not reported. Metal injection molding (MIM) of copper, which serves as the basis for pellet-based and bound metal material extrusion (MEX) processes, has demonstrated comparable results with 90-92% sintered densities [8].

In the filament-based bound metal MEX 3D printing space, commercial copper filaments from Markforged have achieved sintered parts with 95% density and 82 to 86% IACS. Nevertheless, no reports of bound metal MEX 3D printing exceeding 90% IACS have been published. Notably, particle size of powders used in commercial Markforged copper filaments remains undisclosed. In most MEX processes, the use of very fine Powder Size Distribution (PSD) impacts the final properties of the printed copper parts. Achieving 100% IACS in the printed parts has proven challenging due to this fine PSD. Additionally, there is a need for greater focus on the density transition from the green (un-sintered) to the sintered state, which significantly influences the final properties of the copper parts.

Table 2.1: *Copper parts fabricated via different extrusion-based AM technologies in the past*

Technology	Powder PSD	Green Density	Sintered Density	%IACS	Year	Reference
Binder Jet	75μ	N/A	63%	N/A	2015	[9]
	16μ	N/A	78%	N/A	2015	
	15μ	N/A	86%	N/A	2015	
	Bimodal (30μ & 5μ)	N/A	94% (as-sintered) 99% (HIP)	N/A	2017	[10]
	25μ	N/A	78% (as-sintered) 82% (HIP)	52% 64%	2019	[11]
	17μ	N/A	84% (as-sintered)	66% 64%	2019	

			86% (HIP)			
	Bimodal	N/A	91% (as-sintered) 97% (HIP)	81% 90%	2019	
Pellet Based	2μ - 20μ	N/A	91%	N/A	2021	[12]
	6μ	N/A	95%	N/A	2021	[13]
DIW	25μ	N/A	N/A	N/A	2015	[14]
	75 μ	N/A	91%	15%	2017	[6]
	0.5 μ	N/A	90%	N/A	2017	[15]
	10 μ - 25 μ	N/A	89%	52%	2020	[7]
Filament Based	16μ	N/A	N/A	N/A	2021	[16]
	Markforged MetalX	N/A	95%	86%	2021	[17]
	4μ - 28μ	Filament porosity studied	N/A	N/A	2021	[18]
	Markforged Filament	N/A	95%	82%	2022	[19]
	D$_{90}$< 36μ	**99% (w.r.t feedstock)**	**93% (as-sintered) 98% (HIP)**	**86% 100%**	**2023**	**This work**

This paper explores the challenges of 3D printing, sintering, and HIPing copper parts. Our study demonstrates that bound powder copper feedstocks can be transformed into filaments and used for Material Extrusion 3D printing. The MEX process combines

Fused Filament Fabrication (FFF) and powder injection molding to create three-dimensional parts. Achieving 100% density during the green stage is crucial to attain over 90% sintered density and over 95% HIP density, ensuring comparable mechanical properties to traditional metal injection molding. Proper debinding, sintering, and HIP are essential for obtaining desired properties. This research addresses the lack of understanding in scaling mechanical properties from green to sintered state for MEX metal processes with bound powder-polymer metal filaments. The study tests copper feedstock and filaments on a conventional FFF machine, advancing additive manufacturing capabilities with non-ferrous materials like copper using the MEX process.

2.2 Materials & Methods

The present work used copper metal powders of spherical morphology, with particle size (D_{90}) of <36μm (Kymera International, Velden, Germany). As-received copper powders were of high purity (>99.9% copper), with very low concentration of trace elements such as Fe, and P (<20ppm). As-received powders were characterized for true (ρ), apparent (ρ_a), and tap (ρ_t) densities to assess their flowability and packing density. The true density was measured using a helium gas pycnometer, while the tap density was measured using a tap density volumeter in accordance with ASTM B527-15. The apparent density was calculated by measuring the apparent volume of the powders using a graduated cylinder and dividing that by its mass to obtain the apparent density. The copper powder and the multi-component binder system were compounded in a torque rheometer and then ground into smaller pellets. The 61vol.% copper feedstocks were extruded into filaments with a consistent diameter of 1.75±0.05 mm using a capillary die with an L/D ratio of 30mm:1.75 mm on a capillary rheometer. The extrusion temperature was chosen to be

105°C with a uniform extrusion speed of 0.1 mm/s to obtain a filament of smooth surface finish and consistent diameter. The feedstock homogeneity was verified by measuring time-dependent variations in viscosity at a constant shear rate and temperature [20]. A constant shear rate of $50s^{-1}$ at 160°C was used to evaluate the variations in feedstock viscosity to measure its homogeneity. Tablets with nominal dimensions of $10 \times 10 \times 5$ mm have been successfully designed and 3D printed using MatterControl 2.0 software, making them suitable for density measurements in green and sintered states. Tensile bars (ASTM E8 standard) and long rectangular bars ($100 \times 5 \times 4$mm) for electrical conductivity measurements were 3D printed using Pulse 3D Printer, MaterHackers, Lakeforest, CA, USA. A Taguchi L9 matrix was used in selecting print parameters, a bed temperature of 65°C, a print speed of 5 mm.s^{-1}, a nozzle temperature of 220°C, a layer thickness of 0.1mm, and an extrusion multiplier of 120% to ensure consistent material flow and promote strong inter-bead and inter-layer bonding. These parameters resulted in green parts with >99% density relative to the feedstock.

To reduce thermal debinding time and debinding-related defects while completely removing the binder components, a two-step debinding procedure involving solvent dissolution and thermal dissociation of the binder system was used. The 3D printed green parts were first solvent debound in n-heptane solution at 64°C for eight hours in a hot solvent bath. The solvent-rebound samples were then dried overnight in an oven at 50°C to remove the residual solvent. The thermal debinding profile was developed using thermal degradation data of the feedstock, which was generated using a thermogravimetric analyzer (TGA, SDT Q600, TA Instruments, New Castle, DE, USA). The samples' thermal debinding was carried out in a stable hydrogen atmosphere using a heating rate of 1°C/min.

Secondary debinding steps were performed at 500°C and 600°C for 1 hour each, and 700°C, 800°C and 900°C for 2 hours each to enable complete binder removal while also promoting sintering in a reducing environment [21,22]. The debinding cycle was followed by sintering at a temperature of 1075°C for 3 hours in a hydrogen atmosphere. Further, as-sintered parts were subjected to HIPing. HIP process was carried out at a pressure of 100 MPa and a temperature of 950 °C. The as-sintered were held under these conditions for 120 minutes using a Quintus QIH15L HIP furnace in a high-purity (99.995%) inert atmosphere of argon gas, ensuring the attainment of maximum sintered density and desired electrical conductivity properties for the heat sinks.

At least three samples were tested for each characterization technique (Archimedes density, tensile testing, and electrical conductivity). Both as-sintered and HIPed samples were subjected to grinding and polishing for a mirror finish. The surfaces were ground using SiC paper with grit sizes varying from 240 to 1200 and polished with 9 µm and 1 µm diamond suspensions. The polished density cubes were then etched using the standard $FeCl_3$, ethyl alcohol, and hydrochloric acid solution [23]. Archimedes density measurement was performed on the as-sintered and HIPed samples to calculate the densities relative to the pycnometer density of the initial powder particles. The tensile properties of the as-sintered and HIPed samples were measured at a strain rate of 1.0 mm.min^{-1} with an MTS 810 hydraulic dual-column tensile testing system. Electrical conductivity of samples was determined using a four-probe method, where a current I is applied across the sample of known cross-section, while measuring the voltage V across the other two probes separated by a known distance (50mm). Finally, cross sections of

these etched samples were observed to study the microstructure and pore distribution, using a Thermo Fisher Apreo C Field Emission Scanning Electron Microscope (SEM).

2.3 Results and Discussions

2.3.1   Powder, Feedstock & Filament Characteristics

The copper powders that were received were analyzed through SEM and the results are shown in *Figure 2.1(a)*. It was observed that the powders had a clear spherical morphology, indicating that gas atomization was used during processing. The manufacturer's particle size distribution revealed that 90% of the particles were less than 36μm. *Table 2.2* summarizes the packing attributes of the copper powders, including the pycnometer density, tap density, and apparent density. The powder packing fraction was calculated to be 63.13%, which is an estimate of the critical solids loading that could lead to powder-binder separation. The Hausner ratio was also calculated from the ratio of powder tap density (ρ_t) to the powder pycnometer density (ρ) [24] to determine the powder flowability, which was found to be acceptable at 1.21. Higher flowability can reduce feedstock viscosity, making 3D printing easier even at high solids loadings. This result is consistent with the observation that a higher value of powder flowability (lower Hausner ratio) is generally expected to decrease the feedstock viscosity by providing a lower resistance to flow within the polymer binder matrix, thus making 3D printing easier at high solids loadings [25].

Table 2.2: Density measurements of as-received copper powder particles

	Pycnometer density ρ (g/cc)	Apparent density ρ_a (g/cc)	Tap density ρ_t (g/cc)
Copper powder	8.92 ± 0.00	5.03 ± 0.01	5.63 ± 0.04
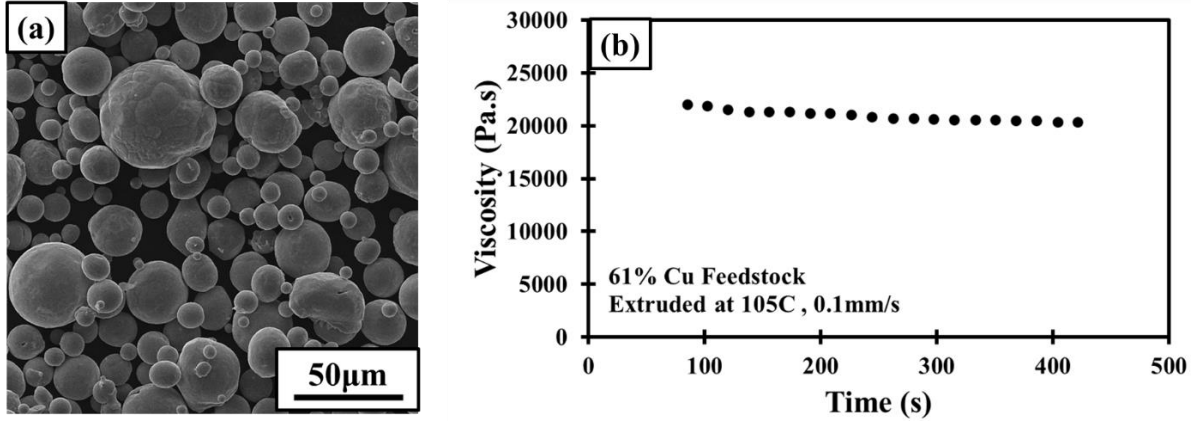
Figure 2.1: *(a) SEM image of copper powder particles (b) Time-dependent viscosity measurements for copper feedstocks*

Viscosity and pressure drop in heated nozzles are dependent on various factors for the filament to 3D print without any challenges. These factors include powder loading, binder composition, feed rate, temperature, and heat transfer gradients (temperature drops) in the heated liquefier and nozzle sections and are highly dependent on the viscosity variation. Therefore, we performed a thorough analysis of the feedstock homogeneity where it was observed that the feedstock viscosity remained at an average of 21000 Pa.s for 61 vol.% feedstock. This was measured for thirteen data points at a constant shear rate of $34s^{-1}$ (0.1mm/s) and a temperature of 105°C, as shown in *Figure 2.1(b)*. It is important to note that the viscosity and pressure drop in the heated nozzle depend on several factors, including powder loading, binder composition, feed rate, temperature, and heat transfer gradients. Our team also analyzed the extruded metal powder-filled filaments for defects and inconsistencies using SEM imaging along the cross-section and outer surface (*Figure 2.2*). We found that the powder was homogeneously dispersed in the polymer matrix with no noticeable voids. The cross-section of the filament was also circular ($\emptyset$ 1.75 $\pm$ 0.05 mm), and none of the filament batches showed any deformation in shape or ovality.

13
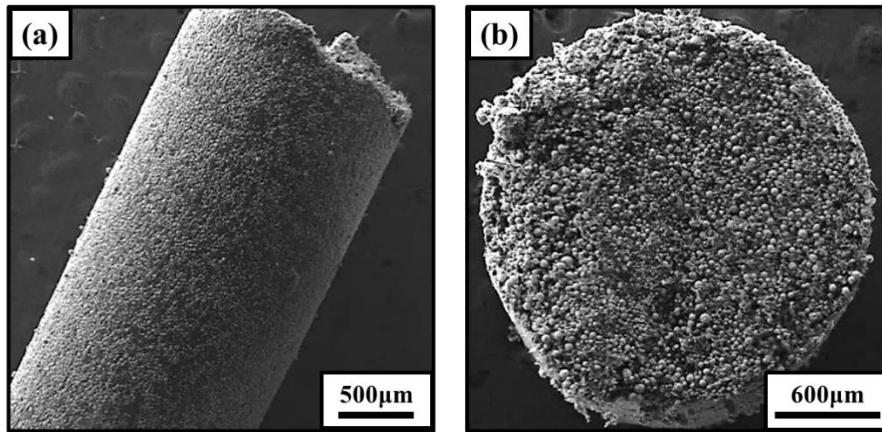
Figure 2.2: (a) Surface of extruded copper filled polymeric filament (b) Cross-section of copper filament

2.3.2 Dimensions, Shrinkage and Density

The 3D printed parts were analyzed for their dimensions and compared to the actual CAD part dimensions. **Figure 2.3(a)** shows a side-by-side comparison of a 3D printed density cube in its green and sintered states respectively. Similar density cubes, as well as tensile dogbones and bars for electrical conductivity measurements (**Figure 2.3(b)**) were 3D printed, sintered and HIPed. It was discovered that the parts' geometric tolerances depend on several factors. These factors include the motion controlled by the gantry system, the selection of process parameters, and the printed material properties. The stepper motor's step size controls the accuracy and details to which a CAD model is translated into a built part in the gantry system. *Table 2.3* shows that the printed parts were larger than their respective designs in all directions. The percentage deviation from the CAD part along the side was seen to be higher. The die swelling phenomenon occurs as the melt leaves the printer nozzle, causing the material to flow laterally. Furthermore, the layer thickness (100µm) is much less than the diameter of the nozzle (600µm), which causes the material to be squeezed through the print nozzle over the print bed or previous layer, resulting in

broader deposited beads. It is worth noting that the part dimensions in X/Y directions also depend on other process parameters, such as the extrusion multiplier and printing speed. The experiment results showed that the sintered parts exhibited a linear shrinkage of 14.6%, while the parts that underwent additional HIPing post-processing resulted in a slightly higher linear shrinkage of 15.6%. This shrinkage indicates a reduction in size during debinding, sintering, and HIP stages of the manufacturing process. As- sintered parts sintered to 93% relative density, while HIPing these samples helped achieve up to 98% in density, relative to the pure powder.
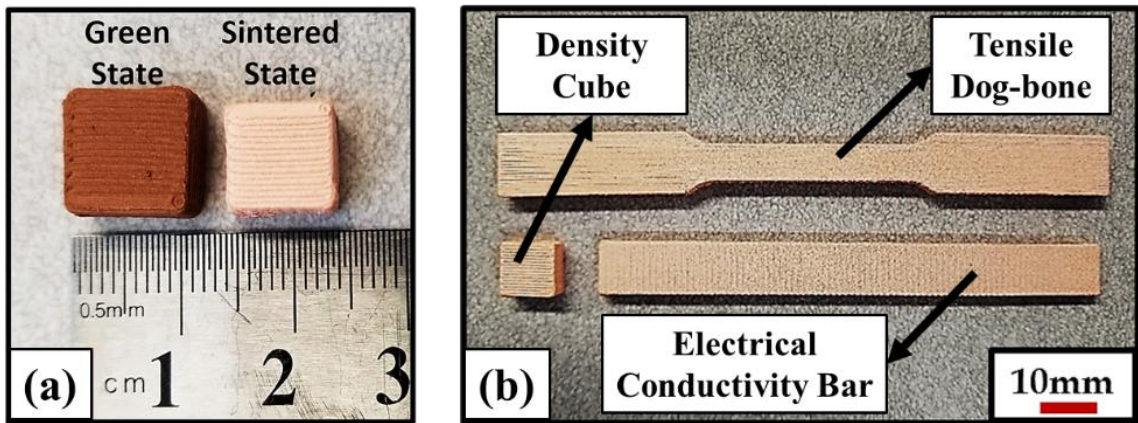
Figure 2.3 : (a) MEX 3D printed density cube in green and sintered states (b) Different geometries: density cube, tensile dog-bone, and electrical conductivity bar, printed and sintered via MEX 3D printing

Table 2.3: Variation in printed part dimensions of density cube tablets

Direction	CAD Part Dimension	Printed Part Dimension	% Deviation from CAD part	As-sintered Dimension	HIPed Dimension
Side	10mm	10.70 ± 0.01mm	6.60 ± 0.10	9.10 ± 0.00mm	9.00 ± 0.00mm
Height	5mm	5.10 ± 0.01mm	1.70 ± 0.10	4.10 ± 0.06mm	4.10 ± 0.06mm

2.3.3   Mechanical and Electrical Properties

Additionally, the parts' ultimate tensile strength (UTS) increased from 170 MPa to 188 MPa after the HIP process, demonstrating enhanced mechanical strength and durability. Additionally, the elongation at failure increased from 23% to 32%, indicating higher ductility in post-HIPing. The stress vs. strain behavior of the sintered copper parts and the HIP copper parts showed notable differences, as shown in Figure 2.4. The elastic regime in both as-sintered and HIPed parts was barely noticeable, with the samples deforming plastically at a very low strain. Inset in **Figure 2.4(a)** depicts the linear elastic region of the stress-strain curve at lower % strain. HIP process significantly improved the stress vs. strain response of the copper parts. The HIP copper parts displayed higher strength of 188MPa and failed at 32% strain compared to the sintered parts which sustained a maximum stress of 170MPa and failed at 23% strain. The Young's modulus from stress vs. strain curve in the HIP parts indicated higher stiffness (75GPa) compared to as-sintered parts (37GPa) as seen in **Figure 2.3(b)**. The HIP process subjects the copper parts to high pressure and temperature, resulting in enhanced interparticle bonding and increased density. This densification process leads to improved mechanical properties and higher resistance to deformation. As a result, the stress-strain curve for HIP copper parts exhibits higher strength and stiffness, indicating a greater ability to withstand applied loads. It is also worth noting that the variation in UTS and % Elongation is higher in HIPed samples than in as-sintered conditions. HIPed samples showed a 3% deviation in UTS while as-sintered samples displayed only 1% deviation. Similarly, the % elongation in HIPed samples showed much higher deviation than that in as-sintered conditions. However, the standard deviation in Young's modulus for both HIPed and as-sintered samples were seen

to be very low (<1%) in spite of HIP treatment improving the Young's modulus of as-sintered samples by up to 70%. Such variation in mechanical data of samples processed under similar conditions was observed in past literature and is hypothesized to be due to the differences in grain size, grain structure, and porosity evolution from as-sintered to HIPed conditions.
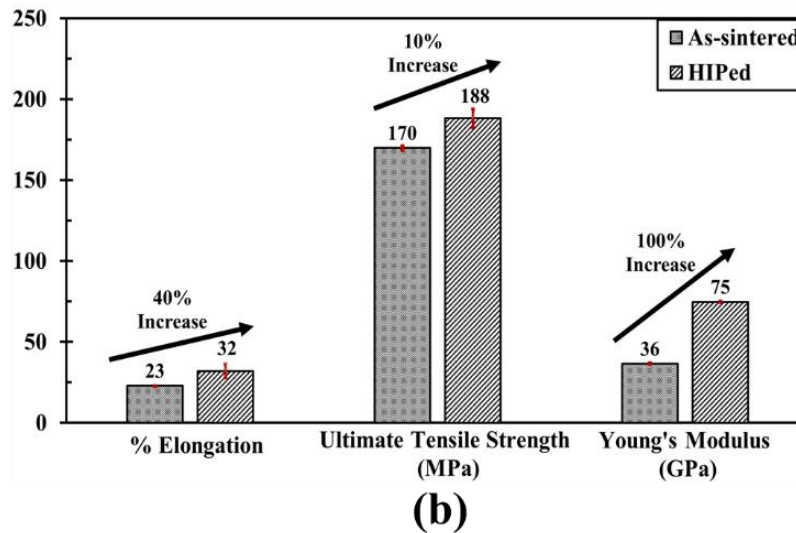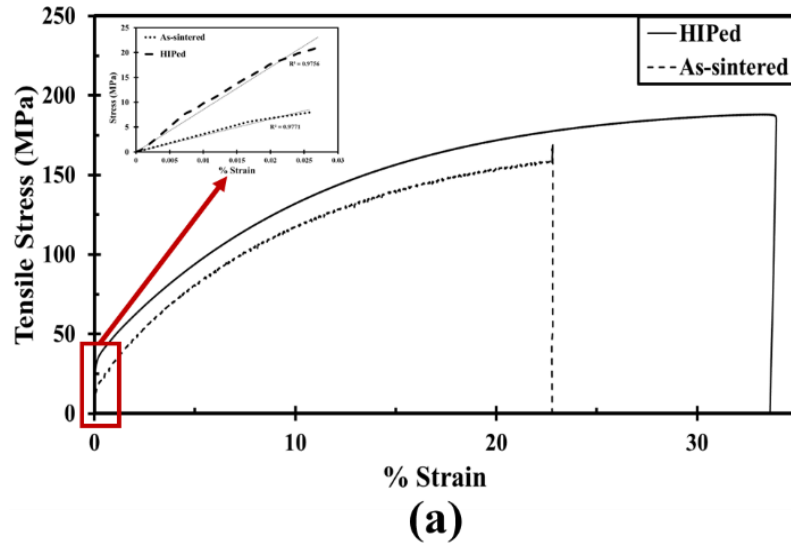
Figure 2.4 : (a) Stress vs strain for as-sintered and HIPed parts (inset showing the linear elastic region at lower % strain), (b) %Elongation, ultimate tensile strength, and Young's modulus of as-sintered and HIPed parts

17

The electrical properties of copper parts undergo significant improvement when they are subjected to the HIP process from their sintered states. Sintered copper parts typically exhibit lower electrical conductivity due to factors such as porosity and incomplete interparticle bonding. However, the HIP process plays a crucial role in enhancing the electrical properties of copper parts. This process effectively eliminates any existing voids or closer porosity within the sintered structure, leading to a denser and more conductive material. The improved connectivity between copper particles allows for more efficient electron flow and reduces resistivity. As a result of the densification achieved through HIP, the electrical conductivity of the copper parts undergoes a significant increase compared to their sintered state, as seen in **Table 2.4.** An increase in sintered density from 93% to 98% showed a clear increase in electrical conductivity values from 86% IACS (International Annealed Copper Standard) to 100% IACS. Therefore, the electrical conductivity values of copper samples 3D printed, sintered, and HIPed are much higher than that observed in copper parts 3D printed using other additive manufacturing techniques such as binder jetting, direct ink writing, or pellet-based extrusion 3D printing (**Table 2.1**).

Table 2.4 : *Electrical conductivity (%IACS) and relative density (w.r.t. pure powder) of samples in as-sintered and HIPed conditions*

	As-sintered samples	**HIPed samples**
% Relative Density (w.r.t pure powder)	92.4 ± 0.6 %	97.7 ± 0.8 %
Electrical Conductivity (% IACS)	85.8 ± 0.3 % IACS	99.7 ± 0.4 % IACS

This enhancement in electrical conductivity is crucial for applications where effective heat transfer is essential, as it enables efficient dissipation of heat through the copper parts. In summary, the HIP process plays a vital role in improving the electrical properties of copper parts by increasing density, improving interparticle bonding, and enhancing electrical conductivity. This enhancement enables the copper parts to efficiently conduct electricity, making them highly suitable for applications requiring effective heat transfer and reliable electrical performance.

2.3.4   Microstructure

The microstructure of copper parts undergoes significant improvements when subjected to the HIP process. One prominent change is the reduction in porosity within the microstructure. Sintered 3D-printed copper parts often exhibit inherent porosity resulting from powder consolidation and sintering. However, through HIP, the application of high pressure and temperature helps to close and eliminate these pores, resulting in a microstructure with reduced porosity (**Figure 2.5**). The closure of pores in the copper microstructure leads to a more uniform and consistent 3D-printed part. This improved microstructure is crucial for enhancing the mechanical properties of the HIP parts. With fewer pores and a more compact structure, the HIP parts exhibit increased strength, overall mechanical and electrical performance compared to their sintered counterparts (**Figure 2.4** and **Table 2.4**). The closure of pores from **Figure 2.5(a)** and **Figure 2.5(b)** to **Figure 2.5(c)** and **Figure 2.5(d)** also contributes to improved dimensional stability and reduced variation in mechanical properties, which is a critical need for 3D-printed parts.

In both as-sintered and HIPed samples, twinning behavior, characteristic of copper, is observed (**Figure 2.5**). After HIPing (**Figure 2.5(c)** and **Figure 2.5(d)**), grain coarsening

is evident, with visibly larger grains observed in the microstructure. Although grain coarsening can lead to reduced strength, the pore closure and increase in sintered density have improved the ultimate tensile strength of HIPed copper samples. Additionally, grain coarsening decreases the grain boundary volume fraction, improving ductility and electrical properties (**Figure 2.4, Table 2.4,** and **Figure 2.5**).
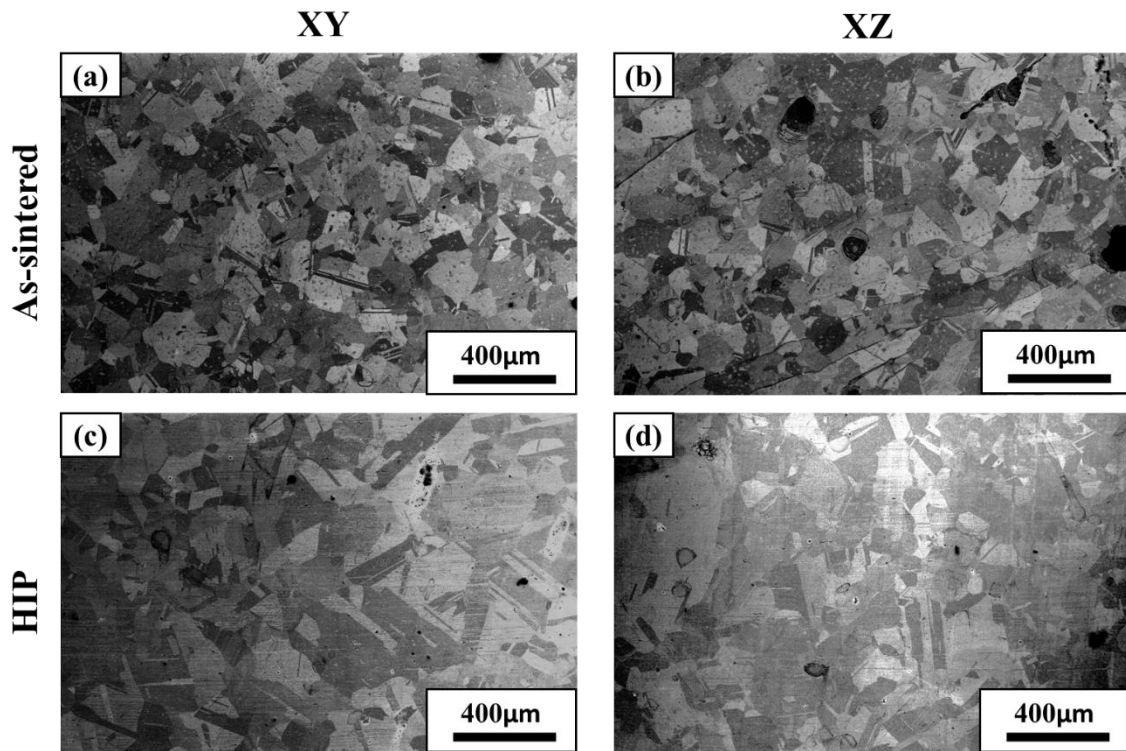
Figure 2.5 : Polished and etched microstructures of (a,b) As-sintered copper in XY and XZ cross-sections (c,d) HIPed copper in XY and XZ cross-sections

The increase in % elongation, Young's modulus, and % IACS after HIPing can be attributed to pore-closure and densification, while it was hypothesized that the increase in grain size also assists in improving the ductility of HIPed samples (**Figure 2.4** and **Table 2.4**). Finally, grain coarsening and improved sintered density can also explain the increased toughness (energy absorbed until fracture) in HIPed samples compared to as-sintered samples. The overall microstructural improvements achieved through the HIP process

contribute to the enhanced mechanical and electrical properties of 3D-printed copper parts, making them more reliable and suitable for demanding applications in various industries.

2.4 Conclusions

This paper has comprehensively explored the challenges and advancements in 3D printing, sintering, and HIPing of copper parts. This study demonstrated the compounding of bound powder copper feedstocks with a volumetric loading of 61%. It successfully showcased the feasibility of processing these feedstocks through Material Extrusion (MEX) 3D printing, followed by debinding, sintering, and HIP treatments. The achievement of mechanical properties comparable to those of the traditional Metal Injection Molding (MIM) process underscores the significance of this research in bridging the gap between the green and sintered states in metal MEX 3D printing.

A pivotal aspect of this study lies in the strategic utilization of pre-sintering holds at varying temperatures in a hydrogen reduction atmosphere coupled with the HIP process. This approach has proven instrumental in enhancing the copper parts' mechanical and electrical properties. The synergy of pre-sintering holds, and HIP treatment facilitates the reduction of surface oxide layers during sintering, while pore-closure and grain coarsening during HIP contributes to improved properties.

As a result, the grain boundary volume fraction is decreased, leading to enhanced ductility and electrical properties. This is evidenced by the notable improvements in mechanical performance, with ultimate tensile strength rising from 170 MPa to 190 MPa, and elongation at failure increasing from 23% to 32%, indicative of heightened ductility. Moreover, Young's modulus experiences a substantial increase from 35GPa to 75GPa, showcasing enhanced stiffness in the post-HIPed components. Additionally, the most

noteworthy finding of this study is the significant improvement in electrical conductivity: the transition from 86% IACS to 100% IACS. This heightened electrical conductivity holds immense promise for applications necessitating effective heat transfer and reliable electrical performance.

The intricate interplay of these processes contributes to the advancement of sintered densities, which escalate from 93% in the sintered state to an impressive 98% post-HIP. This enhanced density, accompanied by grain coarsening, serves to fortify the ultimate tensile strength of HIPed copper samples, compensating for any potential reduction in strength due to grain coarsening. This study stands as a pioneering endeavor, being the first to present superior findings in mechanical and electrical properties through 3D printing. As such, it opens up new horizons for the future evolution of this technology. The fusion of 3D printing and HIPing emerges as a potent methodology, offering the potential to manufacture high-performance copper parts tailored to the exacting demands of diverse industries, encompassing electronics, aerospace, and automotive sectors.

CHAPTER 3: COPPER HEAT SINKS: DESIGN AND FABRICATION VIA SINTER BASED MATERIAL EXTRUSION (MEX) 3D PRINTING

3.1 Introduction

Traditional manufacturing processes such as metal injection molding, casting, and machining have been extensively utilized for producing metal parts, including heat sinks. However, these processes often impose limitations on design flexibility, resulting in heat sinks with similar designs. Specifically for heat sink fabrication, techniques like bonding, folding, skiving, or machining are commonly employed. Nevertheless, these methods have inherent constraints when it comes to design freedom, as they are mainly restricted to fin-like structures. To overcome these limitations and explore advanced manufacturing solutions, researchers have started investigating 3D printing as an alternative method for heat sink fabrication. 3D printing, also known as additive manufacturing, offers greater design freedom, allowing for the creation of complex geometries and internal structures that can optimize thermal performance. However, challenges arise when it comes to 3D printing pure copper due to the material's high thermal conductivity and melting point. Laser-based 3D printing technologies like Laser Powder Bed Fusion (LPBF) face difficulties in achieving successful prints with pure copper [5]. Copper has high reflectivity to the laser used in LPBF, making it difficult to achieve proper energy absorption and melt the powder uniformly [5]. Additionally, the high thermal conductivity of copper can cause

rapid heat dissipation during the printing process, resulting in warping and distortion of the printed part.

Despite these challenges, researchers have made progress in 3D printing copper heat sinks using LPBF. They have been experimenting with various process parameters, such as laser power, scanning speed, and powder characteristics, to optimize the printing conditions and achieve better results with 3D printing copper while employing high laser power source of between 100-200 W. Alternatively, instead of changing process approaches to improve printability of copper, some researchers have explored processing copper alloys by adding small amounts of other metals, such as chromium and zirconium that aids melting behavior and modifies laser absorption characteristics, making it more suitable for achieving high sintered densities with copper while maintaining good thermal conductivity [26]. Some specific examples of 3D printed heat sinks include studies conducted by Singer et al, Mezghani et al., Moon et al., Balzarotti et al. and Sciacca et al.[4,5,27–29]. Singer et al. reported on advances in thermal management using additively manufactured Cu components, which can produce low-mass structures and polymer/metal composites with the potential for transformative impact [27]. Mezghani et al. utilized LPBF to produce integrated wicking structures for heat pipes and vapor chambers with unprecedented design freedom, providing foundational knowledge to fabricate complete assemblies of copper vapor chambers (VCs) and heat pipes (HPs) [5]. Moon et al. designed and manufactured an ultra-power-dense tube-in-tube heat exchanger using shape optimization enabled by a genetic algorithm, achieving significant increases in power density and specific power [28]. Balzarotti et al. investigated 3D-printing replica procedures for producing copper periodic open cellular structures for enhanced substrates

for heat-transfer-limited catalytic processes [29]. Sciacca et al. conducted experimental and numerical characterization of pure copper heat sinks produced by laser powder bed fusion, demonstrating their suitability for liquid cooling,and the potential for enhanced heat transfer [4]

Heat sink design strategies have evolved to encompass topology optimization, generative design, and lattice structure design. These approaches offer distinct advantages in terms of thermal performance and structural performance vs traditional approaches [30–32]. Topology optimization and generative design employ computational algorithms to achieve an optimal distribution of material within the design space, enhancing heat transfer capabilities. On the other hand, lattice structures are lightweight, open-cell configurations composed of repeating unit cells. They provide high surface area for efficient heat dissipation while reducing the weight of the heat sink, an advantage not feasible with traditional manufacturing techniques.

While topology optimization, generative design, and lattice design have been widely employed in various additive manufacturing (AM) methods like laser powder bed fusion (LPBF), stereolithography (SLA), and binder jetting, they have not been extensively explored for metal fused filament fabrication [33–35]. Among the AM technologies capable of producing intricate parts, bound metal material extrusion (MEX) stands out as the most open source process, thanks to lower equipment costs, freedom to design new feedstock materials, and overall lower sintering processing expenses [36,37]. Recent studies have aimed to redefine the design possibilities for heat sinks using 3D printing technology. For instance, Lazarov et al. conducted research on polymer heat sinks utilized in LED lamps [38]. They employed 3D printing to create heat sinks with topology-

optimized designs, lattice structures, and simplified pin-fin interpretations. The resulting heat sink solutions exhibited complex, organic-looking topologies that could be additively manufactured, offering unparalleled design freedom. In contrast, traditional heat sink manufacturing techniques often necessitate post-processing to remove supports and are limited to producing simpler structures.

Furthermore, Yaple's Master's thesis [39] explored additive manufacturing for heat sinks with bio-inspired and cellular structures. The project involved developing a process for manufacturing the copper alloy CuNi2SiCr using a laser powder bed fusion (LPBF) 3D printer. The objective was to obtain parts with a density of 94%, addressing challenges related to copper's low absorptivity and susceptibility to oxidation. Yaple and the team tested traditional pin and fin designs as well as two additional heat sinks: one bio-inspired and another incorporating Triply Periodic Minimal Surface (TPMS) cellular structures. The bio-inspired heat sinks outperformed other designs in terms of heat sink performance.

However, current copper parts produced via additive manufacturing typically have densities ranging from 94% to 97%. LPBF, the primary manufacturing method for these parts, often yields electrical conductivity values of 85% or lower in IACS (International Annealed Copper Standard). Studies have indicated that high electrical conductivity is essential for achieving improved thermal performance in heat sinks, suggesting a correlation between IACS values and heat sink effectiveness. To enhance electrical conductivity, copper powders can be sintered in a reducing atmosphere, reducing oxide layers and leading to higher sintered densities and %IACS electrical conductivity values. Unfortunately, laser-based 3D printing methods do not allow the introduction of reducing atmospheres like H_2, limiting the ability to achieve highly thermally performing copper

26

heat sinks through LPBF. Alternatively, the Bound metal MEX 3D printing method enables the introduction of reduced atmospheres during sintering. However, research on using pre-sintering reduction atmospheres in bound metal MEX 3D printing of copper remains unexplored.

Hence, this study aims to address the existing research gap by examining the use of extended hold times and a reduced atmosphere to achieve enhanced thermal performance in bound metal MEX 3D printed copper heat sinks, by fabricating highly dense copper parts with 100% IACS electrical conductivity. Notably, there is a scarcity of published studies on fabricating heat sinks using pure copper with the bound metal MEX process. Furthermore, the application of lattice structures in creating heat sinks through bound metal MEX 3D printing remains unexplored. Therefore, this study will investigate three types of lattice structures that offer open, closed, and semi-open pathways to facilitate efficient heat transfer. Consequently, this research endeavors to explore the potential advantages of employing lattice structure-based bound metal MEX 3D printing for fabricating copper heat sinks, utilizing a combination of experimental analysis and simulations.

3.2 Materials & Methods

3.2.1   Copper feedstock, filaments and 3D printing process parameters

The present work used copper metal powders of spherical morphology, with particle size (D_{90}) of <36μm (Kymera International, Velden, Germany). Copper powder and the multi-component binder system were compounded in a torque rheometer and were subsequently ground into smaller pellets (Plastic and Rubber Chopper PRC22-N180, Col-Int Tech, South Carolina, USA). Copper feedstocks at 61vol.% were extruded into

filaments with a consistent diameter of 1.75±0.05 mm using a capillary die with an L/D ratio of 30 mm:1.75 mm on a capillary rheometer (Rheograph 20, GÖTTFERT Werkstof-Prüfmaschinen GmbH, Germany). The filament extrusion temperature was chosen to be 105°C with a uniform extrusion speed of 0.1 mm/s to obtain a filament of smooth surface finish and consistent diameter. Tablets (10 X 10 X 5 mm) and bars (100 X 5 X 4 mm) for density and electrical conductivity measurements were designed and 3D printed using MatterControl 2.0 software (Pulse 3D Printer, MaterHackers, Lakeforest, CA, USA). Print parameters were selected based on design of experiments using a Taguchi L9 matrix. A bed temperature of 65°C was seen to facilitate good adhesion of the part to the build platform. A print speed of 10 mm s^{-1}, nozzle temperature of 220°C, layer thickness of 0.2 mm, and an extrusion multiplier of 120% was chosen to ensure consistent material flow and promote strong inter-bead and inter-layer bonding. These print parameters were kept constant while fabricating lattice structure-based heat sinks for this study.

3.2.2   Design Considerations for Lattice Based Heat sink

When designing heat sinks with lattice structures, there are several important considerations to take into account. In this study, three types of lattice structures were utilized: planar lattice, strut lattice and surface lattice (Figure 1). The lattice designs for heat sinks were generated using nTopology software. Each structure offers unique characteristics and influences the heat transfer pathways within the heat sink.

1. Planar Lattice: The planar lattice is a hexagonal plane design that is extruded/repeated in a single direction to form a closed honeycomb pattern (Figure 3.1(**a**))

2. <u>Strut Lattice</u>: The strut lattice design is comprised of a series of rods/struts that are connected to form the unit cell (**Figure 3.1(b)**)

3. <u>Surface Lattice</u>: The surface lattice, on the other hand, is an open lattice design with wavy channels described in all three dimensions by trigonometric equations (**Figure 3.1(c)**)

Our study is centered around the lattice structure itself to test how the lattice design structures effect heat transfer efficiency. We kept certain parameters constant, such as the unit cell size, periodicity, and lattice thickness, to ensure consistency. Our main priorities are to guarantee that the lattice part's resolution surpasses the capabilities of the bound metal MEX 3D printer, eliminate overhangs in the lattice design to support its stability, and ensure that each feature within the lattice part has a similar thickness. By doing so, we can accurately assess the effectiveness of heat transfer of the lattice structures and their performance as heat sinks.

(a)   **(b)**   **(c)**
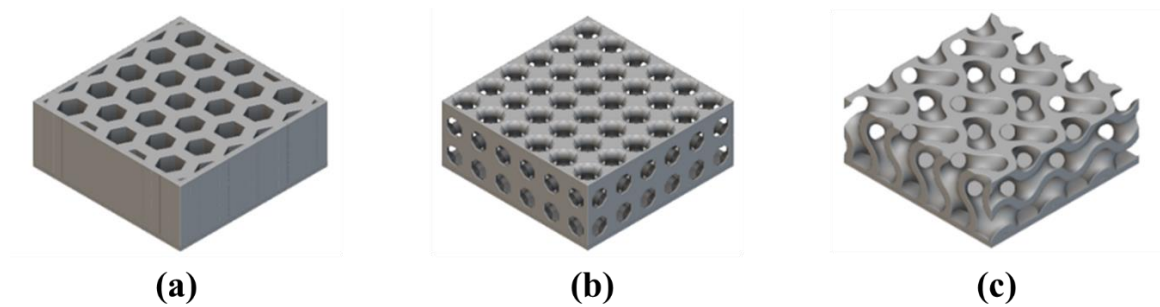
Figure 3.1: *Lattice designs generated via nTopology (a) planar lattice (b) strut lattice (c) surface lattice*

3.2.3   Thermal Simulations for Lattice-Based Heat Sink

Parallel to experimental testing, a steady heat transfer simulation was conducted in ANSYS Fluent using the lattice STL files generated through nTopology (planar, strut, and surface). Boundary conditions were applied in accordance with the experimental setup

utilizing the copper heat sinks: a constant power input (1, 1.5 and 2 W) at the base of the heat sink and surrounding air temperature of 26°C. Temperature contour plot of the surface lattice heat sink geometry with a power input of 2 W is presented in **Figure 3.2** for visualization. The simulation results provided steady-state temperature and heat distribution profiles. These outputs were compared with experimental data to validate the simulations' accuracy and provide insights for designing next-generation heat sinks. The simulations serve as a valuable guide to enhance the heat sink performance based on their ability to capture real-world heat transfer behavior.

3.2.4 Debinding, Sintering and HIP

The fabrication process of the 3D printed heat sinks involved several steps. Firstly, the green parts were subjected to solvent debinding in an n-heptane solution at a temperature of 64 °C for 8 hours. Subsequently, thermal debinding and sintering processes were performed. The thermal debinding profile was developed based on the thermal degradation data obtained from thermogravimetric analysis (TGA) using a SDT Q600 instrument from TA Instruments, with a heating rate of 5 °C/min up to 600 °C under a nitrogen (N2) atmosphere. For the sintering step, all 3D printed heat sinks were sintered in a 100% hydrogen (H_2) atmosphere at a temperature of 1075 °C for a duration of 3 hours. The use of the H_2 atmosphere helps to achieve maximum sintered density and optimal electrical conductivity properties in the final heat sink parts. Furthermore, the heat sinks underwent the HIP (Hot Isostatic Pressing) process. The HIP process was carried out at a pressure of 100 MPa and a temperature of 950 °C. The heat sinks were held under these conditions for 120 minutes using a Quintus QIH15L HIP furnace. The HIP process was performed in a high-purity (99.995%) inert atmosphere of argon gas, ensuring the

attainment of maximum sintered density and desired electrical conductivity properties for the heat sinks.

3.2.5 Electrical Properties and Density Measurements.

The sintered and HIP 3D printed heat sinks were subjected to electrical and density measurements. Electrical conductivity was determined through a four-point probe method using a multimeter and four-point probe station, where a current I is applied across the sample of known cross-section, while measuring the voltage V across the other two probes separated by a known distance (50mm). Additionally, the density of both the sintered and HIP parts was measured using an Archimedes setup, conforming to ASTM standard B962-17. These measurements provide essential data to evaluate the electrical properties and density characteristics of the 3D printed heat sinks.

3.2.6 Testing setup for Heat Sink and LabView programming

A heater block with 28mm X 28mm (x/y) dimensions was acquired and connected to a thermocouple and source meter (**Figure 3.2**). This setup was interfaced with a NI LabVIEW program, incorporating a virtual PID controller to maintain a constant electrical power output from the heater. We tested different heat sinks with constant heater powers of 1, 1.5, and 2 Watts. Temperature measurements were taken until the temperature reached a steady state, both with and without the heat sink attached to the heater block. To prepare the heat sinks for mounting, the base of the 3D-printed heat sink was polished with 325 mesh grit size paper to obtain a smooth surface. Thermal paste was then applied to the heat sink base, and it was mounted on the heater block. To reduce heat loss from the heater block, insulation was applied to the bottom and side surfaces, promoting heat transfer to the mounted 3D-printed heat sink.
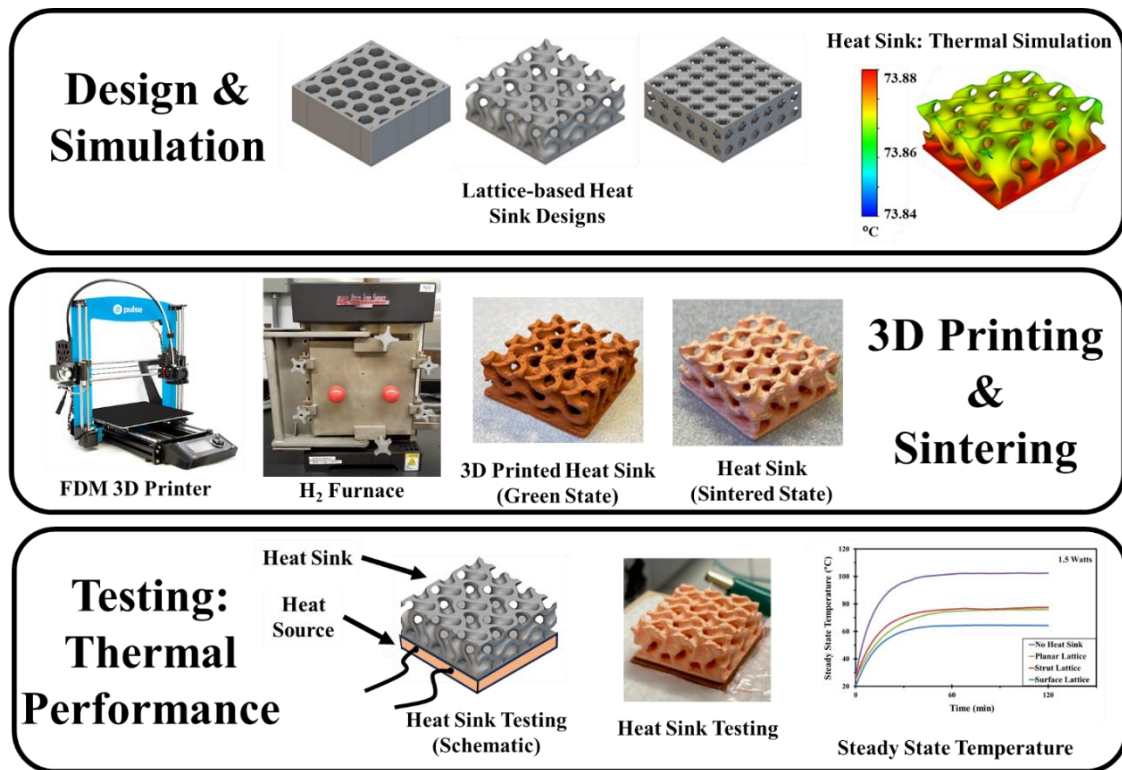
Figure 3.2 : Process schematic depicting a step-by-step approach starting from design and simulation of lattice heat sinks to 3D printing and sintering them via MEX technology followed by thermal performance testing of the fabricated lattice heat sinks

3.3 Results & Discussions

3.3.1 Feedstock and Filament Characteristics

The morphological features of as-received copper powders were confirmed by SEM and is shown as an inset in **Figure 3.3(a)**. The clear spherical morphology is indicative of the fact that these powders were processed via gas atomization. The powder was found to have 90% of the particles < 36μm based on the manufacturer's particle size distribution. The extruded metal powder-filled filaments were also analyzed for defects and other inconsistencies using SEM imaging along the cross-section and outer surface. As shown in **Figure 3.3(b)** and **Figure 3.3(c)**, the powder was found to be homogeneously dispersed in the polymer matrix with no noticeable presence of voids. The cross-section of

the filament was also found to be circular (∅ 1.75 ± 0.05 mm), and none of the filament

batches showed ovality or any deformation in shape.
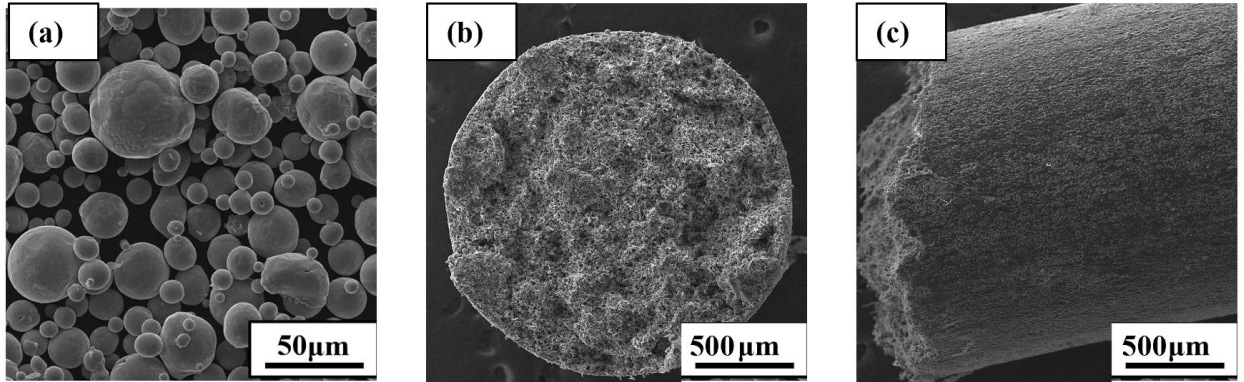
Figure 3.3: (a) SEM image of copper powder particles (b,c) SEM image of cross-section and side of extruded copper filament

3.3.2   3D Printed Heat Sinks: Green, Sintered, and HIPed

Heat sinks dissipate heat through conduction and convection. Increasing surface area enhances heat dissipation. Different lattice structure heat sinks were 3D printed with copper filaments. The anticipated performance of each lattice structure is as follows: Strut Lattice: Open channels allow air or coolant flow, ensuring effective cooling for linear flow paths. Surface Lattice: Wavy channels can create turbulence, maximizing contact area for improved heat transfer in non-linear flow paths. Planar Lattice: Closed sides direct airflow in a linear path, with the added weight/material in this lattice aiding conduction. optimizing heat transfer for controlled flow paths. 3D printed heat sinks that were subjected to sintering and HIP are shown in **Figure 3.4**. Post-sintering and HIPing, the planar lattice heat sink weighed 44 g, strut lattice heat sink weighed 28 g, and the surface lattice heat sink weighed 27 g. These weight variations are attributed to the different lattice configurations, each designed to serve specific heat dissipation needs.
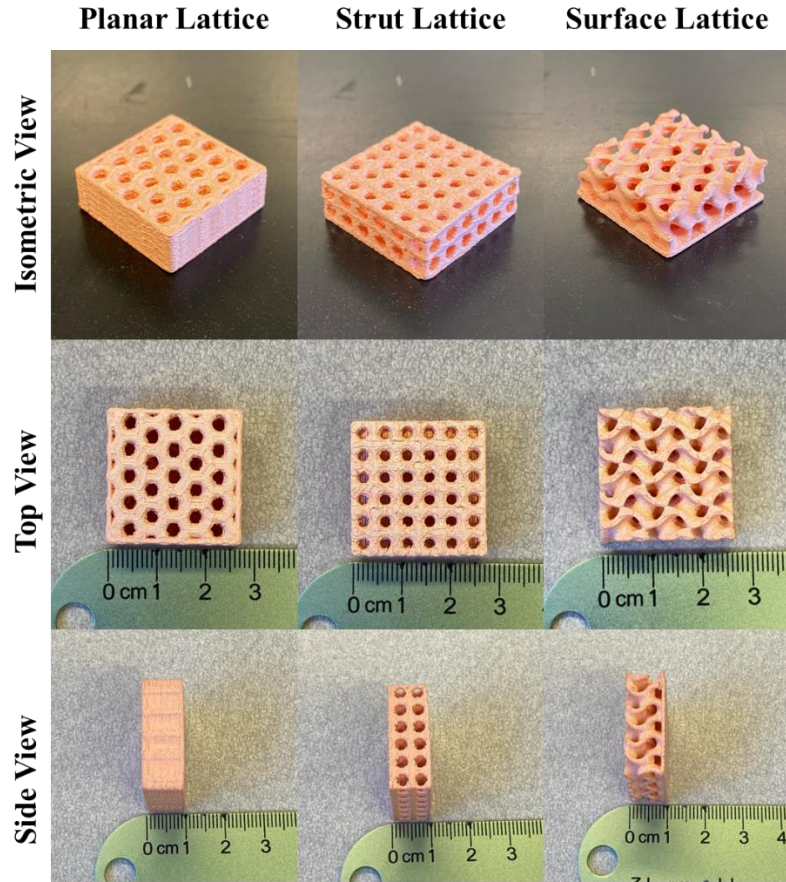
Figure 3.4 *: Isometric, top, and side view of planar, strut, and surface lattice heat sinks after sintering and HIPing*

Table 3.1 presents crucial data on the weight, surface area, density, linear shrinkage and electrical properties of the 3D printed, sintered, and HIP heat sinks. The surface area to weight ratios provides valuable insights into the effectiveness of each lattice in maximizing heat transfer. The planar lattice demonstrates a surface area to weight ratio of 1.7, while the strut lattice exhibits a ratio of 2.5, and the surface lattice achieves the lowest ratio of 2.9. These ratios highlight the relative effectiveness of each lattice design in dissipating heat and serve as a useful metric for guiding future heat sink optimization efforts. Notably, all the heat sinks demonstrate a density of 98% relative to pure copper, ensuring high material integrity. The linear shrinkage is a critical consideration during the

part design phase, necessitating oversizing of the parts to meet post-sintered and HIP dimension specifications accurately. The achieved HIP density of 98% surpasses that of commercially available Markforged bound metal copper filament 3D printing and other comparable studies using HIP and Copper with bound metal MEX 3D printing processes. Additionally, the outstanding 100% IACS values are comparable to those of wrought copper, highlighting the exceptional electrical conductivity properties of these 3D printed parts.

Table 3.1 : Density, Shrinkage, and Electrical Properties after HIPing

Lattice Type	Weight post-HIP (g)	Surface Area post-HIP (cm^2)	% Relative Density post-HIP	Electrical Conductivity post-HIP (%IACS)	% Shrinkage		
					X	Y	Z
Planar	44	76.5	98	100	16	16	17
Strut	28	71.2	98	100	16	16	17
Surface	27	78.4	98	100	16	16	33

3.3.3   Thermal Simulations

Steady state thermal results for all the heat sinks are presented in **Table 3.2**. It is important to highlight that the temperature scale bar is different for each geometry for clarity even though the energy input was 2 Watts. The result of the honeycomb geometry presents an asymmetric temperature distribution influenced by its geometry. The closed sides of the heat sink limit air circulation limiting convective pathways to remove heat, however, the thick walls improve conduction heat transfer allowing the heat sink to become the second-best performer of the tested geometries based on the ability of each heat sink to maintain a lower base temperature at constant heat input. Simulation results (**Table 2**) predict the ability of surface lattice to maintain a base temperature as low as 73.88°C at

2W power input, whereas the base temperatures for planar lattice and strut lattice are 82.4°C and 94.39°C respectively. Additionally, from the simulation results, we see that the strut lattice heat sink shows a homogeneous temperature distribution across its surface. However, the strut lattice is seen to exhibit higher equilibrium temperature than the planar lattice. This behavior is due to the fact that, although strut lattice has a more open structure compared to planar lattice, the surface area and the weight of the lattice is much lower compared to planar lattice.

Table 3.2 : *Thermal simulation results for 1-D, 2-D, and 3-D lattice heat sinks in isometric, top, bottom, and cross-sectional view at 2 Watts power input*
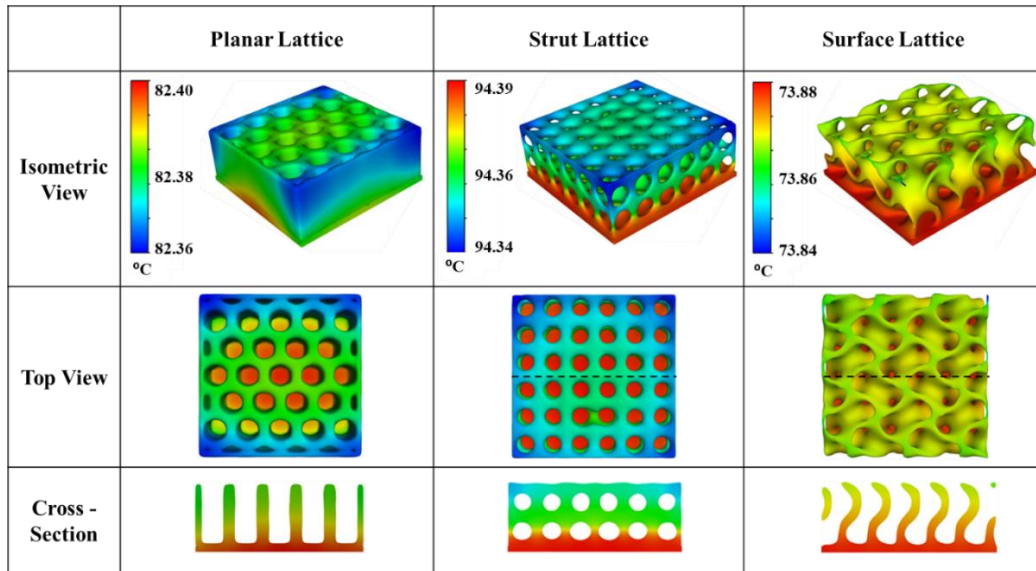
Therefore, although the heat sinks' performance is influenced by both conduction and convection, the effect of poor conduction due to lower surface area overshadows the positive influence of the strut lattice being an open structure. The simulation results of the surface lattice also show a homogeneous temperature distribution, and the performance of the surface lattice was seen to be the best amongst all the three types of lattice structures (planar, strut, and surface). The final steady-state operating temperature of the surface lattice is seen to be much lower than the other two geometries presented. We attribute this

behavior to an optimized balance between surface area, part weight, and conductive/convective methods of heat transfer. The geometrically optimized cavities of the gyroidal surface lattice allows the surrounding air to accelerate through the porosity improving heat transfer kinetics, and the performance of the heat sink in operation. These FEA simulations proved to be an efficient tool to predict heat sink performance of different lattice geometries under natural convection.

3.3.4   Experimental Results: Thermal Performance

Figure 3.5(a) depicts the temperature of the base of the heat sinks plotted over time with a constant power input of 1.5 W. Such measurements of base temperature and ambient temperatures were taken for all three types of 3D-printed lattices under three different heater powers (1W, 1.5W, and 2W). Notably, all heat sinks reached equilibrium temperature within 30-60 minutes after powering on the heat source, regardless of the input power. To evaluate their performance, the steady-state temperature of each heat sink was compared to the steady-state temperature achieved without a heat sink (**Figure 3.5(b)**). The results highlight the thermal behavior of the different lattice types under varying power inputs, showcasing their efficiency in maintaining lower temperatures at the base compared to the base temperature without any heat sink. Remarkably, the surface lattice heat sink consistently exhibited the lowest equilibrium temperature at the base, irrespective of the heater power. Although the steady state temperature (T_b) of the base remains lowest for the surface lattice heat sink at 1W, 1.5W, and also at 2W as seen in **Figure 3.5(b).** It is worth noting that this value is also dependent on the temperature of the ambient atmosphere (T_a) while testing these samples. To account for the ambient temperature and normalize it with the power input at the base,
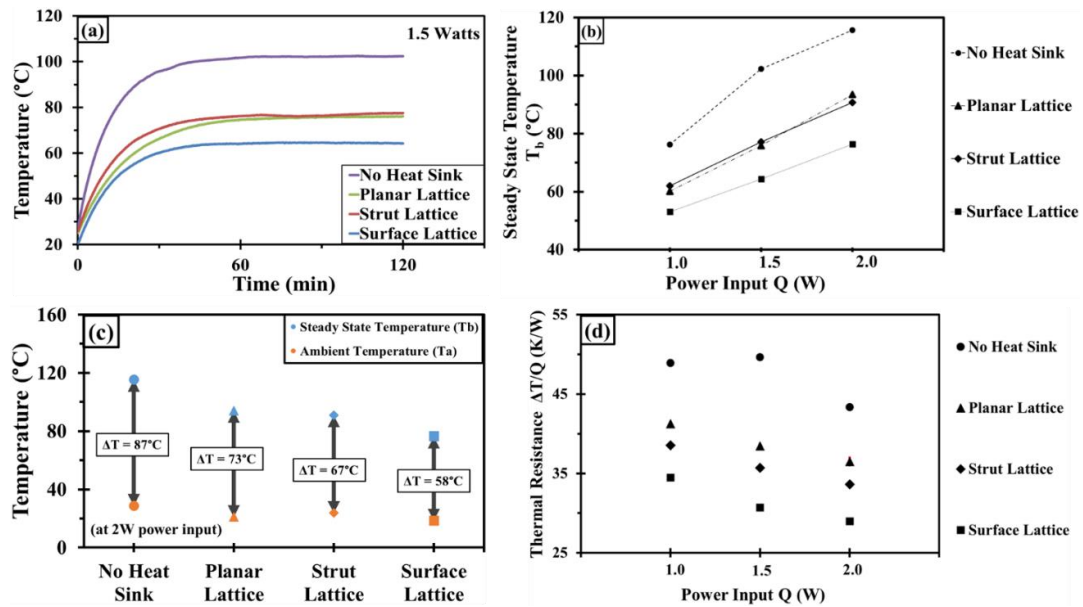
Figure 3.5 : *(a) Base temperature of each lattice heat sink as a function of time at 1.5W heater power (b) Steady state temperature (T_b) of the base of each heat sink at different heater power (c) Temperature difference (ΔT) between T_b and T_a for each heat sink at 2W power input (d) Thermal resistance (ΔT/Q) as a function of power input for different lattice heat sinks*

Figure 3.5(c) and represents the steady state temperature (T_b) as well as the ambient temperature (T_a) in one plot, while identifying the difference between steady state and ambient temperatures. This difference is denoted by ΔT and defined by the following equation.

$$ΔT = Tb - Ta$$ **……………………….…….. (Eq. 3.1)**

This temperature difference (ΔT) represents the equilibrium steady state temperature (T_b) of the base relative to the ambient temperature (T_a). A lower ΔT corresponds to higher heat transfer, which implies higher thermal performance as a heat sink. **Figure 3.5(c)** depicts temperature data for all three types of lattice heat sinks (planar, strut, and surface) under a 2W power input. It is observed that the surface lattice exhibits the lowest ΔT of 58°C, which is 50% lower than the ΔT without any heat sink, and 26% and 16% lower than the ΔT in planar and strut lattices respectively.

The thermal resistance was also calculated by normalizing the temperature difference (ΔT) with the power input for all three types of lattice heat sinks. The thermal resistance was calculated using the equation:

$$Thermal\ Resistance = \frac{\Delta T}{Q} \quad \text{.................... (Eq. 3.2)}$$

Where, $\Delta T = T_b - T_a$ (all temperatures in K); and Q is the heat input (1W, 1.5W, or 2W)

Figure 3.5(d) presents the calculated thermal resistance as a function of power input for each of the lattice heat sinks. The thermal resistance was observed to be constantly decreasing with increasing power (input heat flux) for all the lattice heat sinks, with the surface lattice heat sink showing the least thermal resistance. This decrease in thermal resistance with increasing input power is hypothesized to be due to the increasing effect of convection heat transfer with increasing temperatures at higher power inputs. The thermal resistance of surface lattice heat sinks was found to be lowest at any given power input. It was observed that the thermal resistance of surface lattice heat sink was 50% lower (on average) than that without any heat sink, and 25%, and 15% lower (on average) than the planar and strut lattices respectively. These observations highlight the importance of heat sink design and material choice in achieving efficient and stable thermal performance during various power inputs and heat transfer processes.

3.4 Conclusions

This study presents a comprehensive analysis of 3D printed heat sinks with various lattice configurations. The results provide valuable insights into their performance, material characteristics, and thermal behavior. The weight variations of the heat sinks offer essential information on the lattice structures, while the surface area to weight ratios demonstrate their efficiency in maximizing heat transfer. The 3D printed, sintered, and HIP

heat sinks exhibit high material integrity and achieve a density of 98% relative to pure copper, making them suitable for demanding applications. The linear shrinkage value emphasizes the need for careful consideration during the part design phase to meet precise dimensional specifications. The outstanding 100% IACS values underscore the excellent electrical properties of the 3D printed heat sinks, making them a promising choice for applications where electrical conductivity significantly impacts performance. This opens up new possibilities for innovative heat dissipation solutions in various industries.

Thermal performance analysis shows that 3D printed lattices outperform conventional heat sinks in maintaining lower base temperatures, with the gyroid heat sink proving to be the most effective among the designs tested. Optical images reveal distinctive surface textures resulting from the layer-by-layer stacking, with the gyroid heat sink displaying a notably higher surface area. Moreover, the efficient temperature distribution along the Z-direction enhances the overall thermal performance of the 3D printed heat sinks, making them highly effective in dissipating heat. Overall, this study highlights the potential of 3D printed heat sinks with different lattice designs to revolutionize heat dissipation technologies. Their superior thermal performance, material integrity, and customizability make them a promising solution for various cooling applications in industries such as electronics, aerospace, and automotive. As the field of additive manufacturing continues to evolve, further optimization and research hold the promise of even more efficient and innovative heat sink designs. The insights gained from this study will guide future advancements in 3D printing technology, paving the way for more effective and sustainable cooling solutions in the years to come.

CHAPTER 4: MAPPING 3D PRINTED PART DENSITY AND FILAMENT FLOW CHARACTERISTICS IN THE MATERIAL EXTRUSION (MEX) PROCESS FOR FILLED AND UNFILLED POLYMERS

4.1 Introduction

The bound metal powder-polymer 3D printing process, often referred to as Material Extrusion (MEX), presents a promising avenue for the fabrication of metal and ceramic components. This process utilizes a high metal powder solids loaded bound powder-polymer filament, typically exceeding 50 vol.% or 80 wt.% equivalent, as its raw material [6,14,40]. However, it's important to note that the polymer in this filament primarily serves the purpose of binding the metal or ceramic powder particles together. To achieve the desired dense metal or ceramic parts, additional post-processing steps, including polymer removal through debinding and powder compaction and densification via sintering, are necessary. Therefore, maintaining nearly 100% printed part density is paramount for bound powder-polymer filaments, as any porosity introduced during printing can result in compromised mechanical properties after the sintering process. This study delves into the intricate interactions between material properties and the 3D printing process with the focus on bound powder-polymer filaments, focusing on achieving dense parts, and comparing its processing behavior to traditional unfilled polymer filaments. There are many material-process challenges in working with bound powder-polymer filaments in

contrast with unfilled polymers systems used in MEX 3D printing. Primarily, the intrinsically limited mechanical and unfavourable rheological characteristics that occur as the bound powder-polymer filaments are highly loaded with powder content, typically, >50 vol% that give rise to a set of challenges [41,42]. These include a notable reduction in printing speed, frequent filament breakage, and erratic material flow during extrusion, often culminating in unsuccessful prints and subpar part quality [43–45]. Therefore, we focused to understand and review the literature in bound powder-polymer MEX 3D printing process to identify the past work that has been performed to identify the material-process interactions that yield nominally extruded high density green parts and identify gaps in the literature that have not been addressed so far (**Table 4.1**).

Table 4.1 : *Past literature studying the effects of viscosity, filament properties, and process parameters on the density of parts 3D printed using unfilled/filled polymer systems*

Reference	Year	Material Viscosity	Filament Mechanical Properties	Process Parameters (Flow rate, print temp, print speed, pressure drop)	Density of Printed Part	Comments
[46]	2000	✓	✓	No	No	Compressive elastic modulus vs. viscosity
[47]	2004	✓	No	✓	No	Liquefier dynamics (flow rate, pressure-drop, & force) in FDM
[48]	2007	✓	No	✓	No	Mathematical modelling and FEA of melt flow behavior in extrusion 3D printing
[44]	2014	✓	✓	✓	No	Review paper on process design and modelling in FDM.

[42]	2016	✓	No	No	No	Viscosity prediction models for MIM feedstocks
[49]	2017	✓	✓	No	No	Identified role of viscosity and elastic modulus in filament failure via buckling or back-flow
[50]	2017	✓	No	✓	No	Effect of (nozzle temp., print speed, layer ht.) on mass flow rate (dependent on viscosity)
[51]	2018	✓	No	✓	No	Rheology and Heat transfer effects in FDM
[52]	2018	✓	No	✓	No	Optimized analytical melting model for material extrusion AM
[53]	2019	✓	No	✓	No	In-line rheological monitoring and effect on pressure across nozzle
[54]	2019	✓	No	✓	No	Nozzle design that enables in-situ measurement of temperature and pressure
[55]	2020	✓	✓	✓	✓	Printability studies of Ti-6Al-4V. However, does not consider back-flow and back pressure. Also, it is specific to a single material system.
This Paper	2023	✓	✓	✓	✓	Elucidates the influence of materials viscosity, filament type, and process parameters on printed part density.

In several studies, the significance of viscosity in the context of 3D printing processes was underscored. For instance, Venkataraman et al. delved into the intricate

correlation between viscosity and the feasibility of filament printing, identifying a specific range of shear rates conducive to successful extrusion based on the viscosity-to-stiffness ratio [46]. However, the finer nuances of this ratio, a pivotal factor in achieving the high-density 3D printed parts, were left unexplored. Similarly, Gonzalez-Gutierrez et al. conducted a comprehensive review of models designed to predict viscosity in polymeric blends and suspensions [56]. However, they did not delve into the repercussions of viscosity on part density. Similarly, while mechanical properties of printing materials have been discussed in various papers such as Venkataraman et al. [46], which studied ceramic and metal powder-polymer systems. Turner et al. highlighted the interdependencies between material properties like modulus and viscosity with shear rates and pressure drop [44,45]. However, in the studies by Venkataraman et al. and Turner et al., the relationship between these properties and part densities remains an underexplored aspect of the process [44–46].

As mentioned before, one key challenge with working with bound powder-polymer filaments is the high solids loading (>50vol. %) is its rheological properties that are often not conducive to printing at higher print speeds. Several studies, such as Venkataraman et al., have explored the relationship between viscosity and the ability to print filaments but didn't delve into the specifics crucial for achieving high-density 3D printed parts [46]. They identified a range of shear rates where filaments could be successfully printed based on the viscosity-to-stiffness ratio. However, they didn't delve into the specifics of this ratio, which is crucial for achieving high-density 3D printed parts. Similarly, Gonzalez-Gutierrez et al. reviewed models for predicting viscosity in polymeric blends and suspensions but didn't consider the effects of viscosity on part density [56]. The mechanical properties of printing

materials were discussed in various papers. Venkataraman et al. studied ceramic and metal powder-polymer systems, focusing on their mechanical properties [46]. Turner et al. highlighted the interdependencies between material properties like modulus and viscosity with shear rates and pressure drop [44,45]. However, these studies didn't extensively explore the relationship between material properties and part densities, which is vital for producing high-quality printed components. Therefore, mapping viscosity in bound powder-polymer filaments is critical for consistent 3D printing, as it affects the material's flow behavior through the MEX 3D printer nozzle.

On the other hand, process parameters play a crucial role in bound metal 3D printing, as demonstrated in several papers. For instance, typical print speeds for metal MEX are around 30 mm/s [55], while polymer MEX 3D print speeds can reach over 100 mm/s [57]. In MEX 3D printing, the filament behaves as a ram and is pushed while it melts inside the liquefier and extruders out of the nozzle. Therefore, low-modulus filaments start to buckle with an increase in print speed (as the force with which the filament is pushed is increased). For highly filled powder-polymer filaments, where typical solids loading is above the percolation threshold, the stiffness is lower, and viscosities are higher than for pure polymer filaments [55]. Specifically, filaments with high powder can reduce the Young's modulus by two orders of magnitude. For instance, ~1500 MPa for pure 1.75 mm diameter PLA filament to ~70 MPa for ~55 vol.% Ti-6Al-4V powder in PLA. Alternatively, highly elastomeric materials such as TPU or TPC have 8X lower stiffer than PLA [58]. Therefore, print speed limits are highly dependent on the mechanical properties of the filaments. Interestingly, no study on print speed and its interrelationships with material properties for bound metal MEX 3D printing is currently there.

However, there have been attempts to investigate some of the print speed effects for unfilled polymer MEX 3D printing. For example, Duddleston et al. emphasized the significance of process parameters like nozzle diameter, print speed, layer height, and nozzle temperature on extrusion rates [50]. David Phan et al. and Tim Osswald et al. delved into heat transfer and nozzle dynamics [51,52,59]. However, these papers didn't thoroughly address how mechanical properties of filaments influence green part densities or the correlation between process conditions and viscosity. Additionally, the print temperature is typically raised to prevent filament buckling, breakage, and nozzle clogging while printing at higher print speeds. The increase in temperature helps lower polymer viscosity allowing for a continuous flow [42–45,53,60–62]. However, print temperatures cannot be increased by much since the polymer starts degrading over a particular temperature range. Therefore, the majority of previous studies of pure polymer systems and low-concentration polymer composites modelled liquefier geometry to determine the pressure drop at the nozzle exit and filament failure criteria along with governing rate limits for printing that included elastic modulus/viscosity ratios and extrusion forces required for successful printing [46–49,54,63,64] but only two studies have reported filament behavior for ceramic fused filament fabrication [46,64].

From **Table 4.1**, none of the papers investigating the interdependence of material viscosity, mechanical properties of the filament, and their impact on 3D printing speed with the goal of achieving 100% part density and specifically for bound powder-polymer filaments based 3D printing research most of the focus is only on demonstrating that the part can be 3D printed and sintered and find out what are the ensuing mechanical properties post sintering. These papers primarily focus on various aspects of 3D printing, including

viscosity, mechanical properties, and process parameters, but they do not appear to delve into the specific interplay between these factors and the pursuit of achieving full part density at different printing speeds. Currently due to this limited understanding, the design of metal and ceramic-bound filaments is stunted to a limited material portfolio due to challenges in understanding the flow inconsistencies and filament breakages that lead to print defects. Although low solids loading can make extrusion easier, it poses sintering challenges such as high shrinkage, slumping, and low dimensional tolerances. In contrast, excessively high solids loading can result in high extrusion forces, filament breakage, printing failure, and poor extrusion due to high viscosity [55]. Therefore, it is imperative to understand the relationship between material viscosity, mechanical properties, and printing speed, especially in the context of optimizing for full part density, is a complex and multifaceted aspect of 3D printing that may require further research and experimentation to fully understand and model.

Therefore, this paper focused on PLA, TPU, and bronze filled metal powder-bound filaments, each with extreme variation in filament mechanical and rheological properties. This variation can affect the print speed and the ensuing part density obtained, so we studied the influence of mechanical, thermal, and rheological properties on attaining a printed part density of $100\pm5\%$ for each material type. Our findings show that continuous material flow across the nozzle, the volume of material extruding from the nozzle, and maximizing inter-layer bonding while preventing filament failure or buckling are crucial in achieving the desired density. To understand this process-property variation, we measured the force required to overcome pressure drop and the volumetric flow rate of each material, correlating it with the material viscosity and strength. We created process

47

maps of density and viscosity for each material type for various volumetric flow rates resulting from changing the 3D printing process conditions. Our study also created and compared the process maps for bound metal filaments with the unfilled PLA and TPU systems to understand the zones where all materials print at 100±5% density. A full factorial design of experiments was performed, and ANOVA analysis was conducted to identify the effect of print conditions on measured variables such as print density, volumetric flow rate, and force required to overcome the pressure drop. Regression analysis was used to determine which process variable affects volumetric flow rate and part density. Overall, this study provides crucial insight into the 3D printing process of polymer filaments, highlighting the importance of adjusting printing conditions for different materials. Our results can aid in new material design and discovery for bound metal filaments that have stagnated due to a limited understanding of their mechanical and rheological property interactions and the ensuing challenges in achieving near 100% dense parts.

4.2 Materials and Methods

4.2.1 Methodology

In the process of developing process maps and identifying statistical models for predicting the behavior of different material systems processed via Metal MEX 3D printing, multiple steps were performed as shown in **Figure 4.1**. A variety of material systems, based on their intrinsic properties were selected and extruded into filaments. Thermal, rheological, and mechanical properties of each of these material systems were measured before passing them for 3D printing. In order to understand the behavior of these filaments while 3D printing multiple measurements and calculations were performed to

identify the volumetric flow rate, pressure drop, and force across the nozzle. These parameters would later help delineate the cause and effect of print failures.
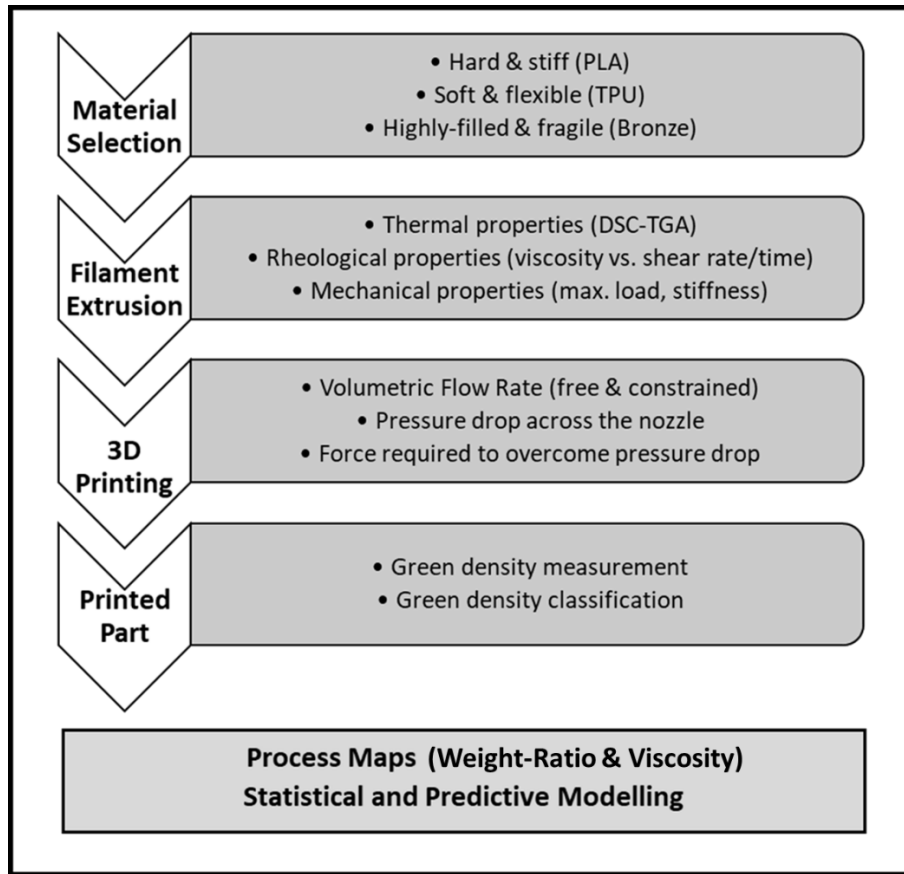
Figure 4.1: *Flow chart outlining the approach adopted by the authors for developing process maps and statistical models*

Finally, to correlate the 3D printed parts' quality with independent variables such as print speed, print temperature, and material type, a dimensionless number (based on part weight) called the "weight-ratio" of each 3D printed part was measured and classified. This weight-ratio (WR) is expressed as a percentage and is defined as:

$$\text{Weight-Ratio (\%)} = \frac{Actual\ Weight\ of\ 3D\ Printed\ Part\ (g)}{Theoretical\ weight\ (g)}\ X\ 100$$

Where, the theoretical weight is calculated using the density of the material and the theoretical volume of the 3D printed part (based on CAD model). This weight-ratio is a

measure of whether a part is over-extruder (WR>105), under-extruded (WR<95), or nominally extruded (95<WR<105).

4.2.2   Materials

To understand how variation in material type (filled and unfilled polymers) and its material properties play a role in understanding the rate limits for MEX 3D printing three types of representative materials were selected. Specially, PLA (BCN3D, 1.75mm filament) and TPU (NinjaTek NinjaFlex, 1.75mm filament) were chosen to represent rigid and highly elastic filament materials [65,66] . Whereas a custom 92 wt.% bronze filament was formulated to represent highly filled powder-polymer filaments used for printing metal with MEX 3D printing. In such a case, the highly filled powder-polymer filaments are 3D printed and subsequently postprocessed via debinding and sintering to remove polymer and obtain dense metal parts.   Therefore, the present work utilizes two unfilled polymeric filaments: PLA, TPU, and one highly filled bronze filament with 55 vol.% solids loading

Bronze powders (Kymera International, Durham, NC), with a median particle size of 150μm were utilized to prepare the feedstock used for this study. A proprietary binder used for feedstock preparation was composed of three components: a backbone polymer (30–50wt%), an elastomer (20–30wt%), and a plasticizing phase (20–40wt%). The elastomer provides flexibility to the filament such that it can be spooled into coils for the ease of printing and storage. At the same time, the plasticizing phase helps decrease feedstock viscosity and improve overall metal powder loading into the binder matrix. Bronze powder loading of 55 vol% was selected for preparing the feedstock filaments for further metal MEX print processing. The powder-binder mixture was blended and introduced at 180 °C, followed by mixing with a rotating speed of 50 rpm. This powder-

binder mixture was blended for 45 min until the torque is stabilized, which signified mixture homogeneity. The blended mixture obtained from the torque rheometer were subsequently ground into smaller pellets (Plastic and Rubber Chopper PRC22-N180, Col-Int Tech, South Carolina, USA). This 55 vol% bronze feedstock pellets were extruded into flaments with a consistent diameter of 1.75±0.05 mm using a capillary die with an L/D ratio of 30mm:1.75 mm on a capillary rheometer (Rheograph 20, GÖTTFERT Werkstof-Prüfmaschinen GmbH, Germany). The extrusion temperature was chosen to be 135 °C with a uniform extrusion speed of 0.1 mm/s to obtain a filament of smooth surface finish and consistent diameter. With a good understanding of the materials used and the filaments fabricated from each of this material system, it was important to identify a range of parameters at which these filaments were to be 3D printed.

4.2.3   Design of Experiments

To identify the effect of 3D printing parameters on weight-ratio and viscosity, an experimental matrix was designed to inculcate a range of extrusion temperatures and print speeds for each material while maintaining all the other print parameters constant. A set of 5 different print temperatures (210, 220, 230, 240, 250 °C), and 6 print speeds (5, 10, 20, 30, 40, 50 mm/s) were chosen for experimentation. All the three materials (PLA, TPU and Bronze) were processed using a desktop 3D printer (Pulse from MatterHackers fitted with a Bondtech extruder) at each combination of these print temperatures and print speeds. A 0.4mm diameter nozzle was used for the experiments. Solid cubes of dimensions 20mm X 20mm X 2mm were printed at each combination of print parameters to determine the green part density of each material printed at different processing conditions. The weight-ratio was calculated as a ratio of the measured weight of the printed part to the theoretical weight

of the part. The theoretical weight was defined to be the weight of the cube based on the pycnometric density of the material printed and the volume calculated from the dimensions of the 3D printed cube.

4.2.4   Material Characterization

Additionally, thermal, mechanical and rheological characterization was performed to understand the properties of each material feedstock. The as-received bronze powders and filaments were characterized for true densities. The true density (ρ) was measured using a helium gas pycnometer (Accupyc II 1340, Micromeritics Inc., GA, USA). The thermal characteristics of each material was analyzed by collecting DSC-TGA data which was generated using a thermogravimetric analyzer (TGA, SDT Q600, TA Instruments, New Castle, DE, USA). Thermogravimetric analysis (TGA) and differential scanning calorimetry (DSC) experiments were performed on PLA, TPU, and 55 vol.% bronze feedstock, at a heating rate of 5 °C/min up to 600 °C in N_2 atmosphere. The mechanical properties of the filaments, especially under compressive loading was evaluated by measuring the maximum compressive load that each filament can sustain. Filament of each material was subjected to compression testing (Instron 5569 Universal Testing Machine, Norwood, MA, USA) using a 50kN load cell while maintaining a constant crosshead spped of 0.5mm-min^{-1}. Viscosity of all three feedstocks was measured at 5 different print temperatures in the shear rate range of 20 s^{-1} to 800 s^{-1} using a capillary rheometer (Rheograph 20, GÖTTFERT Werkstof-Prüfmaschinen GmbH, Germany) with a tungsten carbide die (L/D ratio of 30:1). The apparent shear rate was adjusted with Rabinowitsch-Weissenberg correction to account for the actual shear rate at the wall [67].

4.3 Mathematical Modelling

In order to identify the theoretical values for parameters such as volumetric flow rate, pressure drop across the nozzle, and force required to overcome the pressure drop, certain mathematical calculations and models were used in this study. Multiple researchers in the past developed different mathematical models to calculate these parameters. Numerous assumptions were made while utilizing these models and most of these assumptions were based on the need to simplify calculations while ensuring that the calculated values are as close to experimental values as possible. This work utilized mathematical models suggested by researchers in the past, while understanding and reviewing the assumptions made to calculate the parameters theoretically.

4.3.1   Past Mathematical Models

One of the first models was published in 2004 by Bellini and Güçeri [47], where they related the material flow to the pressure within the nozzle. In their model, the incoming filament acts as a piston that pushes the polymer melt through three distinct nozzle zones, while assuming that the polymer filament is in the melt state once it enters the nozzle. In 2008, Ramanath et al. published a research article, in which they modelled the melt flow of poly-ε-caprolactone across a nozzle [48]. In their analysis, they used the finite element method to model the flow and heat transfer within 5 distinct nozzle zones. Their model included two additional zones as compared to the model by Bellini et. al., which included the heating conduit that precedes the nozzle. A review paper by Turner et al. in 2014, re-emphasizes Bellini and Güçeri's model as a standard approach in identifying the driving force for material flow across the nozzle in FDM systems [44,45]. A research article by Heller et al. later in 2016 focussed on simulating the flow within the extrusion nozzle to

predict fiber orientation within the deposited bead during printing [68]. Most of these models [44,45,47,48,68] are based on the premise that the polymer melts as soon as the filament enters the nozzle.

More recently in 2018, Osswald et. al. discussed the validity of prior models based on the fact that those approaches are only valid in cases where sufficient time is available to melt the filament as it travels through the heated nozzle, which translates to very low print speeds [62]. Their paper presented a model that included a limiting case scenario where, at high print speeds, the melting rate controls the rate of the material flow across the nozzle. In this model, the material melts at the bottom of the larger diameter nozzle, forming a small melt film on the surface of the conical section. The pressure within the melt film acts as a driving force, squeezing the melt toward the center and out through the capillary. This model was shown to be useful for optimizing the melting within a material extrusion additive manufacturing process, and for addressing the material flow rate at higher print speeds.

Typically, the metal MEX feedstocks were seen to exhibit shear-thinning behavior, where viscosity decreases with increasing shear rate [55,56,64] Material flow properties were determined by applying the power law of Ostwald and de Waele for non-Newtonian fluids (shown in **Eq. 4.1**) to the viscosity measurements. Here, γ is the shear rate, τ is the shear stress, ϕ is the material fluidity, and m describing material flow characteristic and its deviation from the Newtonian flow. These flow parameters further enable calculating the shear rate and pressure drop at the nozzle.

$$\dot{\gamma} = \ \Phi.\tau^{m} \qquad \text{……………………...…………. (Eq. 4.1)}$$

4.3.2   Volumetric Flow Rate Calculation

The volume throughput of a material passed through a 3D printer under specific process parameters is quantitatively defined using the volumetric flow rate (Q). The ideal volumetric flow rate (Q_{ideal}) was estimated using mass conservation law (assuming the melt is incompressible), wherein the volume of material pushed into the liquefier is equal to the extrudate volume at the nozzle exit [55,69]. Q_{ideal} was measured using **Eq. 4.2** where, A_1 is the cross-sectional area of the filament having diameter 1.75 mm, and A_2 is the cross-sectional area at the nozzle exit having a diameter 0.4 mm. v_1 is the feed rate at which filament is pushed by pinch rollers into the liquefier and v_2 is the exit velocity of the extrudate as it leaves the nozzle.

$$Q_{ideal} \text{ (cc/s)} = A_1 v_1 = A_2 v_2 \quad ....(Eq. 4.2)$$

The ideal case scenario however, is virtually non-existent and the actual volumetric flow rate in almost all cases is lower than the Q_{ideal}, due to the affect of pressure drop across the nozzle and the force required to overcome this pressure drop for successful extrusion. To account for the pressure drop across the nozzle and to identify the actual volumetric flow rate for a given material at specific process conditions, volumetric free flow rate (Q_{free}) was measured. This method of measuring Q was assumed to mitigate the influence of non-steady state extrusion caused by pressure build-up in the nozzle [50], and was incorporated by researchers in the past [55,69]. In this work, material was freely extruded with the nozzle raised a few centimeters above the build platform by programming the software feed a constant length of filament (500mm) into the extruder using the feed rollers. Each material (TPU, PLA and Bronze) was extruded using a commercial FFF printer (Pulse from MatterHackers fitted with a Bondtech extruder) at different print temperatures (210°C to

250°C) and print speeds (5mm/s to 50mm/s). Extrudates from each experiment was

collected in an aluminum crucible as shown in **Figure 4.2(a)** and weighed, while repeating

each experiment at least three times to determine the average weight while ensuring

repeatability. The flow rate was calculated using **Eq. 4.3**.

$$Q\left(\frac{cm^3}{s}\right) = \frac{Extrudate\ mass\ flow\ rate\ (\frac{g}{s})}{Material\ density\ (\frac{g}{cm^3})} \quad \text{.............. (Eq. 4.3)}$$

Although the volumetric free flow rate (Q_{free}) provides valuable data on the volume

throughput of material passing through a nozzle at a given temperature and speed, it does

not account for the back-flow pressure experienced by the extrudate while being deposited

on an existing 3D printed layer. Annular back-flow and filament buckling are known to be

the two primary failure modes during extrusion via FFF [46,49,59]. The filament acting as

a piston to drive the liquid polymeric material out of the nozzle is usually not perfectly

flush with the liquefier wall, causing the heated polymer to flow back up the annular region

between the filament and the liquefier wall, causing additional back-pressure across the

nozzle that further inhibits material flow [49]. More often than not, the back-pressure was

seen to be a significant and cannot be neglected. To simulate such a scenario which can

account for the back-pressure experienced by the extrudate, and to compare it with the

volumetric flow rate measured by free extrusion (Q_{free}), an alternate method was inculcated.

A single walled- perimeter with 0% infill and one perimeter with 10 layers stacked on top

of each other as shown in **Figure 4.2(b)**. was printed with each material (PLA, TPU and

Bronze) at different print temperatures and print speeds and weighed to measure the mass

of the part. The volumetric constrained flow rate ($Q_{constrained}$) was calculated using **Eq. 4.3**

as mentioned before. This technique ensured that the volumetric flow rate of a material at

specified print temperature and print speed was measured in a constrained flow condition.
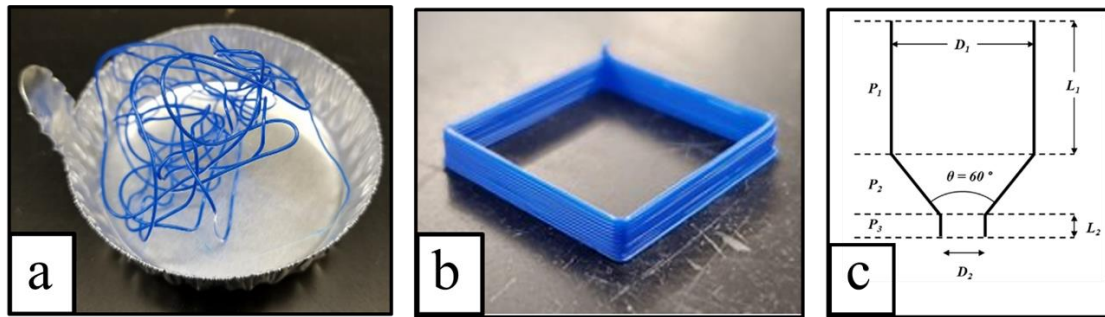
Figure 4.2 : Samples collected to measure the volumetric flow rate (Q) using two methods: (a) 500mm extrudate collected in an aluminum pan (b) single-walled cube (c) Pictorial representation of the nozzle divided into three sections to calculate pressure drop

4.3.3 Calculating Pressure Drop and Force Across the Nozzle

The pressure drop estimations were performed for the liquefier nozzle geometry with varying flow rates corresponding to the filament feed rates between 0.5 mm/s and 16 mm/s. The total pressure drop (P) was estimated to be the summation of P1, P2, and P3, which are the pressure drops in the three different sections of the liquefier/nozzle region shown in *Figure 2(c)*. The pressure drop in the three sections of the liquefier was estimated by performing momentum balance in conjunction with the power-law viscosity models [44,47,48,54], **Eq. 4.4**, **Eq. 4.5**, **Eq. 4.6** and **Eq. 4.7**. Some of the key assumptions in these models include: melt is incompressible and isothermal, there is a no-slip boundary condition at the wall, and the flow is fully developed, steady-state, and laminar [70].

$$P_1 = 2L_1 \left[\frac{Q(m+3)}{\pi\Phi\left(\frac{D_1}{2}\right)^{m+3}} \right]^{\frac{1}{m}} \quad \text{.....................} \text{(Eq. 4.4)}$$

$$P_2 = \frac{m}{3\tan\left(\frac{\theta}{2}\right)} \left(\frac{1}{D_2^{\frac{3}{m}}} - \frac{1}{D_1^{\frac{3}{m}}} \right) \left(\left[\frac{Q}{\pi\Phi}\right][m+3]2^{m+3} \right)^{\frac{1}{m}} \quad \text{.........} \text{(Eq. 4.5)}$$

$$P_3 = 2L_2 \left[\frac{Q(m+3)}{\pi\Phi\left(\frac{D_2}{2}\right)^{m+3}} \right]^{\frac{1}{m}} \quad \text{..........................} \text{(Eq. 4.6)}$$

57

$$P = P_1 + P_2 + P_2 \quad \dots\dots\dots\dots\dots\dots\dots \quad \text{(Eq. 4.7)}$$

Q is the volumetric flow rate for the extrudate leaving the nozzle as defined in

Section 3.2. L1 and D1 are the length and diameter at the entrance section, which are

measured 10.5 mm and 1.75 mm, respectively, and L2 and D2 are length and diameter at

the exit section which are 0.6 mm and 0.4 mm, respectively. And θ is the nozzle angle

(60°). The material constants m and φ were determined from the experimentally measured

viscosity data. While using **Eq. 4.4** to **Eq. 4.7** for calculating the pressure drop across the

nozzle, the volumetric flow rates used were that of both free and constrained flow measured

from free extrusion of material and 3D printed single-wall perimeters respectively. To

overcome the pressure drop P in **Eq. 4.7**, a force, F is required to achieve successful

material extrusion, which can be calculated with **Eq. 4.8**, where $A_{filament}$ is the area of

filament cross-section at entry.

$$F = P \times A_{filament} \quad \dots\dots\dots\dots\dots\dots\dots\dots \quad \text{(Eq. 4.8)}$$

Figure 4.3 outlines the roadmap to calculating and collecting all the data that was

used in developing these statistical models. Independent variables (material type, nozzle

temperature, and print speed), measured variables (volumetric flow rate, and viscosity), as

well as constant variables such as nozzle dimensions were taken into account to calculate

pressure drop and force across the nozzle for different combinations of independent

variables. The effect of independent was analyzed using ANOVA, before identifying

logistic and multiple variable regression models to predict the weight-ratio and viscosity.
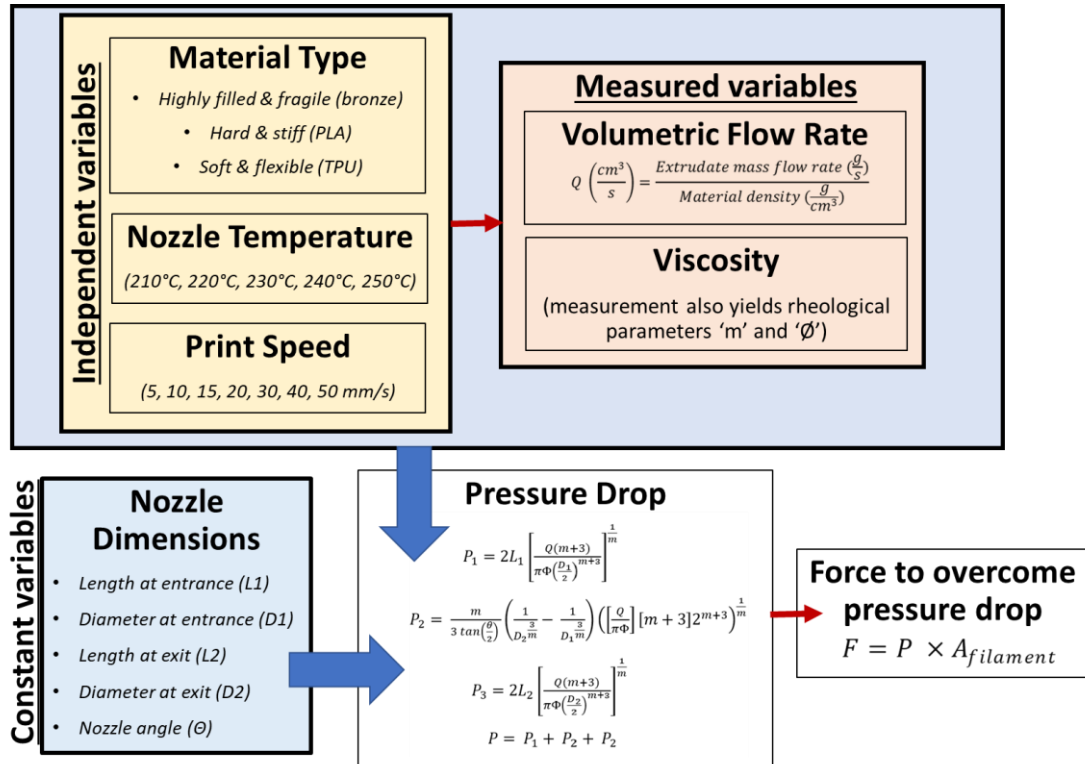
Figure 4.3 : Roadmap outlining the independent variables, constant variables, and mathematically calculated parameters for experimentation and modelling

4.4 Results and Discussion

4.4.1   Filament Characteristics

Figure 4.4(a) represents the DSC analysis of all the three feedstocks (PLA, TPU and Bronze) used in this study. PLA and TPU filaments were as-received and were 3D printed in the range of 210°C to 250°C. Bronze filament on the other hand was manufactured in-house, where bronze powders were blended with a polymeric mixture at 180°C to make the feedstock that is further extruded at 135°C. DSC analysis in **Figure 4.4(a)**, clearly delineates the enthalpy changes associated with glass transition temperature (T_g) and polymer degradation for all three material systems. Polymer degradation was seen to be evident at temperatures beyond 280°C, whereas the glass transition temperatures of all the polymer was under 100°C. The processing temperatures to fabricate the feedstock

and 3D print the filaments was carefully chosen, ensuring no polymer is thermally degraded.
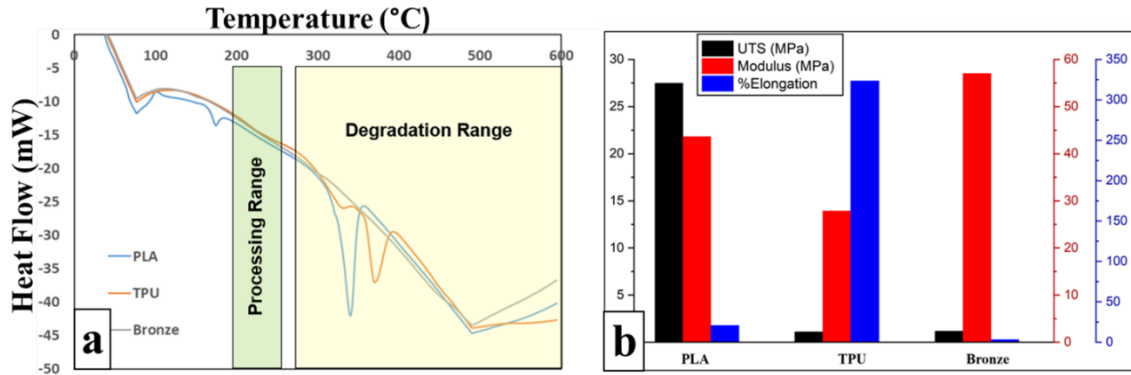
Figure 4.4: *(a) Differential Scanning Calorimetry (DSC) of PLA, TPU and Bronze filaments (b) Mechanical testing results of PLA, TPU and Bronze filaments*

Figure 4.4(b) reveals the mechanical testing data for the three filaments under compressive loading. The behavior of filaments under compressive loading was especially important as it simulates the loading condition of the filaments during 3D printing. In a Fused Filament Fabrication (FFF) set-up, the feed rollers initiate the drive mechanism that delivers filament material into the heated nozzle. As pointed by multiple researchers in the past [44,47], the filament is under tensile stress upstream to the roller and under compression, in the region between the roller and the heated nozzle. This is understood to be due to the external force applied by the feed rollers on the filament to push more material into the heated nozzle or liquefier, which is counter-acted by the resistance to flow generated due to the viscosity of the melt material in the liquefier. This compressive stress therefore, is the driving force behind the extrusion process.

4.4.2 Volumetric Flow Rate (Q) Characteristics

Figure 4.5 integrates the volumetric flow rate (Q) values measured in free and constrained flow conditions as a function of print speed and extrusion temperature for each material. Line plots represent the volumetric free flow rate (Q_{free}) and bar plots represent volumetric constrained flow rate ($Q_{constrained}$).
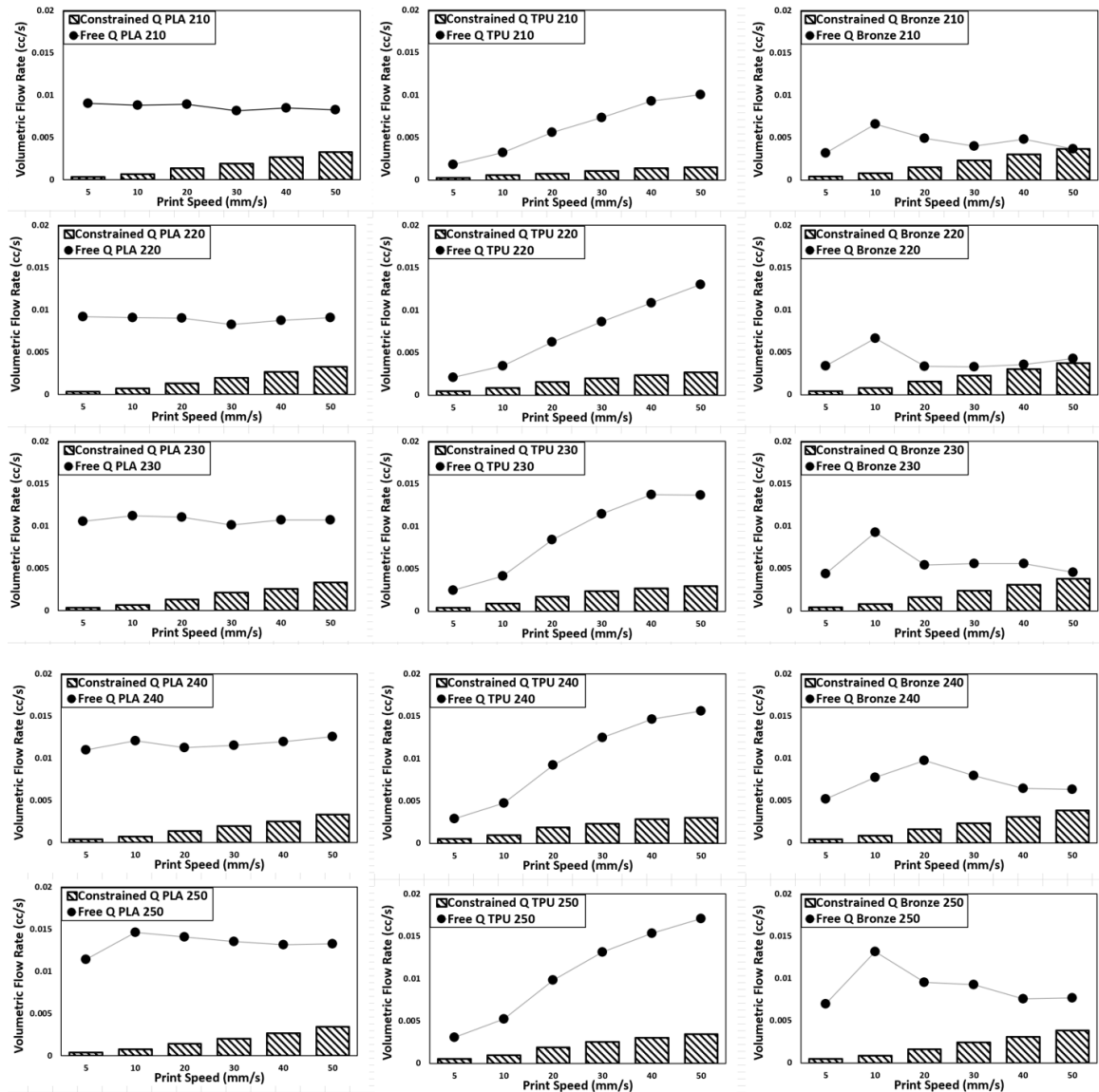
Figure 4.5 : *Volumetric flow rate (Q) of PLA, TPU and Bronze measured at different print temperatures and print speeds in both free and constrained conditions*

The material throughput in free flow conditions is evidently higher than in constrained flow, owing to the back pressure inhibiting free material flow across the nozzle. Volumetric flow rates (both free and constrained) showed a general increasing trend with increase in feed rate and extrusion temperatures. This abides with intuition, where a higher feed rate suggested higher material input across the nozzle, while higher extrusion temperature suggested lower viscosity of the melt in the liquefier owing to the shear thinning behavior of the feedstock.

4.4.3　　Pressure-drop and force across the nozzle

Figure 4.6 represents the pressure across the nozzle plotted against print speed for each material at different extrusion temperatures. The bar plots indicate the pressures calculated assuming constrained flow rate conditions whereas the line plots represent pressure drop in free flow condition. It was observed that the volumetric flow rate has a direct impact on measure the pressure drop across the nozzle and therefore, it is pertinent to identify the volumetric flow rate that closely resembles actual 3D printing conditions. **Figure 4.6** also shows a predominant difference in pressure drop calculated in free flow and constrained flow conditions, re-emphasizing and validating the importance of back-pressure. Additionally, the back pressure could be calculated as the difference between pressures calculated using free and constrained flow conditions. According to this hypothesis, we observed that the back pressure for unfilled and filled materials were strikingly different. This is in accordance with the theory proposed by Gilmer et. al. [49] that suggests, materials with high modulii transitioning to a very low viscosity fluid upon heating experience backflow. The back pressure sustained by bronze filaments was seen to be distinctly lower than that of PLA and TPU.
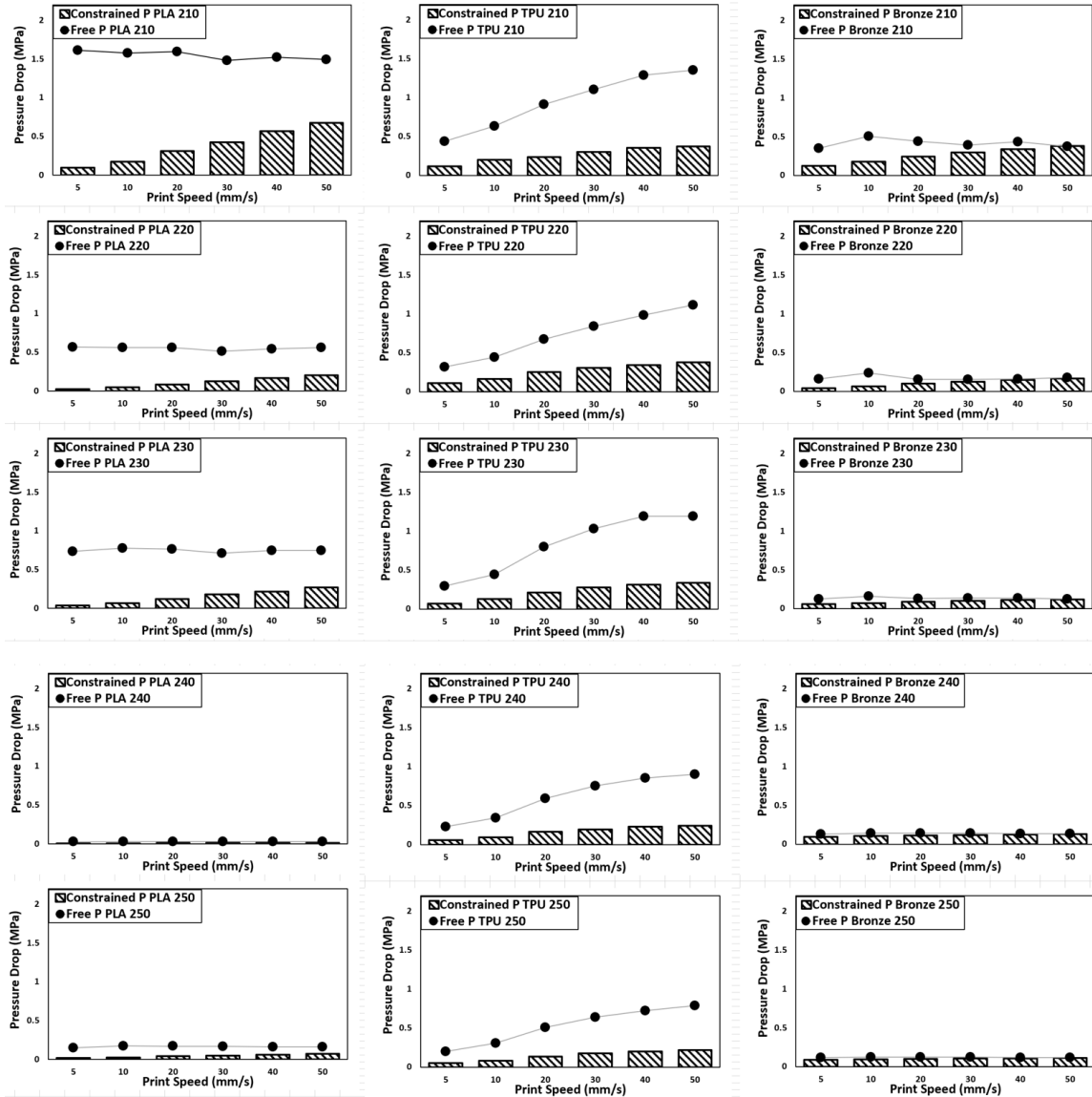
Figure 4.6 : *Pressure drop across the nozzle for TPU, PLA and Bronze as a function of print speed at different print temperatures considering both free and constrained flow conditions*

In **Figure 4.7**, the force required to overcome the pressure drop was calculated by taking into consideration, only pressures measured during free and constrained flow conditions. With the importance of back-pressure being evident from **Figure 4.5** and **Figure 4.6**, it makes sense to study and compare the forces calculated assuming constrained flow conditions.

63
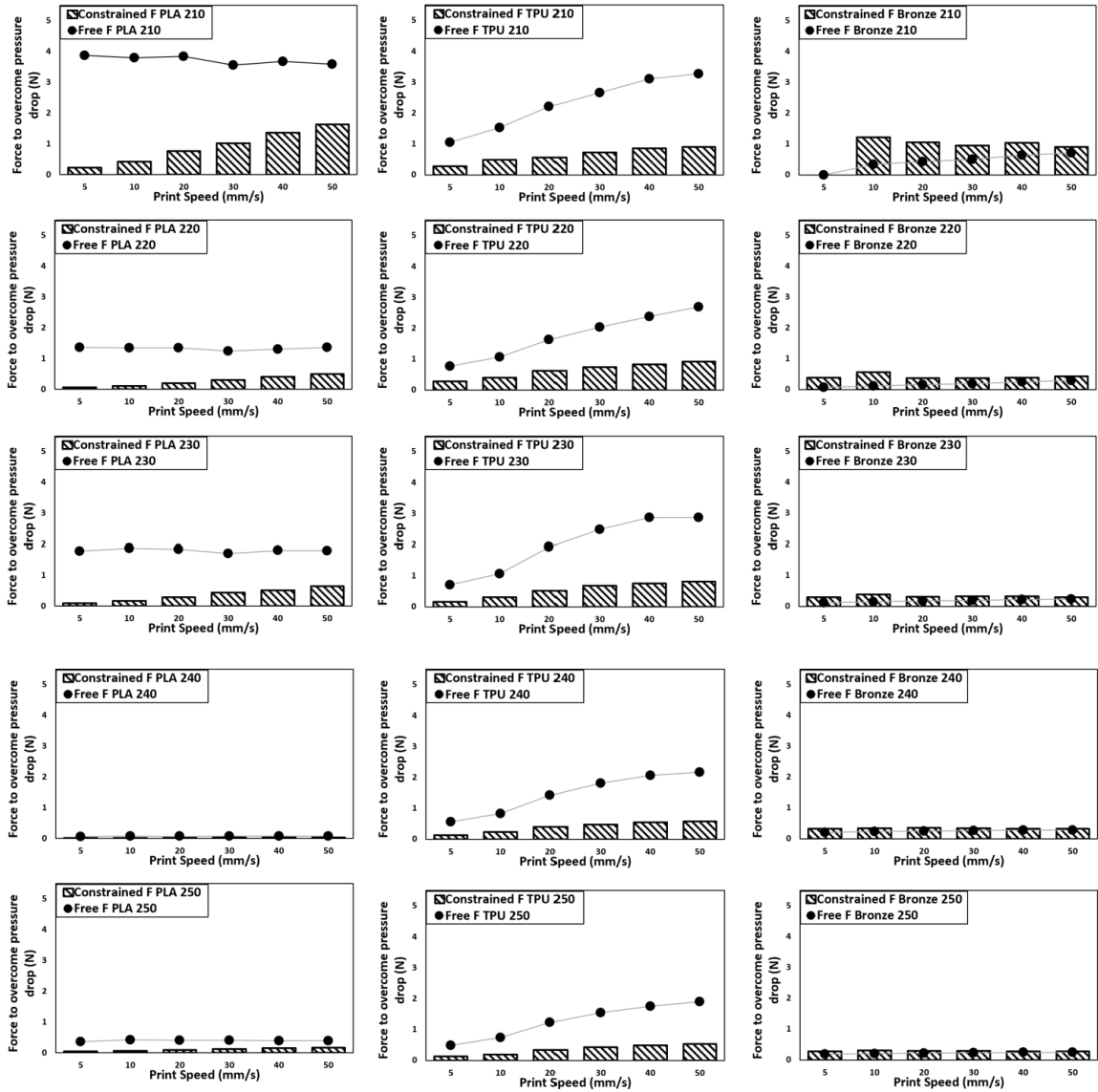
Figure 4.7 : *Force required to overcome the pressure dop across the nozzle for TPU,*
PLA and Bronze as a function of print speed at different print temperatures

The relatively higher force values for PLA and Bronze filaments at lower temperature (210°C) was indicative of the higher viscosity values of these feedstocks at lower temperature. TPU filaments on the other hand were seen to be more sensitive to print speed, experiencing higher forces with increasing print speeds. This was attributed to the lower stiffness of TPU compared to PLA and bronze-filled filaments. It was suspected that the low stiffness of TPU combined with higher feed rates facilitated bucking of the filament

between the rollers and the liquefier, thereby reducing the volumetric flow rate across the nozzle, leading to higher force requirement to overcome the pressure drop.

4.4.4 Weight-Ratio and Viscosity Mapping

To understand the printability of each material at different processing conditions, simple cubes were 3D printed with each material (PLA, TPU and Bronze) and screened for their weight-ratio (WR) at different extrusion temperatures and print speeds. **Figure 4.8** represents the weight-ratio of cubes printed at different conditions. A 5% tolerance limit was considered and all the print conditions that yielded parts with a weight-ratio <95% or higher than 105% were classified as non-optimal prints. Although the force required to overcome the pressure drop for every material used was lower than maximum load a filament can sustain under compression, parts printed using only certain print speeds and temperatures displayed optimal weight-ratio with a 5% tolerance.
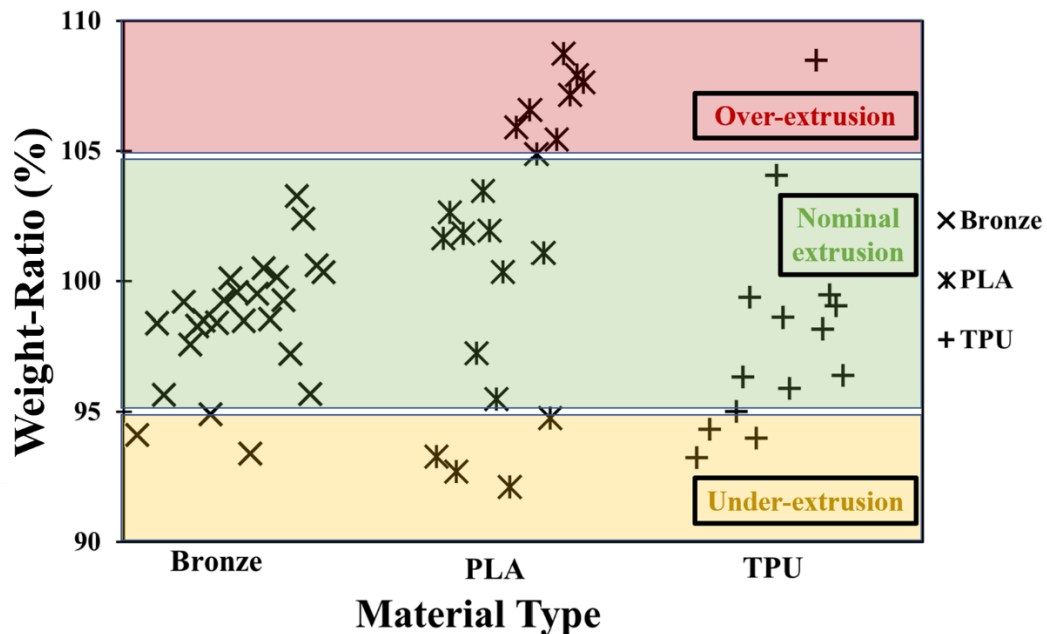
Figure 4.8 : *Weight-ratio mapping of parts printed using filaments of TPU, PLA, and Bronze*

This emphasizes the fact that the filament structural stability, although a determining condition in 3D printing, is not the only parameter to predict printability of a material at given processing conditions. Moreover, the trend in achieving optimum prints was also seen to be varying with each material, suggesting that the printability of a material under specific process conditions is as much dependent on the thermal and rheological characteristics of the molten material in the liquefier as it is on the stiffness and strength of the filament.

The viscosity of all threes material systems (PLA, TPU and Bronze) was measured at each combination of print temperature and print speed. These viscosity values at different print conditions were correlated to the weight-ratio at their respective print conditions and classified accordingly. Parts printed at weight-ratio less than 95% were considered "under-extrusion" and parts with weight-ratio higher than 105% were classified as "over-extrusion", with all the parts having weight-ratio greater than 95% and less than 105% being "nominal extrusion". **Figure 4.9** represents all the viscosity data from different material systems printed at multiple print parameter combinations, classified based on their weight-ratio. Most of the under-extruded parts printed with WR<95% were seen to have higher viscosity, while over extruded parts (WR>105%) seemed to exhibit relatively lower viscosity. It is also worth noting that the number of correlations between viscosity and weight-ratio for bronze is most distinct, with PLA tending to over-extrude and TPU tending to under-extrude. This behavior to attributed to material characteristics such as stiffness & strength of PLA over TPU and Bronze filaments. Moreover, it was also observed that the viscosity range for these three material systems vary with TPU extruding nominally at a higher viscosity range compared to PLA and Bronze filaments.
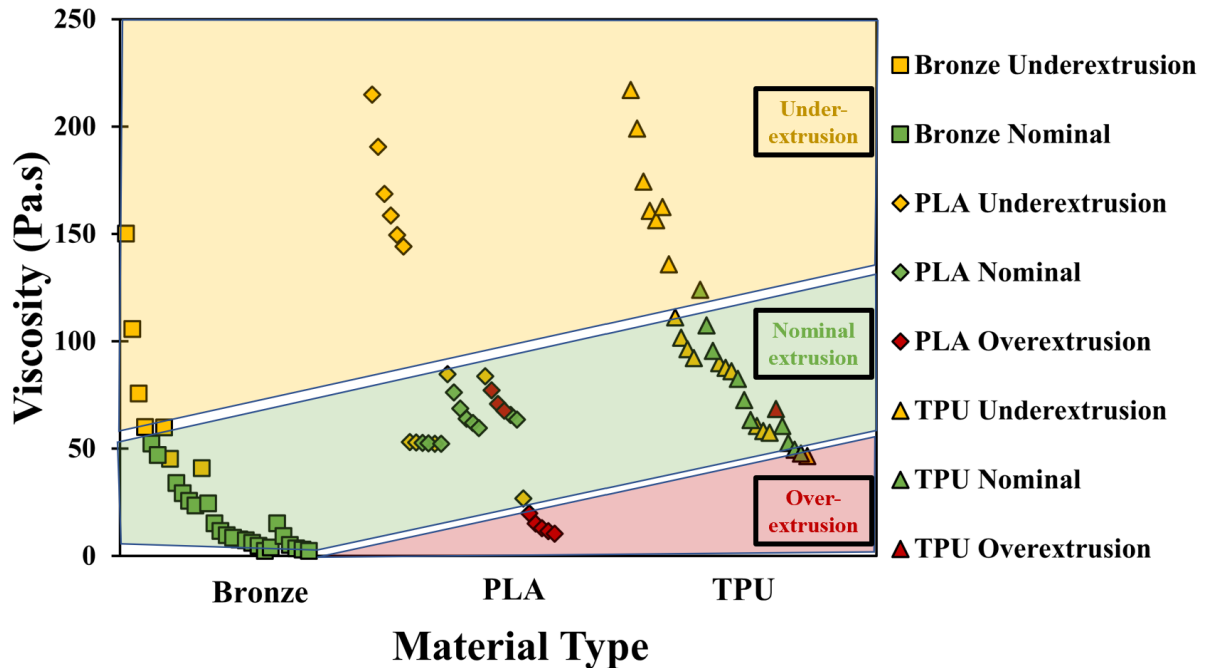
Figure 4.9: *Viscosity data of PLA, TPU, and Bronze classified according to Weight-Ratio (WR). WR<95% represents "under-extrusion", WR>105% represents "over-extrusion", and 95%<WR<105% represents nominal extrusion*

4.5 Statistical Modelling

Metal MEX 3D printing is a multi-step technique involving feedstock fabrication, filament extrusion, 3D printing, and post processing to get to the final part. Every step in this process involves multiple process parameters which can define the quality and properties of the 3D printed part. Understanding the influence and effect of each parameter by trial and error, or even by design of experiments is highly time-consuming and rigorous. To help solve this problem and to assist in predicting the viscosity which determines the material flow through the nozzle, as well as weight-ratio that identifies the green part quality, statistical modelling such as multiple variable regression and logistic regression analysis was performed.

4.5.1　　　ANOVA Analysis

The effect of the experimental conditions on the measured variables is investigated by statistical analysis approaches. **Table 4.2** shows the p-value results from N-way analysis of variance (ANOVA) [71] on the effect of the experimental conditions on the observed measurements of weight-ratio, viscosity and force across nozzle.

Table 4.2 : p-value results from ANOVA.

Measured Properties	P<0.05
Weight-Ratio	$X_1 \mid X_2 \mid X_3$
	$X_1 * X_2 \mid X_1 * X_3$
Viscosity	$X_1 \mid X_2 \mid X_3$
	$X_1 * X_2 \mid X_1 * X_3 \mid X_2 * X_3$
Force Across Nozzle	$X_1 \mid X_2 \mid X_3$
	$X_1 * X_2 \mid X_1 * X_3$

Note:

X_1 – Material (PLA | TPU | Bronze Feedstock)

X_2 – Nozzle Temperature (210 | 220 | 230 | 240 | 250 °C)

X_3 – Print Speed (5 | 10 | 20 | 30 | 40 | 50 mm/s)

The conditions are as follows: material (PLA, TPU, Bronze Feedstock), nozzle temperature (210, 220, 230, 240, 250 °C), and print speed (5, 10, 20, 30, 40, 50 mm/s). A significance levels 0.05 is used for comparison. Significant effect of all three experimental conditions is observed for the weight-ratio, viscosity, and force. However, there is difference regarding interaction effects. Viscosity exhibits significant interaction effect of

nozzle temperature and print speed. This is not observed for the weight-ratio and force across nozzle. But all three measured variables exhibit significant interaction between material and nozzle temperature, and material and print speed.

4.5.2   Multiple Variable Regression

We investigated if the constrained flow rate and the weight-ratio can be effectively predicted by applying regression modeling on the process variables. For the multiple variable regression, the input or predictor variables included three dummy variables corresponding to the three material types – Bronze, PLA, TPU. This means that the dummy variables have values of 0 or 1, with 1 corresponding to the presence of a material. The other predictor variables are Temperature and Speed. The response variables are the Constrained Flow Rate and Weight-Ratio. Using MATLAB^{TM}, the coefficient estimates for the multiple linear regression based on the response and the predictor variables. The coefficients thus obtained are shown in **Table 4.3**.

Table 4.3 : Coefficient estimates of multiple linear regression

Coefficients	Constrained Q ($X10^{-5}$ cm^3/s)	Weight-Ratio (%)
Bronze	32.9	19.0
PLA	3.8	18.8
TPU	14.6	65.0
Temperature	39.9	29.9
Speed	286.0	-6.3

It should be noted that in **Table 4.3**, there is no constant term for the regression model. There is no need for including a constant term (intercept) in this linear regression due to the presence of dummy variables. **Figure 4.10** shows the plots of the experimental and fitted "Constrained Q" and "Weight-Ratio (%)". The correlation is good and suggests

that linear regression is effective in predicting these outcomes and can be utilized to develop a prediction model with division of experimental data into training and testing data sets.
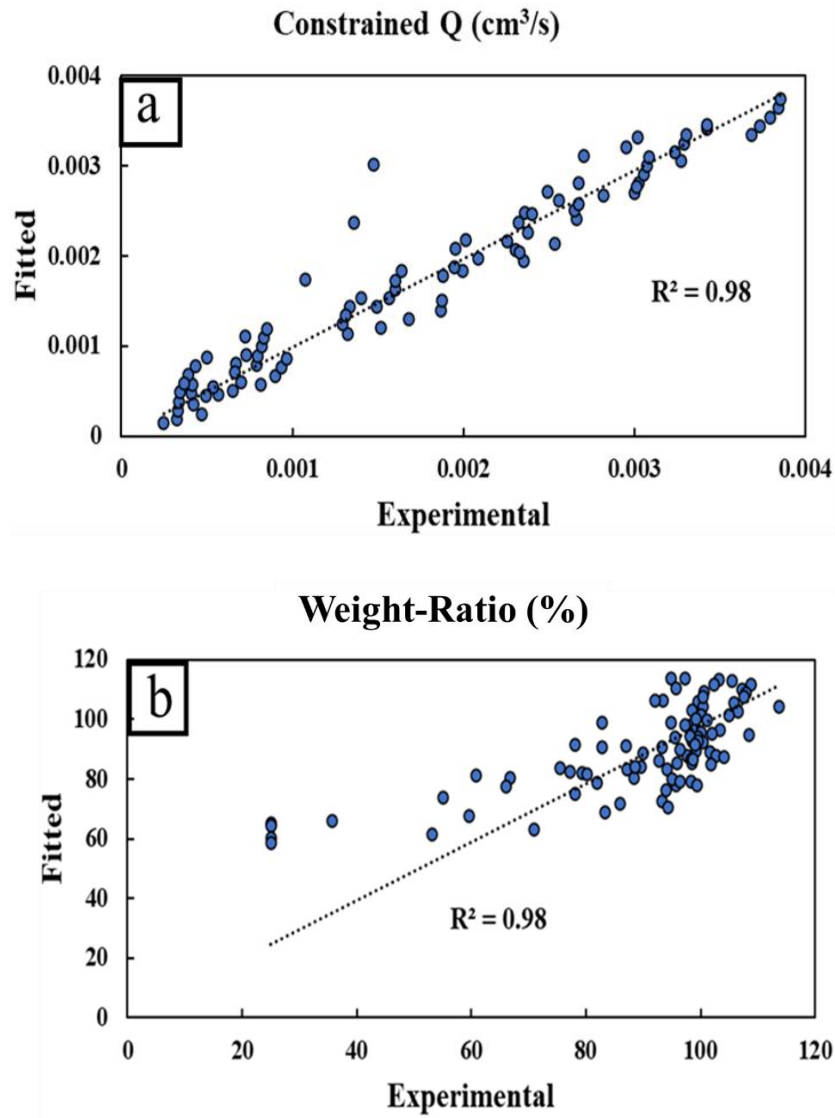
Figure 4.10 : Plots of fitted and experimental (a) constrained Q, and (b) density values from multiple variable regression.

4.5.3   Logistic Regression

In the context of 3D printing, the weight-ratio has also been explored as a categorical variable with three states – under extrusion, normal extrusion, and over

extrusion. Thus, a prediction of the extrusion category based on the process conditions may also be a helpful tool. A multinomial logistic regression model was developed. The predictor variables were the same as in the multiple linear regression in **Section 4.5.2**. The response variable was the categorical variable of extrusion state. In this study, the outcomes were not equally divided among under extrusion, normal extrusion and over extrusion. Consequently, the effectiveness of logistic fit is affected. In the future, for an effective logistic regression-based prediction of the extrusion, the experiments will incorporate large datasets as well as equal number of data points pertaining to the three categories of extrusion. Our experiments described in this study resulted in 39 instances of under extrusion, 9 instances of over extrusion, and 42 instances of normal extrusion. Regardless, the effectiveness of logistic regression was explored as an initial proof of concept. Using MATLAB^{TM} to fit the multinomial logistic regression, the relative risk equations are obtained as shown in **Eq. 4.8** and **Eq. 4.9**.

$\ln\left(\frac{P_{Under\ Extrusion}}{P_{Over\ Extrusion}}\right) = -15.57 - 16.80(Bronze) - 17.92(PLA) - 19.21(TPU) +$

$4.26(Temperature) + 1.34(Speed)$ …………………………………….. (Eq. 4.8)

……………………………………... (Eq. 4.9)

The regression models (**Eq. 4.8** and **Eq. 4.9**) were used to calculate and the probabilities and compared with actual test conditions. In the case of over extrusion, the fitted probability of over extrusion is higher than the probability of normal extrusion in 8 out of 9 instances. Similarly, in the case of under extrusion, the fitted probability of under extrusion is higher than the probability of normal extrusion in 37 out of 39 instances. However, although these fits are not perfect and cannot confidently be used to predict if the extrusion is normal or abnormal due to the size of the dataset, they still give insight on

the probability of over-extrusion or under-extrusion of a given material system under given parameters. Our future study will utilize logistic regression as well as other predictive models based on larger datasets to predict the extrusion in 3D printing.

4.6 Conclusion

Material Extrusion (MEX) 3D Printing, especially with unfilled hard, soft, and highly filled (metal/ceramic) polymer systems, effectively fabricates polymers, composites, and even metals and ceramic components. However, MEX 3D Printing requires tremendous efforts toward optimizing the parameters to achieve highly dense parts when there is a change in material type and composition. Parameter optimization is a trial-and-error process requiring rigorous experimentation and testing. This process step makes MEX 3D Printing time-consuming and overwhelming to work with new material systems regularly. Therefore, it is advantageous to predict the material properties such as viscosity to achieve parts with nominal weight-ratio irrespective of changes in the material type, composition, and print parameters such as nozzle temperature and print speed.

Specifically, this work identified that MEX 3D Printing with hard, soft, and highly filled polymer composites significantly depends on each material system's intrinsic material characteristics and mechanical properties. For instance, hard and stiff PLA filaments, which were 25X stronger and 8X stiffer than soft and flexible TPU, can print at higher speeds (up to 50mm/s) as compared to TPU (<20mm/s). This behavior is due to different material systems' filament strength and viscosity variation at a given nozzle temperature and print speed. The 3D printing speed also changes the force required to overcome the pressure drop across the nozzle. For example, at 230°C and 50mm/s, the viscosity of TPU is 1.5 times that of PLA, producing 55% dense TPU parts as opposed to

100% dense PLA parts. Conversely, bronze-filled filaments, although brittle and fragile, still manage to print 98% dense parts under similar print conditions. This behavior is because the force to overcome the pressure drop in bronze (0.2N) is lower than that for TPU (2.9N), making TPU buckle and causing inconsistent material flow and can be captured on a process-property map.

ANOVA analysis highlighted the significance of viscosity, and force required to overcome the pressure drop, causing each material system to either under-extrude, over-extrude, or print optimally at different print parameters. Viscosity and weight-ratio maps were developed to pinpoint the locations of high-density parts printed using various material systems processed at different print conditions. Multiple variable regression models predicted the volumetric flow rate and weight-ratio with up to 98% accuracy, and logistic regression models quantitatively identified the probability of over-extrusion or under-extrusion. In conclusion, this work helps us understand how the material-structure-process relationship governs the printing process and the ensuing part properties.

CHAPTER 5. CONCLUSIONS & FUTURE WORK

5.1 Conclusions

This dissertation presents an in-depth investigation into the challenges and advancements of 3D printing pure copper, focusing on Material Extrusion (MEX) processes. The study highlights the importance of achieving 100% density in the green stage to ensure over 93% sintered density and 98% Hot Isostatic Pressing (HIP) density. The research addresses the gap in understanding the scaling of mechanical and electrical properties from the green to the sintered state in the MEX metal 3D printing process. The study explores the difficulties of 3D printing, sintering, and Hot Isostatic Pressing (HIP) of copper parts, providing insights into the scaling of mechanical properties, the thermal performance of copper heat sinks, and the complexities of achieving full part density in 3D printed components. The study demonstrated the feasibility of processing bound powder copper feedstocks through Material Extrusion (MEX) 3D printing, followed by debinding, sintering, and HIP treatments. The research has shown that pre-sintering holds at varying temperatures in a hydrogen reduction atmosphere coupled with the HIP process can enhance the copper parts' mechanical and electrical properties. As a result, the ultimate tensile strength and Young's modulus experience substantial increases, while electrical conductivity transitioned from 86% IACS to 100% IACS. This research opens up new horizons for the future evolution of 3D printing and HIPing, offering the potential to

manufacture high-performance copper parts tailored to the exacting demands of diverse industries.

The insights gained from this section are then utilized to improve the thermal performance of bound metal MEX 3D printed copper heat sinks. This research explores the uncharted territory of lattice structures for heat sinks, investigating three types of lattice structures through experimental analysis and simulations to explore the potential advantages of lattice structure-based bound metal MEX 3D printing for fabricating high-performance copper heat sinks. This study has made significant contributions to the advancement of heat dissipation technologies by showcasing the superior thermal performance, material integrity, and customizability of 3D printed heat sinks with different lattice designs. The findings highlight the potential of 3D printed heat sinks to revolutionize heat dissipation technologies, making them a promising solution for various cooling applications in industries such as electronics, aerospace, and automotive. The research provides valuable insights into the performance, material characteristics, and thermal behavior of 3D printed heat sinks, paving the way for more effective and sustainable cooling solutions in the years to come.

Additionally, the research focuses on understanding the intricate interplay of material viscosity, mechanical properties, and printing speed in bound-powder-polymer MEX 3D printing. This study has made significant contributions to understanding the intrinsic material characteristics and mechanical properties of hard, soft, and highly filled (metal/ceramic) polymer systems in Material Extrusion (MEX) 3D printing. It explores PLA, TPU, and bronze-filled metal powder-bound filaments, investigating their impact on achieving a printed part weight-ratio (WR) of 100±5%. The research has identified that

MEX 3D printing significantly depends on each material system's intrinsic material characteristics and mechanical properties. The development of viscosity and weight-ratio maps and multiple variable regression models has helped to predict the volumetric flow rate and weight-ratio with up to 98% accuracy, enabling the efficient printing of high-density parts irrespective of changes in the material type, composition, and print parameters. This work helps us understand how the material-structure-process relationship governs the printing process and the ensuing part properties, paving the way for more efficient and predictive material design and discovery for bound metal filaments. Process maps of weight-ratio and viscosity were created for each material type, and a full factorial design of experiments was conducted to identify the effects of print conditions on various variables.

Overall, this research contributes to understanding the challenges and advancements in 3D printing, providing insights into the scaling of mechanical properties, the thermal performance of copper heat sinks, and the complexities of achieving full part density in 3D printed components. The research opens new avenues for material design, process optimization, and the practical applications of high-performance copper components across diverse industries.

5.2 Future Work

The study presented above has made significant contributions to the field of 3D printing of copper and its alloys. However, there is still room for further research and development to enhance the process's capabilities and improve the material properties of the printed parts. In this section, we outline some potential areas for future work:

1. **Material Innovations:**

    a. *Qualify New Material Systems:* There is a vast scope for exploring novel material systems, including Cu-10Sn, Ni-Ti, C18150, C14500. Research on these systems can help us understand their intrinsic material characteristics and mechanical properties in the 3D printing process.

    b. *Identify Structure-Property Correlationships:* In-depth analysis of porosity evolution with HIPing, considering factors like openness, surface/bulk distribution, size, shape, and distribution. Investigation into grain size evolution through heat treatment, emphasizing grain coarsening and orientations via Electron Backscatter Diffraction (EBSD). Examination of the effects of post-sintering heat treatments (annealing, tempering, ageing) on material properties. Exploration of the impact of chemical composition and trace elements (C.N, O, P, S analysis) on the final part properties.

2. **Process Innovations:**

    a. *Infill Patterns:* Research on infill patterns with the potential to skip solvent and thermal debinding, reducing lead times. Evaluation of infill patterns for minimizing variations in final part properties, enhancing reliability and consistency. Investigation into infill patterns to potentially decrease shrinkages by incorporating a powder-filled bulk in the infill skeleton. Leveraging 3D printing design freedom and Powder Metallurgy's high sintered densities for optimized outcomes.

    b. *Coated Filaments:* Exploration of coated filaments to enhance inter-layer bond strength in 3D printed parts. Development of techniques to make traditionally

fragile filaments, like ceramic filaments, printable. Investigation into the potential to fabricate parts with hierarchical microstructures using coated filaments.

c. ***Multi-metal 3D Printing:*** Research on the potential of 3D printing functionally graded materials for diverse applications. Development of techniques to engineer alloys and explore new-material combinations through multi-metal 3D printing. Investigation into the feasibility of printing high-entropy alloys for advanced material applications.

3. **<u>Process Monitoring & Predictability</u>:**

a. ***Identification of Acoustic and Vibration Signals:*** Develop methods to identify and interpret acoustic and vibration signals from 3D printers. Correlation of these signals with specific events such as filament clogging, filament breakage, and inconsistent prints. Implementation of real-time monitoring systems for enhanced predictability and control of the 3D printing process. This future work envisions a comprehensive exploration of materials, processes, and monitoring techniques, pushing the boundaries of 3D printing capabilities for copper and its alloys. The proposed innovations aim to not only deepen our understanding of material behavior but also enhance the reliability, efficiency, and versatility of the 3D printing process.

REFERENCES

[1]   W.A. Lanford, P.J. Ding, S. Hymes, S.P. Murarka, Surface and interface modification of copper for electronic application, Mater. Res. Soc. Symp. - Proc. 337 (1994) 169–176. https://doi.org/10.1557/proc-337-169.

[2]   R.P. Minneci, E.A. Lass, J.R. Bunn, H. Choo, C.J. Rawn, Copper-based alloys for structural high-heat-flux applications: a review of development, properties, and performance of Cu-rich Cu–Cr–Nb alloys, Int. Mater. Rev. 66 (2021) 394–425. https://doi.org/10.1080/09506608.2020.1821485.

[3]   B. Blakey-Milner, P. Gradl, G. Snedden, M. Brooks, J. Pitot, E. Lopez, M. Leary, F. Berto, A. du Plessis, Metal additive manufacturing in aerospace: A review, Mater. Des. 209 (2021) 110008. https://doi.org/10.1016/j.matdes.2021.110008.

[4]   G. Sciacca, M. Sinico, G. Cogo, D. Bigolaro, A. Pepato, J. Esposito, Experimental and numerical characterization of pure copper heat sinks produced by laser powder bed fusion, Mater. Des. 214 (2022) 110415. https://doi.org/10.1016/j.matdes.2022.110415.

[5]   A. Mezghani, A.R. Nassar, C.J. Dickman, E. Valdes, R. Alvarado, Laser powder bed fusion additive manufacturing of copper wicking structures: fabrication and capillary characterization, Rapid Prototyp. J. 27 (2021) 1181–1188. https://doi.org/10.1108/RPJ-01-2021-0016.

[6]   L. Ren, X. Zhou, Z. Song, C. Zhao, Q. Liu, J. Xue, X. Li, Process parameter optimization of extrusion-based 3D metal printing utilizing PW-LDPE-SA binder system, Materials (Basel). 10 (2017). https://doi.org/10.3390/ma10030305.

[7]   Y. Zhao, W. Gao, J. Xi, H. Li, F. Ren, Development of copper powder paste for direct printing and soft mold casting, Addit. Manuf. 31 (2020) 100992. https://doi.org/10.1016/j.addma.2019.100992.

[8]   L. Moballegh, J. Morshedian, M. Esfandeh, Copper injection molding using a thermoplastic binder based on paraffin wax, Mater. Lett. 59 (2005) 2832–2837. https://doi.org/10.1016/j.matlet.2005.04.027.

[9]   Y. Bai, C.B. Williams, An exploration of binder jetting of copper, Rapid Prototyp. J. 21 (2015) 177–185. https://doi.org/10.1108/RPJ-12-2014-0180.

[10]   A. Kumar, Y. Bai, A. Eklund, C.B. Williams, Effects of Hot Isostatic Pressing on Copper Parts Fabricated via Binder Jetting, Procedia Manuf. 10 (2017) 935–944. https://doi.org/10.1016/j.promfg.2017.07.084.

[11]   A. Yegyan Kumar, J. Wang, Y. Bai, S.T. Huxtable, C.B. Williams, Impacts of process-induced porosity on material properties of copper made by binder jetting additive manufacturing, Mater. Des. 182 (2019) 108001. https://doi.org/10.1016/j.matdes.2019.108001.

[12]   G. Singh, J.M. Missiaen, D. Bouvard, J.M. Chaix, Copper additive manufacturing using MIM feedstock: adjustment of printing, debinding, and sintering parameters for processing dense and defectless parts, Int. J. Adv. Manuf. Technol. 115 (2021) 449–462. https://doi.org/10.1007/s00170-021-07188-y.

[13]   G. Singh, J.M. Missiaen, D. Bouvard, J.M. Chaix, Copper extrusion 3D printing

using metal injection moulding feedstock: Analysis of process parameters for green density and surface roughness optimization, Addit. Manuf. 38 (2021) 101778. https://doi.org/10.1016/j.addma.2020.101778.

[14] S. Hong, C. Sanchez, H. Du, N. Kim, Fabrication of 3D Printed metal structures by use of high-viscosity cu paste and a screw extruder, J. Electron. Mater. 44 (2015) 836–841. https://doi.org/10.1007/s11664-014-3601-8.

[15] X. Yan, L. Hao, W. Xiong, D. Tang, Research on influencing factors and its optimization of metal powder injection molding without mold via an innovative 3D printing method, RSC Adv. 7 (2017) 55232–55239. https://doi.org/10.1039/c7ra11271h.

[16] J. Gonzalez-Gutierrez, S. Cano, J.V. Ecker, M. Kitzmantel, F. Arbeiter, C. Kukla, C. Holzer, Bending properties of lightweight copper specimens with different infill patterns produced by material extrusion additive manufacturing, solvent debinding and sintering, Appl. Sci. 11 (2021). https://doi.org/10.3390/app11167262.

[17] J. Rodriguez, J.I. Vicente, J.C. Ezeiza, A. Zuriarrain, P.J. Arrazola, X. Badiola, E. Dominguez, D. Soler, Mechanical and electrical properties of additively manufactured copper, IOP Conf. Ser. Mater. Sci. Eng. 1193 (2021) 012034. https://doi.org/10.1088/1757-899X/1193/1/012034.

[18] C. Santos, D. Gatões, F. Cerejo, M.T. Vieira, Influence of metallic powder characteristics on extruded feedstock performance for indirect additive manufacturing, Materials (Basel). 14 (2021). https://doi.org/10.3390/ma14237136.

[19] A. Cañadilla, A. Romero, G.P. Rodríguez, M. Caminero, Ó.J. Dura, Mechanical, electrical, and thermal characterization of pure copper parts manufactured via

material extrusion additive manufacturing, Materials (Basel). 15 (2022). https://doi.org/10.3390/ma15134644.

[20] R. Zauner, C. Binet, D.F. Heaney, J. Piemme, Variability of feedstock viscosity and its correlation with dimensional variability of green powder injection moulded components, Powder Metall. 47 (2004) 151–156. https://doi.org/10.1179/003258904225015473.

[21] J.L. Johnson, L.K. Tan, R. Bollina, P. Suri, R.M. German, Evaluation of copper powders for processing heat sinks by metal injection moulding, Powder Metall. 48 (2005) 123–128. https://doi.org/10.1179/003258905X37792.

[22] R.M. German, J.L. Johnson, Metal powder injection molding of copper and copper alloys for microelectronic heat dissipation, Int. J. Powder Metall. (Princeton, New Jersey). 43 (2007) 55–63.

[23] ASTM International, ASTM E407-07e1: Standard practice for microetching metals and alloys, Annu. B. ASTM Stand. (2007) 22. https://doi.org/10.1520/E0407-07.2.

[24] J.M. Contreras, A. Jiménez-Morales, J.M. Torralba, Experimental and theoretical methods for optimal solids loading calculation in MIM feedstocks fabricated from powders with different particle characteristics, Powder Metall. 53 (2010) 34–40. https://doi.org/10.1179/003258909X12450768327225.

[25] P. Singh, V.K. Balla, A. Gokce, S. V. Atre, K.H. Kate, Additive manufacturing of Ti-6Al-4V alloy by metal fused filament fabrication (MF3): producing parts comparable to that of metal injection molding, Prog. Addit. Manuf. (2021). https://doi.org/10.1007/s40964-021-00167-5.

[26] H. von Lintel, E. Evsiutkina, C. Haase, U. Krupp, K. Jahns, Copper alloys for

additive manufacturing: Laser powder bed fusion of CuCr1Zr by using a green qcw-laser, Eur. J. Mater. 0 (2022) 1–17. https://doi.org/10.1080/26889277.2022.2115945.

[27] F. Singer, D.C. Deisenroth, D.M. Hymas, M.M. Ohadi, Additively manufactured copper components and composite structures for thermal management applications, Proc. 16th Intersoc. Conf. Therm. Thermomechanical Phenom. Electron. Syst. ITherm 2017. (2017) 174–183. https://doi.org/10.1109/ITHERM.2017.7992469.

[28] H. Moon, D.J. McGregor, N. Miljkovic, W.P. King, Ultra-power-dense heat exchanger development through genetic algorithm design and additive manufacturing, Joule. 5 (2021) 3045–3056. https://doi.org/10.1016/j.joule.2021.08.004.

[29] R. Balzarotti, A. Bisaccia, M.C. Tripi, M. Ambrosetti, G. Groppi, E. Tronconi, Production and characterization of copper periodic open cellular structures made by 3D printing-replica technique , J. Adv. Manuf. Process. 2 (2020) 1–13. https://doi.org/10.1002/amp2.10068.

[30] T. Pereira, J. V. Kennedy, J. Potgieter, A comparison of traditional manufacturing vs additive manufacturing, the best method for the job, Procedia Manuf. 30 (2019) 11–18. https://doi.org/10.1016/j.promfg.2019.02.003.

[31] E. Tyflopoulos, M. Steinert, A comparative study between traditional topology optimization and lattice optimization for additive manufacturing, Mater. Des. Process. Commun. 2 (2020) 1–6. https://doi.org/10.1002/mdp2.128.

[32] D. Landi, F.C. Zefinetti, C. Spreafico, D. Regazzoni, Comparative life cycle assessment of two different manufacturing technologies: Laser additive

manufacturing and traditional technique, Procedia CIRP. 105 (2022) 700–705. https://doi.org/10.1016/j.procir.2022.02.117.

[33] C. Zhang, T. Wu, S. Xu, J. Liu, Multiscale topology optimization for solid-lattice-void solid–lattice–void hybrid structures through an ordered multi-phase interpolation, CAD Comput. Aided Des. 154 (2023) 103424. https://doi.org/10.1016/j.cad.2022.103424.

[34] A. Bacciaglia, A. Ceruti, A. Liverani, Towards large parts manufacturing in additive technologies for aerospace and automotive applications, Procedia Comput. Sci. 200 (2022) 1113–1124. https://doi.org/10.1016/j.procs.2022.01.311.

[35] J. Zhu, H. Zhou, C. Wang, L. Zhou, S. Yuan, W. Zhang, A review of topology optimization for additive manufacturing: Status and challenges, Chinese J. Aeronaut. 34 (2021) 91–110. https://doi.org/10.1016/j.cja.2020.09.020.

[36] E.C.E. Costa, J.P. Duarte, P. Bártolo, A review of additive manufacturing for ceramic production, Rapid Prototyp. J. 23 (2017) 954–963. https://doi.org/10.1108/RPJ-09-2015-0128.

[37] J.C. Wang, H. Dommati, S.J. Hsieh, Review of additive manufacturing methods for high-performance ceramic materials, Int. J. Adv. Manuf. Technol. 103 (2019) 2627–2647. https://doi.org/10.1007/s00170-019-03669-3.

[38] B.S. Lazarov, O. Sigmund, K.E. Meyer, J. Alexandersen, Experimental validation of additively manufactured optimized shapes for passive cooling, Appl. Energy. 226 (2018) 330–339. https://doi.org/10.1016/j.apenergy.2018.05.106.

[39] Jordan Yaple, Design and Additive Manufacturing of Copper Heat Sinks for Microelectronics Cooling, 2021.

[40]   J. Abel, U. Scheithauer, T. Janics, S. Hampel, S. Cano, A. Müller-Köhn, A. Günther, C. Kukla, T. Moritz, Fused filament fabrication (FFF) of metal-ceramic components, J. Vis. Exp. 2019 (2019). https://doi.org/10.3791/57693.

[41]   J. Chen, D.E. Smith, Filament rheological characterization for fused filament fabrication additive manufacturing: A low-cost approach, Addit. Manuf. 47 (2021) 102208. https://doi.org/10.1016/j.addma.2021.102208.

[42]   J. Gonzalez-Gutierrez, I. Duretek, C. Kukla, A. Poljšak, M. Bek, I. Emri, C. Holzer, Models to predict the viscosity of metal injection molding feedstock materials as function of their formulation, Metals (Basel). 6 (2016). https://doi.org/10.3390/met6060129.

[43]   C. Luo, X. Wang, K.B. Migler, J.E. Seppala, Effects of feed rates on temperature profiles and feed forces in material extrusion additive manufacturing, Addit. Manuf. 35 (2020) 101361. https://doi.org/10.1016/j.addma.2020.101361.

[44]   B.N. Turner, R. Strong, S.A. Gold, A review of melt extrusion additive manufacturing processes: I. Process design and modeling, Rapid Prototyp. J. 20 (2014) 192–204. https://doi.org/10.1108/RPJ-01-2013-0012.

[45]   B.N. Turner, S.A. Gold, A review of melt extrusion additive manufacturing processes: II. Materials, dimensional accuracy, and surface roughness, Rapid Prototyp. J. 21 (2015) 250–261. https://doi.org/10.1108/RPJ-02-2013-0017.

[46]   N. Venkataraman, S. Rangarajan, M.J. Matthewson, B. Harper, A. Safari, S.C. Danforth, G. Wu, N. Langrana, S. Guceri, A. Yardimci, Feedstock material property - Process relationships in fused deposition of ceramics (FDC), Rapid Prototyp. J. 6 (2000) 244–252. https://doi.org/10.1108/13552540010373344.

[47] A. Bellini, S. Güçeri, M. Bertoldi, Liquefier dynamics in fused deposition, J. Manuf. Sci. Eng. Trans. ASME. 126 (2004) 237–246. https://doi.org/10.1115/1.1688377.

[48] H.S. Ramanath, C.K. Chua, K.F. Leong, K.D. Shah, Melt flow behaviour of poly-ε-caprolactone in fused deposition modelling, J. Mater. Sci. Mater. Med. 19 (2008) 2541–2550. https://doi.org/10.1007/s10856-007-3203-6.

[49] E.L. Gilmer, D. Miller, C.A. Chatham, C. Zawaski, J.J. Fallon, A. Pekkanen, T.E. Long, C.B. Williams, M.J. Bortner, Model analysis of feedstock behavior in fused filament fabrication: Enabling rapid materials screening, Polymer (Guildf). 152 (2018) 51–61. https://doi.org/10.1016/j.polymer.2017.11.068.

[50] L.J.L. Duddleston, K. Woznick, C. Koch, G.M. Capote, N. Rudolph, T.A. Osswald, Extrudate mass flow rate analysis in Fused Filament Fabrication (FFF): A cursory investigation of the effects of printer parameters, Annu. Tech. Conf. - ANTEC, Conf. Proc. 2017-May (2017) 43–48.

[51] D.D. Phan, Z.R. Swain, M.E. Mackay, Rheological and heat transfer effects in fused filament fabrication, J. Rheol. (N. Y. N. Y). 62 (2018) 1097–1107. https://doi.org/10.1122/1.5022982.

[52] T.A. Osswald, J. Puentes, J. Kattinger, Fused filament fabrication melting model, Addit. Manuf. 22 (2018) 51–59. https://doi.org/10.1016/j.addma.2018.04.030.

[53] T.J. Coogan, D.O. Kazmer, In-line rheological monitoring of fused deposition modeling, J. Rheol. (N. Y. N. Y). 63 (2019) 141–155. https://doi.org/10.1122/1.5054648.

[54] D.A. Anderegg, H.A. Bryant, D.C. Ruffin, S.M. Skrip, J.J. Fallon, E.L. Gilmer, M.J. Bortner, In-situ monitoring of polymer flow temperature and pressure in extrusion

based additive manufacturing, Addit. Manuf. 26 (2019) 76–83. https://doi.org/10.1016/j.addma.2019.01.002.

[55]   P. Singh, V.K. Balla, A. Tofangchi, S. V. Atre, K.H. Kate, Printability studies of Ti-6Al-4V by metal fused filament fabrication (MF3), Int. J. Refract. Met. Hard Mater. 91 (2020). https://doi.org/10.1016/j.ijrmhm.2020.105249.

[56]   J. Gonzalez-Gutierrez, S. Cano, S. Schuschnigg, C. Kukla, J. Sapkota, C. Holzer, Additive manufacturing of metallic and ceramic components by the material extrusion of highly-filled polymers: A review and future perspectives, Materials (Basel). 11 (2018). https://doi.org/10.3390/ma11050840.

[57]   J. Go, A.J. Hart, Fast Desktop-Scale Extrusion Additive Manufacturing, Addit. Manuf. 18 (2017) 276–284. https://doi.org/10.1016/j.addma.2017.10.016.

[58]   M.F. Ashby, Overview No. 80. On the engineering properties of materials, Acta Metall. 37 (1989) 1273–1293. https://doi.org/10.1016/0001-6160(89)90158-2.

[59]   D.D. Phan, J.S. Horner, Z.R. Swain, A.N. Beris, M.E. Mackay, Computational fluid dynamics simulation of the melting process in the fused filament fabrication additive manufacturing technique, Addit. Manuf. 33 (2020) 101161. https://doi.org/10.1016/j.addma.2020.101161.

[60]   M. Moretti, A. Rossi, N. Senin, In-process simulation of the extrusion to support optimisation and real-time monitoring in fused filament fabrication, Addit. Manuf. 38 (2021) 101817. https://doi.org/10.1016/j.addma.2020.101817.

[61]   C. Aumnate, A. Pongwisuthiruchte, P. Pattananuwat, P. Potiyaraj, Fabrication of ABS/Graphene oxide composite filament for fused filament fabrication (FFF) 3D Printing, Adv. Mater. Sci. Eng. 2018 (2018). https://doi.org/10.1155/2018/2830437.

[62]   T.A. Osswald, J. Puentes, J. Kattinger, Fused filament fabrication melting model, Addit. Manuf. 22 (2018) 51–59. https://doi.org/10.1016/j.addma.2018.04.030.

[63]   J. Go, S.N. Schiffres, A.G. Stevens, A.J. Hart, Rate limits of additive manufacturing by fused filament fabrication and guidelines for high-throughput system design, Addit. Manuf. 16 (2017) 1–11. https://doi.org/10.1016/j.addma.2017.03.007.

[64]   S. Rangarajan, G. Qi, N. Venkataraman, A. Safari, S.C. Danforth, Powder processing, rheology, and mechanical properties of feedstock for fused deposition of Si3N4 ceramics, J. Am. Ceram. Soc. 83 (2000) 1663–1669. https://doi.org/10.1111/j.1151-2916.2000.tb01446.x.

[65]   NinjaTek, NinjaFlex® 3D Printing Filament: Flexible Polyurethane Material for FDM Printers, (2016) 1. https://ninjatek.com/wp-content/uploads/NinjaFlex-TDS.pdf.

[66]   BCN3D   Technical   data   sheet   PLA,   (2018)   1–3. https://ultimaker.com/download/74972/UM180821 TDS ABS RB V12.pdf.

[67]   N.R.   T.Oswald,   Polymer   rheology,   2015. https://doi.org/10.1002/app.1961.070051418.

[68]   B.P. Heller, D.E. Smith, D.A. Jack, Effects of extrudate swell and nozzle geometry on fiber orientation in Fused Filament Fabrication nozzle flow, Addit. Manuf. 12 (2016) 252–264. https://doi.org/10.1016/j.addma.2016.06.005.

[69]   P. Geng, J. Zhao, W. Wu, W. Ye, Y. Wang, S. Wang, S. Zhang, Effects of extrusion speed and printing speed on the 3D printing stability of extruded PEEK filament, J. Manuf. Process. 37 (2019) 266–273. https://doi.org/10.1016/j.jmapro.2018.11.023.

[70]   W.M. C Hopmann, Extrusion dies for plastics and rubber: design and engineering

computations, Carl Hanser Verlag GmbH Co KG. (2016).

[71] A.F. Avila, D.T.S. Morais, A multiscale investigation based on variance analysis for hand lay-up composite manufacturing, Compos. Sci. Technol. 65 (2005) 827–838. https://doi.org/10.1016/j.compscitech.2004.05.021.

[72] P. Kunchala, K. Kappagantula, 3D printing high density ceramics using binder jetting with nanoparticle densifiers, Mater. Des. 155 (2018) 443–450. https://doi.org/10.1016/j.matdes.2018.06.009.

[73] W. Du, X. Ren, C. Ma, Z. Pei, Ceramic binder jetting additive manufacturing: Particle coating for increasing powder sinterability and part strength, Mater. Lett. 234 (2019) 327–330. https://doi.org/10.1016/j.matlet.2018.09.118.

[74] M. Moghadasi, W. Du, M. Li, Z. Pei, C. Ma, Ceramic binder jetting additive manufacturing: Effects of particle size on feedstock powder and final part properties, Ceram Int 46 (2020) 16966–16972. https://doi.org/10.1016/j.ceramint.2020.03.280.

[75] S. Cano, J. Gonzalez-Gutierrez, J. Sapkota, M. Spoerk, F. Arbeiter, S. Schuschnigg, C. Holzer, C. Kukla, Additive manufacturing of zirconia parts by fused filament fabrication and solvent debinding: Selection of binder formulation, Addit. Manuf. 26 (2019) 117–128. https://doi.org/10.1016/j.addma.2019.01.001.

[76] J.A. Gonzalez, J. Mireles, Y. Lin, R.B. Wicker, Characterization of ceramic components fabricated using binder jetting additive manufacturing technology, Ceram. Int. 42 (2016) 10559–10564. https://doi.org/10.1016/j.ceramint.2016.03.079.

[77] S. Maleksaeedi, H. Eng, F.E. Wiria, T.M.H. Ha, Z. He, Property enhancement of 3D-printed alumina ceramics using vacuum infiltration, J. Mater. Process. Technol.

214 (2014) 1301–1306. https://doi.org/10.1016/j.jmatprotec.2014.01.019.

[78] D. Yao, C.M. Gomes, Y.P. Zeng, D. Jiang, J. Günster, J.G. Heinrich, Near zero shrinkage porous Al2O3 prepared via 3D-printing and reaction bonding, Mater. Lett. 147 (2015) 116–118. https://doi.org/10.1016/j.matlet.2015.02.037.

[79] G. Lee, M. Carrillo, J. McKittrick, D.G. Martin, E.A. Olevsky, Fabrication of ceramic bone scaffolds by solvent jetting 3D printing and sintering: Towards load-bearing applications, Addit. Manuf. 33 (2020) 101107. https://doi.org/10.1016/j.addma.2020.101107.

[80] M. Mariani, R. Beltrami, P. Brusa, C. Galassi, R. Ardito, N. Lecis, 3D printing of fine alumina powders by binder jetting, J. Eur. Ceram. Soc. 41 (2021) 5307–5315. https://doi.org/10.1016/j.jeurceramsoc.2021.04.006.

[81] M. Schwentenwein, J. Homa, Additive manufacturing of dense alumina ceramics, Int. J. Appl. Ceram. Technol. 12 (2015) 1–7. https://doi.org/10.1111/ijac.12319.

[82] M. Dehurtevent, L. Robberecht, J.C. Hornez, A. Thuault, E. Deveaux, P. Béhin, Stereolithography: A new method for processing dental ceramics by additive computer-aided manufacturing, Dent. Mater. 33 (2017) 477–485. https://doi.org/10.1016/j.dental.2017.01.018.

[83] L. Rueschhoff, W. Costakis, M. Michie, J. Youngblood, R. Trice, Additive Manufacturing of Dense Ceramic Parts via Direct Ink Writing of Aqueous Alumina Suspensions, Int. J. Appl. Ceram. Technol. 13 (2016) 821–830. https://doi.org/10.1111/ijac.12557.

[84] S. Mamatha, P. Biswas, P. Ramavath, D. Das, R. Johnson, 3D printing of complex shaped alumina parts, Ceram. Int. 44 (2018) 19278–19281.

https://doi.org/10.1016/j.ceramint.2018.07.153.

[85] T. Isobe, T. Tomita, Y. Kameshima, A. Nakajima, K. Okada, Preparation and properties of porous alumina ceramics with oriented cylindrical pores produced by an extrusion method, J. Eur. Ceram. Soc. 26 (2006) 957–960. https://doi.org/10.1016/j.jeurceramsoc.2004.11.015.

[86] C. Tosto, M. Bragaglia, F. Nanni, G. Recca, G. Cicala, Fused filament fabrication of alumina/polymer filaments for obtaining ceramic parts after debinding and sintering processes, Materials (Basel). 15 (2022). https://doi.org/10.3390/ma15207399.

[87] D. Nötzel, R. Eickhoff, T. Hanemann, Fused filament fabrication of small ceramic components, Materials (Basel). 11 (2018). https://doi.org/10.3390/ma11081463.

[88] M. Orlovská, Z. Chlup, Bača, M. Janek, M. Kitzmantel, Fracture and mechanical properties of lightweight alumina ceramics prepared by fused filament fabrication, J. Eur. Ceram. Soc. 40 (2020) 4837–4843. https://doi.org/10.1016/j.jeurceramsoc.2020.02.026.

[89] V. Truxová, J. Šafka, J. Sobotka, J. Macháček, M. Ackermann, Alumina manufactured by fused filament fabrication: a comprehensive study of mechanical properties and porosity, polymers (Basel). 14 (2022) 1–13. https://doi.org/10.3390/polym14050991.

[90] D. Nötzel, T. Hanemann, New feedstock system for fused filament fabrication of sintered alumina parts, Materials (Basel). 13 (2020) 1–12. https://doi.org/10.3390/ma13194461.

[91] L. Gorjan, C. Galusca, M. Sami, T. Sebastian, F. Clemens, Effect of stearic acid on

rheological properties and printability of ethylene vinyl acetate based feedstocks for fused filament fabrication of alumina, Addit. Manuf. 36 (2020) 101391. https://doi.org/10.1016/j.addma.2020.101391.

[92] J. Maurath, N. Willenbacher, 3D printing of open-porous cellular ceramics with high specific strength, J. Eur. Ceram. Soc. 37 (2017) 4833–4842. https://doi.org/10.1016/j.jeurceramsoc.2017.06.001.

[93] H. Li, Y. Liu, Y. Liu, Q. Zeng, K. Hu, Z. Lu, J. Liang, J. Li, Influence of debinding holding time on mechanical properties of 3D-printed alumina ceramic cores, Ceram. Int. 47 (2021) 4884–4894. https://doi.org/10.1016/j.ceramint.2020.10.061.

[94] H. Li, Y. Liu, Y. Liu, K. Hu, Z. Lu, J. Liang, Influence of sintering temperature on microstructure and mechanical properties of Al2O3 ceramic via 3D stereolithography, Acta Metall. Sin. (English Lett. 33 (2020) 204–214. https://doi.org/10.1007/s40195-019-00950-y.

[95] ASTM C914-09, Standard test method for bulk density and volume of solid refractories by wax immersion, ASTM Int. West Conshohocken, PA,. 95 (2009) 3–5.

[96] A. López-Delgado, L. Fillali, J.A. Jiménez, S. López-Andrés, Synthesis of α-alumina from a less common raw material, J. Sol-Gel Sci. Technol. 64 (2012) 162–169. https://doi.org/10.1007/s10971-012-2843-2.

[97] P. Mulpur, K. Lingam, A. Chunduri, T.M. Rattan, A.M. Rao, V. Kamisetti, Surface plasmon coupled emission studies on engineered thin film hybrids of nano α-Al 2 O 3 on silver, AIP Conf. Proc. 1576 (2014) 22–24. https://doi.org/10.1063/1.4861970.

[98] S. Barma, B. Mandal, Effects of sintering temperature and initial compaction load

on alpha-alumina membrane support quality, Ceram. Int. 40 (2014) 11299–11309. https://doi.org/10.1016/j.ceramint.2014.03.134.

[99]   D. Agarwala M, Weeren RV, Bandyopadhyay A, Safari A, P.W. S, Filament feed materials for fused deposition processing of ceramics and metals., Int. Solid Free. Fabr. Symp. (1996).

[100] S. Agarwala M, Weeren RV, Bandyopadhyay A, Whalen P, D.S. A, Fused deposition of ceramics and metals: an overview, Int. Solid Free. Fabr. Symp. (1996).

[101] Mukesh K. Agarwala, Vikram R. Jamalabad, Noshir A. Langrana, Ahmad Safari, Philip J. Whalen and, Stephen C. Danforth, Structural quality of parts processed by fused deposition, Rapid Prototyp. J. 2 (1996) 4–19.

[102] Y. Thompson, J. Gonzalez-Gutierrez, C. Kukla, P. Felfer, Fused filament fabrication, debinding and sintering as a low cost additive manufacturing method of 316L stainless steel, Addit. Manuf. 30 (2019) 100861. https://doi.org/10.1016/j.addma.2019.100861.

[103] B.A. German RM, Injection molding of metals and ceramics, Metal Powder Industries Federation, Princeton, 1997.

[104] C. Polzin, D. Günther, H. Seitz, 3D printing of porous Al2O3 and SiC ceramics, J. Ceram. Sci. Technol. 6 (2015) 141–146. https://doi.org/10.4416/JCST2015-00013.

[105] A. Ghazanfari, W. Li, M. Leu, J. Watts, G. Hilmas, Mechanical characterization of parts produced by ceramic on-demand extrusion process, Int. J. Appl. Ceram. Technol. 14 (2017) 486–494. https://doi.org/10.1111/ijac.12665.

[106] R. Hamano, T. Ikoma, Preparation of α-alumina powder and binder for 3D printer, MRS Adv. 3 (2018) 969–975. https://doi.org/10.1557/adv.2018.300.

[107] P. Singh, Q. Shaikh, V.K. Balla, S. V. Atre, K.H. Kate, Estimating powder-polymer material properties used in design for metal fused filament fabrication (DfMF3), JOM. 72 (2020) 485–495. https://doi.org/10.1007/s11837-019-03920-y.

[108] F. Song, D.L. Tang, X.L. Wang, Y.Z. Wang, Biodegradable soy protein isolate-based materials: A review, Biomacromolecules. 12 (2011) 3369–3380. https://doi.org/10.1021/bm200904x.

[109] N. Wu, Z. Demchuk, A. Voronov, G. Pourhashem, Sustainable manufacturing of polymeric materials: A techno-economic analysis of soybean oil-based acrylic monomers production, J. Clean. Prod. 286 (2021). https://doi.org/10.1016/j.jclepro.2020.124939.

APPENDICES

A. Appendix A: Impact of Alumina Powder Morphology on Feedstock and 3D Printed Part Properties in Bound Ceramic Material Extrusion (MEX) 3D Printing

A.1 Introduction

Alumina is a highly versatile material that has found a wide range of applications in various industries. Its excellent mechanical, thermal, and electrical properties make it a popular choice for 3D printing. Some of the potential applications for 3D printed alumina include electronic components, aerospace and aviation, biomedical applications, textile and ceramics industry, and mechanical and structural components. Alumina's exceptional properties indeed make it a sought-after material for 3D printing, enabling the creation of complex and high-performance components for diverse applications. Alumina's high mechanical strength and stiffness at high temperature allow it to be used in 3D printed components, especially in high-temperature and corrosive environments. Its electrical insulation, thermal conductivity, strength, hardness, and wear resistance are especially valuable in electronic, aerospace, biomedical, textile, ceramics, and mechanical industries. The ability to produce custom implants and components further adds to its appeal for specific and specialized applications. As 3D printing technology continues to advance,

alumina's potential for new and innovative uses in different sectors is likely to expand even further.

Alumina, a highly versatile material, has witnessed widespread adoption in the realm of 3D printing, with several prominent techniques such as Binder Jetting, Stereolithography (SLA), Robocasting, and bound ceramic Material Extrusion (MEX) being utilized for its additive manufacturing. However, the use of different processes has led to intriguing variations in three critical aspects: (a) powder size, (b) powder shape, and (c) sintered density, derived from the choice of starting powder material. These variations have been well-documented in numerous studies, shedding light on the diversity present in the 3D printing of alumina (Error! Reference source not found.). As depicted in **Table A.1**, a significant range of powder sizes has been employed across various 3D printing processes for alumina. While investigations have explored both spherical and irregular powders of alumina, the primary focus of these studies has been on processing alumina and achieving specific sintered densities post-sintering. However, even when similar particle sizes and shapes are utilized in the binder jetting process, the sintered density exhibits notable variations. On the other hand, SLA, robocasting, and the MEX process predominantly rely on sub-micron size powders, enabling them to achieve sintered densities exceeding 90%. Nevertheless, intriguingly, little research has delved into the impact of alumina powder shape and size on the sintered density, particularly for these three processes.

Moreover, the MEX process remains relatively unexplored in terms of how material properties scale at different stages of the 3D printing process, encompassing filament processing, 3D printing, debinding, and sintering. Thus, this study sets out to comprehend the role of alumina powder shape in the filament manufacturing, 3D printing, and sintering

processes. To this end, alumina powders with both spherical and irregular morphologies, each measuring 10 microns, have been selected as the basis for this investigation. Notably, this research exclusively concentrates on the 3D printing process, bypassing the pursuit of a particular sintering density. In addition, the paper aims to assess the microstructures of both types of powders after sintering post-3D printing. Notably, while many material parameters have been duly considered, the powder morphology of the filler particles remains relatively underexplored. This study strives to bridge this knowledge gap and sheds light on the influence of powder morphology on feedstock and filament characteristics for MEX 3D printing. Through a thorough characterization of feedstocks containing Al_2O_3 powders with spherical and irregular morphologies in terms of viscosity and printed part properties, the printability using a conventional MEX 3D printing machine has been put to the test. Anticipating considerable differences in surface area and particle shape, the fabricated feedstocks and filaments derived from spherical and irregular Al_2O_3 powder particles are expected to exhibit markedly distinct properties. Furthermore, this study validates the feasibility of employing highly coarse (10µm) Al_2O_3 powder particles in the MEX 3D printing process to fabricate reasonably dense Al_2O_3 parts.

Through this investigation, we aim to gain a comprehensive understanding of how powder morphology influences filament properties and printed part properties. The insights gleaned from this research are expected to contribute significantly to expanding the application of PIM feedstock for MEX 3D printing. Remarkably, our findings highlight the substantial impact that particle shape exerts on the properties of feedstock materials, consequently shaping their viability for successful 3D printing.

Table A.1 : *Correlation between the powder size and shape, and the resulting sintered density for 3D printing alumina*

AM Technology	Material Type	Particle size (µm)	Particle shape	Sintered Density (%Th)	Reference
Binder Jetting	Alumina Powder (with 50nm densifier suspended solution)	40	N/A	65.78	[72]
	Alumina powder (in precursor coating solution)	10	Spherical	48	[73]
	Alumina powder (in precursor coating solution)	70	Spherical	44	[73]
	Commercial TP80 powder mix	53-90	Irregular	25.32	[74]
	Commercial TP80 powder mix	90-150	Irregular	20.25	[74]
	Alumina Grinding Powder	53	Irregular	60-65	[75]
	Alumina Grinding Powder	45	Irregular	75-85	[76]
	Alumina Grinding Powder	30	Irregular	80-95	[76]
	Alumina Grinding Powder	53+45+30	Irregular	90-96	[76]
	Alumina powder	20-50	Spherical	38.4	[77]
	Alumina powder	<25	Spherical	47-55	[78]
	Micro powders coated with nano powders	15.6	Irregular	70.9	[79]
	Alumina powder	9	Spherical	75.4	[80]
SLA	Lithoz Alumina suspension	N/A	N/A	99.3	[81]
	Alumina Slurry	1.58+0.46	N/A	98.1	[82]
Robocasting	Alumina suspension	0.48	Irregular	98.2	[83]
	Pure Alumina	0.3	Irregular	98	[84]
	Alumina + carbon fiber	0.7	N/A	62	[85]
FFF	Nanoe filament (52vol.%)	<1	N/A	96-98	[86]

	Alumina Powder (50vol.%)	0.1	N/A	97.3	[87]
	Alumina Powder (50vol.%)	0.4-0.7	N/A	89	[88]
	Zetamix Filament (52vol.%)	<1	N/A	99.54	[89]
	Alumina Powder (50vol.%)	0.1	N/A	97	[90]
	Alumina Powder (50vol.%)	0.5	N/A	98.73	[91]

A.2 Methodology

A.2.1   Materials

The methods described below were employed to characterize and prepare the feedstock for the subsequent 3D printing process using the MEX (Material Extrusion) technique. Al_2O_3 ceramic powders of two different morphologies were utilized in the study. The powders were procured from Inframat Advanced Materials, Manchester, Connecticut. The median particle size of the powders was measured to be 10μm. To assess flowability and packing density, the as-received powders underwent characterization for true, apparent, and tap densities. The true density (ρ) of the powders was determined using a helium gas pycnometer (Accupyc II 1340, Micromeritics Inc., GA, USA). The pycnometer method allows for precise measurements of the true density by using helium gas displacement.

The tap density (ρ_t) of the powders was determined using a tap density volumeter (AS-100 Tap Density Tester, Aimsizer Scientific, Dandong Liaoning, China), following the ASTM B527-15 standard. This method involves subjecting the powder to a series of taps to settle the particles and obtain the tap density value. The apparent density (ρ_a) of the powders was calculated by measuring the apparent volume of the powders using a graduated cylinder and then dividing this volume by the mass of the powder. This process

allows for the determination of the apparent density, which takes into account the volume occupied by voids and interparticle spaces. The constituent phases of the alumina powders were identified through X-ray diffraction (XRD) analysis. XRD patterns were obtained using a Discovery D8 HR instrument from BRUKER AXS, Inc., USA. XRD analysis is a standard technique for identifying crystallographic phases in materials. For feedstock preparation, a proprietary binder was used. The binder composition consisted of three components: a backbone polymer (30–50wt%), an elastomer (20–30wt%), and a plasticizing phase (20–40wt%). The elastomer provided flexibility to the filament, allowing it to be spooled into coils for ease of printing and storage. Meanwhile, the plasticizing phase helped reduce feedstock viscosity and improve the overall loading of metal powder into the binder matrix.

A.2.2   Feedstock Preparation

The preparation of the feedstock for the 3D printing process involved careful consideration of solids loading to ensure a homogeneous mixture of ceramic powder and binder. Solids loading refers to the ratio of the volume of ceramic powder to the total volume, which includes both powder and binder components. The critical solids loading was defined as the threshold beyond which inhomogeneity in the feedstock, caused by powder-binder separation, becomes noticeable. To avoid such issues, the mixing torque stabilization was monitored to maintain the solids loading below the critical value. Based on the range of solids loading reported in the published literature [87,88,90–94], a solids loading of 55 vol% was chosen for the preparation of the feedstock filaments. A 500g mixture of ceramic powder and binder at 55 vol% was blended at a temperature of 180 °C,

employing a rotating speed of 50 rpm. The blending process was carried out for 45 minutes until the torque stabilized, indicating a homogenous mixture of the powder and binder.

To further assess feedstock homogeneity and determine its flow characteristics, viscosity measurements were performed at the print temperature as a function of shear rate using a capillary rheometer (Rheograph 20, GÖTTFERT Werkstof-Prüfmaschinen GmbH, Germany) equipped with a tungsten carbide die (L/D ratio of 30:1). The feedstock viscosity was measured at 260 °C for shear rates ranging from 20 to 800 s−1 to understand the shear rate dependence of the feedstock viscosity. Although a stable torque during blending indicated a homogenous powder-binder mixture, an additional verification of feedstock homogeneity was carried out by evaluating time-dependent variations in viscosity at a constant shear rate and temperature [20]. In the current study, a constant shear rate of 50 s−1 at 160 °C was employed to assess variations in feedstock viscosity and ensure uniformity in the mixture. Through the described feedstock preparation methods, the aim was to achieve a homogeneous and well-controlled feedstock with appropriate solids loading, essential for successful and consistent 3D printing using the bound ceramic Material Extrusion (MEX) 3D printing process.

A.2.3   Filament Extrusion and Bound Ceramic Material Extrusion (MEX) 3D Printing

The blended mixture of Al_2O_3 ceramic powder and the binder system, obtained from the torque rheometer, was further processed into smaller pellets using a Plastic and Rubber Chopper PRC22-N180 (Col-Int Tech, South Carolina, USA). The resulting 55 vol% Al2O3 feedstock was then extruded into filaments with a consistent diameter of 1.75±0.05 mm using a capillary die with an L/D ratio of 30mm:1.75 mm on a capillary

rheometer (Rheograph 20, GÖTTFERT Werkstof-Prüfmaschinen GmbH, Germany). The extrusion temperature was set at 135 °C, and a uniform extrusion speed of 0.1 mm/s was maintained to obtain filaments with a smooth surface finish and consistent diameter. The measured extrusion forces at the capillary entrance were approximately 2±0.2 kN and 7±0.3 kN for feedstocks containing spherical and irregular alumina, respectively.

Bars with nominal dimensions of 4 × 3 × 45 mm, were designed using the 3D modeling program Simplify3D. The 3D printing process was carried out using a Makergear M2 3D Printer (Makergear LLC., Beachwood, OH, USA) with the bound ceramic Material Extrusion (MEX) 3D printing process, based on several printing experiments conducted using the developed feedstock system. The initial 3D printing experiments revealed that an extrusion temperature of 260 °C provided optimal feedstock viscosity, enabling continuous material flow during printing. It should be noted that the viscosity of the feedstocks with spherical and irregular powder morphologies was substantially different. To ensure good adhesion of the part to the build platform, a bed temperature of 75 °C was maintained.

For the printing parameters, a layer height of 300 μm with 100% infill, a single perimeter, and 2 top and bottom solid layers were selected. These parameters were chosen to achieve close packing of the printed beads, leading to relatively dense green parts. The deposition angle of the printed beads alternated between 45° and 135°, with the solid bottom layers printed at a 0° angle, resulting in sound and dense parts. To optimize the printing process, a print speed of 10 mm/s was found to provide good infill. Additionally, an extrusion multiplier of 120% was selected to ensure consistent material flow and promote strong inter-bead and inter-layer bonding, enhancing the overall integrity of the 3D-printed components.

A.2.4   Debinding and Sintering

A two-step debinding procedure was employed to effectively remove the binder system while minimizing debinding-related defects and reducing thermal debinding time. The debinding process involved solvent dissolution and thermal dissociation of the binder components, ensuring complete removal. The 3D printed green parts were subjected to solvent debinding using n-heptane as the solvent. The debinding process took place in a hot solvent bath at a temperature of 64 °C for 8 hours. During this period, the solvent effectively dissolved the binder components, preparing the green parts for the subsequent thermal debinding step. Following solvent debinding, the samples were carefully removed from the solvent bath and dried overnight in an oven at 80 °C to eliminate any residual solvent, ensuring the complete removal of the binder. The thermal debinding profile was designed based on thermal degradation data of the feedstock, which was generated using a thermogravimetric analyzer (TGA, SDT Q600, TA Instruments, New Castle, DE, USA). Thermogravimetric analysis experiments were conducted on the 55 vol.% Al_2O_3 feedstock in a nitrogen (N_2) atmosphere, with a heating rate of 5 °C/min up to 500 °C. The samples' thermal debinding was then performed in a stable nitrogen atmosphere, utilizing a heating rate of 1 °C/min to ensure a controlled and gradual process. The thermal debinding step effectively removed any residual binder components remaining after solvent debinding. After completion of the thermal debinding process, the samples were transferred to a tube furnace for sintering. The sintering temperature was set at 1700 °C, chosen to promote the densification of the alumina powder. The sintering process lasted for 24 hours, allowing sufficient time for the sintering process to occur thoroughly. The extended hold time of 24

hours was specifically selected to accommodate the large particle size of the Al_2O_3 powders and ensure a uniform and fully dense sintered ceramic structure.

A.2.5   Physical and Microstructural characterization

The 3D printed parts were subjected to debinding and sintering processes as described in the previous sections. After sintering, the bulk density of the sintered parts was determined using the wax immersion principle, following the ASTM C914-95 standard [95]. This method involves immersing the sintered samples in molten wax and measuring the displacement of the wax to calculate the bulk density of the parts. To calculate the relative density of the sintered parts, the pycnometer density of the initial powder particles was used as a basis. After sintering, the microstructure and pore distribution of the sintered samples were analyzed. The sintered samples were first polished using SiC papers in a sequence of 120/240/400/600/800/1200 grit to achieve a smooth surface. Subsequently, the samples were further polished using 1 μm diamond slurry followed by colloidal silica slurry to obtain a fine and polished surface for observation. The cross-section of the sintered samples was observed using a Scanning Electron Microscope (TESCAN Vega3 SEM, TESCAN Inc., Brno, Czech Republic). SEM is a powerful tool for microstructural analysis, providing high-resolution images of the sample's surface and allowing the examination of the internal structure and pore distribution. SEM analysis allowed for the verification of the microstructure, and pore morphology within the sintered alumina samples. Through the described physical and microstructural characterization methods, the properties and structure of the 3D-printed alumina components were thoroughly examined and evaluated. These analyses provided essential insights into the density, microstructure, and pore distribution, validating the effectiveness of the bound

ceramic Material Extrusion (MEX) 3D printing process for fabricating sintered alumina components.

A.3 Results and Discussion

A.3.1   Powder Characteristics

Figure A.1(a) presents the XRD peaks of the as-received alumina powders with spherical and irregular morphologies. The XRD peaks correspond predominantly to the trigonal α-Al_2O_3 crystal structure, consistent with previous published work work [96–98]. The morphological differences between the two as-received alumina powders were confirmed through scanning electron microscope (SEM) images, displayed as insets in **Figure A.1(b)** and **Figure A.1(c)**. The particle size distribution of the alumina powder indicated that 50% of the particles were smaller than 10μm, based on the manufacturer's data. Both powders exhibited similar XRD patterns, suggesting that they were compositionally similar and primarily composed of α-Al_2O_3 particles. These similarities in size and composition made them ideal candidates for studying the isolated effect of powder morphology on feedstock properties and 3D printed part properties.
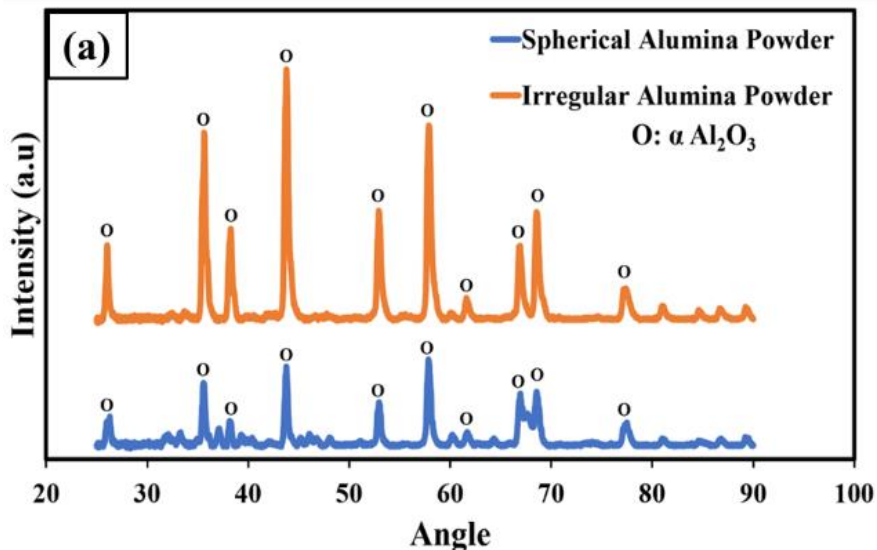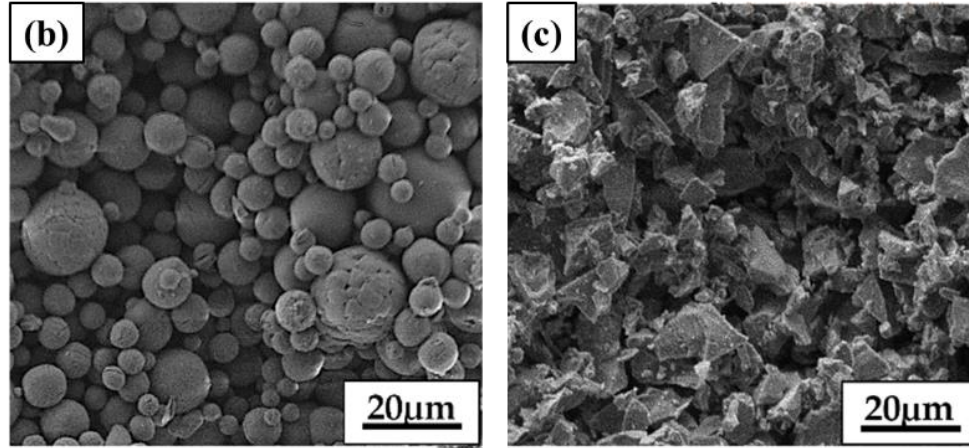
Figure A.1 : (a) XRD pattern of spherical and irregular alumina powders; (b), (c) SEM images of alumina powder particles (spherical and irregular morphologies)

Table A. summarizes the packing attributes of the Al_2O_3 powders, determined experimentally. Pycnometer density, tap density, and apparent density of both powders were measured and compared. Spherical powders are known to offer improved flowability and high packing density, which are crucial characteristics for successful bound ceramic MEX 3D printing. This observation was supported by the significantly higher apparent density and tap density values of spherical Al_2O_3 powders compared to irregular Al_2O_3 powders.

Table A.2: Pycnometer, tap, and apparent densities of alumina powders (spherical and irregular)

	Pycnometer density ρ (g/cc)	Apparent density ρ_a (g/cc)	Tap density ρ_t (g/cc)
Spherical Al_2O_3 powder	3.81 ± 0.0017	1.68 ± 0.056	2.15 ± 0.055
Irregular Al_2O_3 powder	3.92 ± 0.0014	1.19 ± 0.018	1.71 ± 0.044

A higher powder packing fraction typically enables the incorporation of a greater amount of powder into the feedstock mixture, allowing for higher solids loading and reducing overall shrinkage during sintering. The powder packing fraction is theoretically

determined by the ratio of the powder tap density (ρ_t) to the powder pycnometer density (ρ) [24]. In this study, the powder packing fraction was calculated to be 0.56 for spherical alumina powders and 0.44 for irregular alumina powders. This indicates that the packing density of spherical alumina powders is at least 20% higher than that of irregular alumina powders. Additionally, the powder flow properties were assessed and compared using the Hausner ratio (ρ_t to ρ_a). A higher value of powder flowability (lower Hausner ratio) is generally desirable, as it indicates decreased feedstock viscosity and reduced resistance to flow within the polymer binder matrix during 3D printing, especially at high solids loadings [25]. The calculated Hausner ratio for spherical alumina powders was found to be 1.28, while for irregular alumina powders, it was 1.44. This suggests that irregularly shaped alumina powder particles exhibited inferior flow properties and higher viscosity compared to their spherical counterparts.

The observed differences in powder packing fraction and flow properties between the spherical and irregular alumina powders have significant implications for the MEX 3D printing process. The higher packing density and better flowability of spherical alumina powders are likely to promote smoother and more consistent filament extrusion, leading to improved feedstock behavior during 3D printing. These characteristics may contribute to the fabrication of high-quality 3D printed parts with reduced defects and enhanced mechanical properties. Understanding the influence of these powder characteristics on the feedstock behavior and printability is essential for optimizing the MEX 3D printing process for alumina-based materials and advancing their applicability in various industries.

A.3.2   Feedstock and Filament Properties

The selection of an appropriate powder loading in the feedstock is crucial for determining the rheological properties of the powder-polymer mixture. Excessive solids loading can lead to higher viscosity, resulting in inconsistent material flow during printing, print obstructions, and entrapment of air pockets in the green parts [56,64,99–102]. Conversely, very low solids loading may cause problems such as part slumping during the debinding step of the process. Furthermore, a high binder ratio in the feedstock can lead to greater shrinkage and porosity during the sintering of parts [103]. In this study, a powder solids loading of 55 vol% was selected to ensure good feedstock flowability and viscosity during the bound ceramic Material Extrusion (MEX) 3D printing process. This choice was based on the range of solids loading used in prior research [88,90,91,93,104–106]. To achieve a homogenous feedstock, precise volumes of the proprietary binder system and alumina powder particles were carefully blended together to manufacture a high powder particle loading. The homogeneity of the feedstock is crucial for consistent 3D printing, ensuring a uniform distribution of powder throughout the printed parts. Non-homogeneous feedstocks can cause powder agglomeration, leading to filament breakage during handling or printing. Additionally, filaments with inhomogeneous powder distribution regions can result in low powder areas, causing issues such as slumping, shrinkage, warpage, and porosity during thermal processing.

To ensure feedstock homogeneity, the mixture of the powder-binder system was blended until a steady mixing torque was achieved. It was observed that the mixing torque for irregular alumina powder feedstock was significantly higher than that of the spherical alumina powder feedstock after mixing for the same amount of time in a torque rheometer

(Figure A.2(a)). The homogeneity of the feedstock was further confirmed by assessing variations in viscosity at a constant shear rate and temperature. The feedstock viscosity measurements showed a small deviation of less than 2% for both spherical and irregular feedstocks **(Figure A.2(b))**, indicating that the feedstock was highly homogeneous.
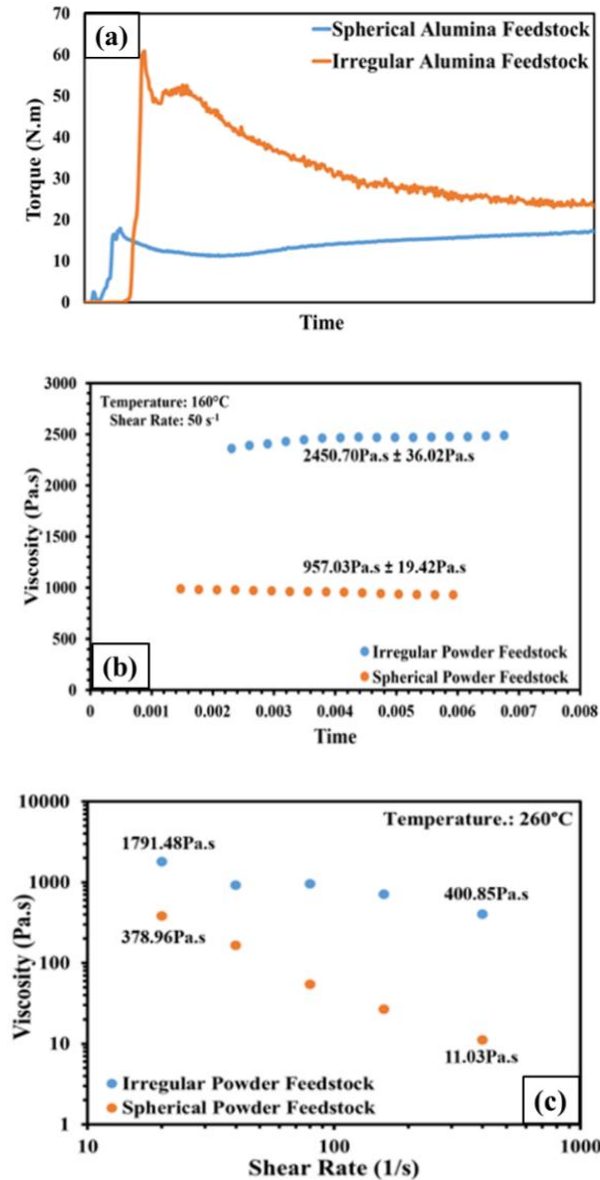
Figure A.2 : *(a) Plot showing the variation in mixing torque with time for both spherical and irregular alumina powder feedstocks (b) Time-dependent viscosity measurements for alumina feedstocks (c) shear rate- dependant viscosity measurements for alumina feedstocks*

In previous studies, it has been observed that the viscosity and pressure drop in the heated nozzle during 3D printing depend on various factors, including powder loading, binder composition, feed rate, temperature, and heat transfer gradients within the heated liquefier and nozzle sections [58,59]. To understand the rheological behavior of the material system while passing through the heated nozzle, viscosity measurements were conducted at varying shear rates, while keeping the temperature constant at 260°C. This temperature was deliberately chosen to study the changes in viscosity as the filament passes through the heated nozzle. Furthermore, Fused Filament Fabrication (FFF) systems typically operate at shear rates below 300 s^{-1} [49], depending on the feedstock material and filament feed rates. Hence, the viscosity measurement at 260°C within the shear rate range of 20 to 800 s^{-1} was deemed appropriate to accurately reflect and address the rheological behavior of the material system during 3D printing.

The viscosity of the 55 vol% Al_2O_3 feedstock was determined at 260°C in the shear rate range of 20–800 s^{-1}, with the Rabinowitsch correction applied to obtain the shear rate at the wall. As shown in **Figure A.2(c)**, the viscosity exhibited a decrease with an increase in shear rate, which is characteristic of shear-thinning behavior observed in most 3D printed materials. For the spherical alumina feedstock, the viscosity decreased from 380 Pa.s at a shear rate of 20 s^{-1} to 10 Pa.s at a shear rate of 800 s^{-1}. Similarly, the irregular alumina feedstock showed a decrease in viscosity from 3500 Pa.s at a shear rate of 20 s^{-1} to 400 Pa.s at a shear rate of 800 s^{-1}. This distinct difference in viscosity changes with respect to shear rate between the feedstocks prepared from powders with different morphologies highlights their unique rheological behavior.

SEM imaging was conducted to analyze the extruded ceramic powder-filled filaments for defects and inconsistencies along the cross-section and outer surface. The results revealed that the powder was homogeneously dispersed within the polymer matrix without any noticeable presence of voids (**Figure A.3(a)** and **Figure A.3(c)**). The cross-section of the filament was consistently circular with a diameter of $\emptyset$ 1.75 ± 0.05 mm, and none of the filament batches exhibited ovality or deformation in shape. At higher magnification, an excellent powder-polymer interface with numerous adhesion/contact points on the powder particles was observed (**Figure A.3(b)** and **Figure A.3(d)**). This robust powder-polymer interface is expected to provide sufficient mechanical strength to the filaments and promote uniform material flow during 3D printing. The filaments were also found to be reasonably flexible and easily woundable, facilitating smooth feeding into a desktop 3D printer. Overall, the analysis of feedstock and filament properties demonstrates the suitability of the selected powder-binder system for the bound ceramic Material Extrusion (MEX) 3D printing process. The homogeneity of the feedstock, along with the robust powder-polymer interface in the filaments, contributes to the consistent and defect-free fabrication of 3D printed alumina components. These findings further validate the potential of the MEX 3D printing process in producing high-quality alumina parts for various applications in industries such as electronics, aerospace, and biomedical fields.
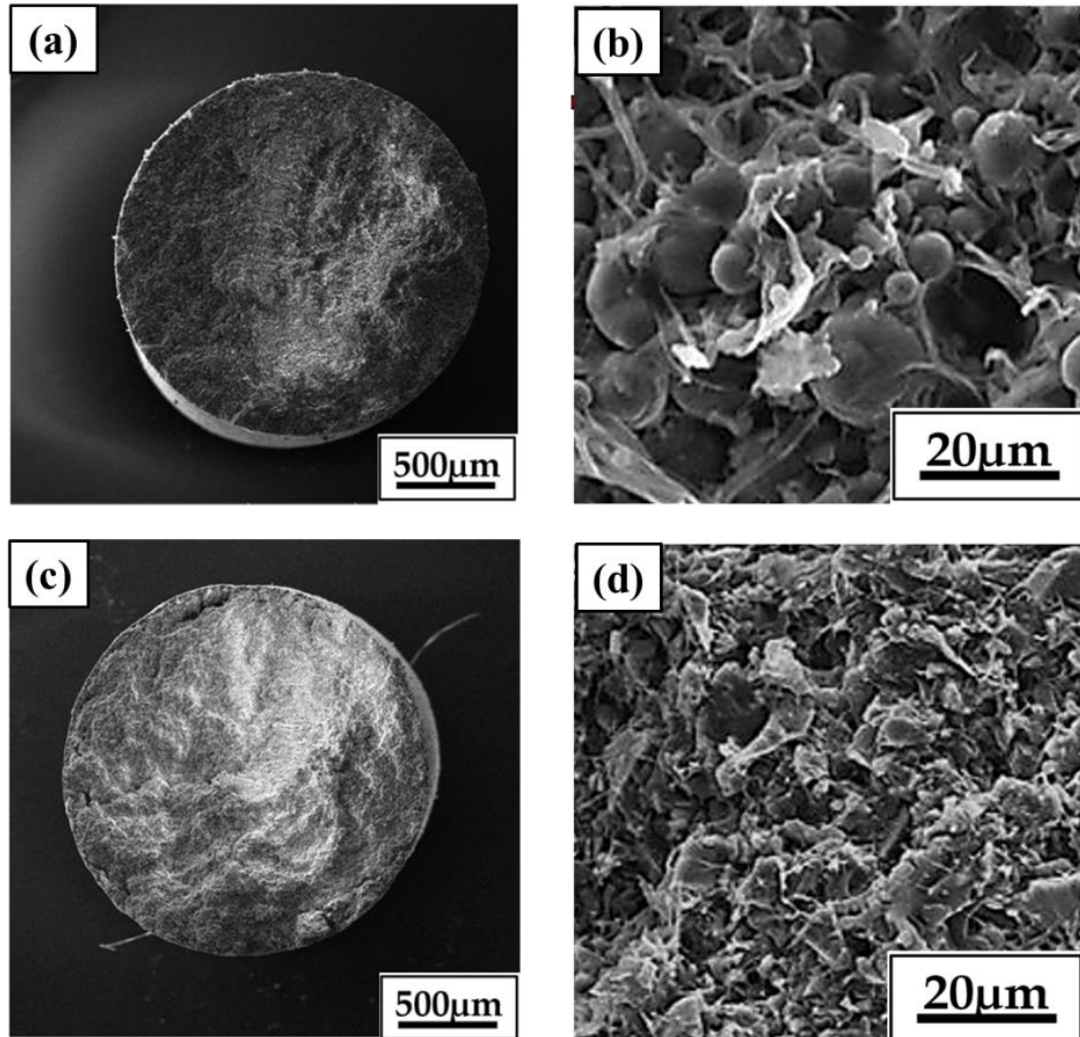
Figure A.3 : *(a),(c) Cross-section of spherical and irregular Al₂O₃ powder filaments respectively; (b), (d)Magnified SEM images of spherical and irregular powder particles held together by polymeric binder system*

A.3.3   Bound Ceramic MEX 3D Printing

Bound Ceramic Material Extrusion (MEX) 3D printing, while similar to Fused Filament Fabrication (FFF) in some aspects, presents unique challenges due to the high-volume fractions of powder particles in the feedstock. The presence of these particles affects the rheological and mechanical characteristics of the filament, making the printing process more complex. One significant observation during the MEX 3D printing process

was that there exists a critical feed rate where the extrusion force exceeds the shear strength of the filament at the roller feeding mechanism, leading to filament failure at the entrance [55]. To overcome this issue, a slow printing speed of 10 mm/s was adopted to ensure low feed rates, allowing for a consistent and continuous flow of material across the nozzle. This careful adjustment of the printing speed played a crucial role in successfully 3D printing using alumina-filled polymeric filaments. The printed parts were then subjected to analysis to evaluate their dimensions and compare them to the actual CAD part dimensions. The goal was to understand any expansion or contraction that might have occurred in the parts after printing. **Figure A.4(a)** and **Figure A.4(b)** depict the 3D printed alumina parts obtained through the MEX 3D printing process.
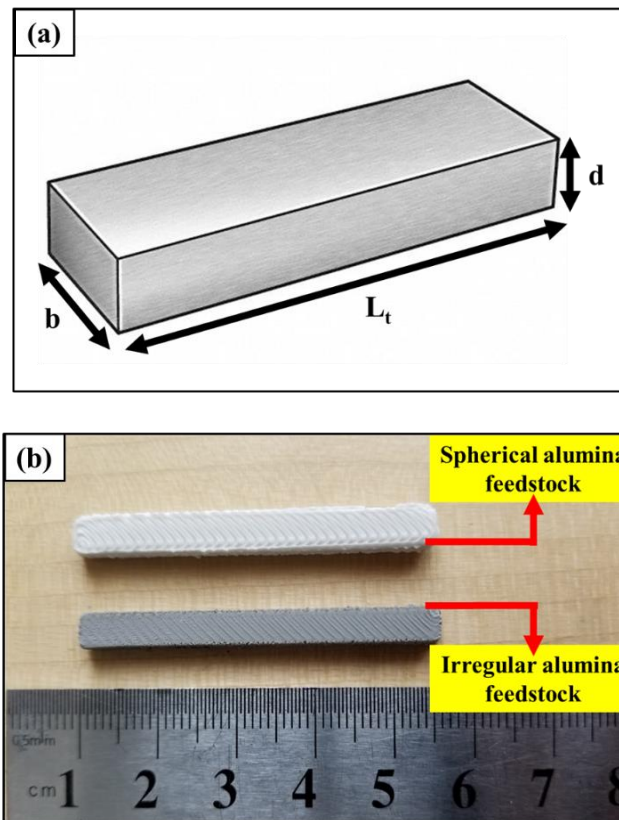
Figure A.4 : *(a) Schematic representation of the 3-point bend testing sample (b) Green parts 3D printed using spherical and irregular alumina filaments*

Understanding these dimensional changes is essential for optimizing the MEX 3D printing process and ensuring the production of parts with precise and accurate geometries. **Table** provides a detailed comparison between the dimensions of the printed parts and their corresponding dimensions in the CAD model. By examining the results in Table 3, any discrepancies between the printed part and the CAD part dimensions were identified. These discrepancies could arise due to factors such as material shrinkage during sintering, thermal effects during the printing process, and potential inaccuracies in the 3D printing system.

The geometric tolerances of 3D printed parts are influenced by several key factors, including the motion control of the gantry system, the selection of process parameters, and the properties of the printed material. The accuracy with which a CAD model is translated into a built part depends on the step size of the stepper motor in the gantry system. The process parameters used during printing play a crucial role in determining the final dimensions of the printed parts. In this study, the process parameters were carefully selected to maintain constant print conditions while 3D printing both spherical and irregular alumina powder filaments. The nozzle diameter, nozzle temperature, print speed, and extrusion multiplier were deliberately kept constant to facilitate a direct comparison between the two types of feedstocks. **Table** presents the results of the dimensional analysis for the printed parts. For parts printed with spherical alumina powder filaments, the dimensional difference was positive, indicating that the parts were larger than their respective designs along all directions. Similarly, for parts printed with irregular alumina powder filaments, the difference was positive along the 'b' and 'L_t' directions. The percentage deviation from the CAD part dimensions along the 'L_t' direction was the same

114

for both spherical and irregular powder filaments, suggesting that this deviation was solely dependent on the tolerances of the motion-controlled gantry system.

The die swelling phenomenon, caused by the lateral flow of material coming through the nozzle, resulted in radial expansion of the extrudate, leading to the dimensional changes along the 'b' direction. This phenomenon is known to limit the resolution considerations of MEX 3D printed parts [45]. Additionally, as the layer thickness (300 μm) is less than the nozzle diameter (750 μm), the material is squeezed through the print nozzle over the print bed or previous layer, leading to broader deposited beads and affecting the part dimensions in the X/Y directions. Other process parameters, such as the extrusion multiplier and printing speed, also contribute to the dimensions in these directions. For parts printed with irregular-shaped alumina powder filaments, a negative dimensional change was observed along the printing direction ('d' direction). This could be attributed to thermal contraction of the printed layers upon cooling. Moreover, the higher viscosity of the irregular feedstock led to a decreased volumetric flow rate of material across the nozzle, resulting in lower dimensional deviations compared to parts printed with spherical alumina powder filaments.

Table A.3: *Bound cermic MEX 3D printed dimesions and tolerances for green Al_2O_3 parts*

Direction	CAD part dimension	Printed part dimension (spherical)	Printed part dimension (irregular)	% deviation from CAD part (spherical)	% deviation from CAD part (irregular)
b	4mm	5.33 ± 0.14mm	4.63 ± 0.06mm	33.13 ±3.57	15.71 ± 1.47
d	3mm	3.29 ± 0.03mm	2.87 ± 0.11mm	9.50 ± 1.15	-4.50 ± 3.71
L_t	45mm	45.75 ± 0.23mm	45.39 ± 0.12mm	1.67 ± 0.50	1.67 ± 0.50

Overall, the results from the Bound Ceramic MEX 3D printing process demonstrate the successful fabrication of alumina-filled polymeric filaments for both spherical and irregular alumina powders at a controlled printing speed. The dimensional analysis provides valuable insights into the dimensional changes that occur during the printing process and helps in refining the printing parameters for achieving desired part dimensions. This knowledge contributes to enhancing the reliability and reproducibility of the MEX 3D printing process for alumina-based components. It is important to note that the material composition and thermo-physical properties, such as viscosity, specific volume, thermal conductivity, and specific heat, play a significant role in determining the final geometry of the printed parts [25]. Understanding these material properties and their relation to the process parameters is crucial for improving dimensional control and avoiding defects during the 3D printing process. By gaining a deeper understanding of these relationships, further advancements in dimensional accuracy and overall printing quality can be achieved [107].

A.3.4   Debinding and Sintering

After conducting preliminary experiments with various time-temperature combinations, the optimal conditions for solvent debinding were determined to be 64 °C for 4 hours in n-heptane solution, which removed approximately 40% of the total binder. The remaining binder was subsequently removed through thermal debinding, using a temperature profile derived from Thermogravimetric Analysis (TGA) data. **Figure A.5(a)** illustrates the TGA of the present feedstock, revealing the breakdown of the polymer binder in three distinct stages, denoted by zones 1-3. The temperature at which the maximum binder removal occurs is indicated by the peaks in the weight loss rate. For the debinding

116

process, debinding temperatures were selected from the midpoint of each decomposition zone of the TGA data, resulting in temperatures of 250 °C, 330 °C, and 440 °C. **Figure A.5(b)** depicts the combined debinding-sintering cycle employed for the alumina feedstocks. The debinding process involved two hold times, with 4 hours and 3 hours respectively, in the initial two zones. Each of these phases eliminated 20 wt% of the remaining binder after solvent debinding, leaving 60 wt% of the binder to be removed at 440 °C during a hold time of 6 hours.
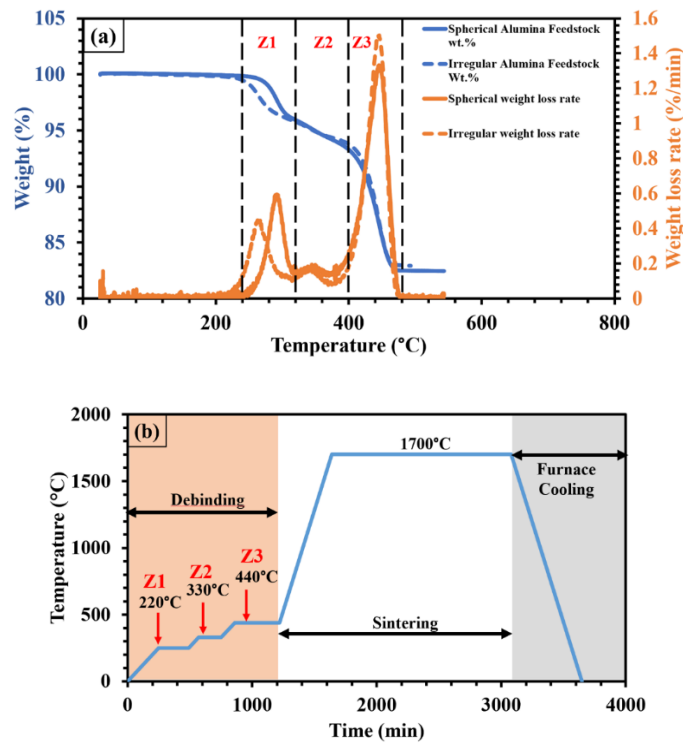
Figure A.5 : *(a) Thermogravimetric analysis of Al_2O_3 feedstocks to understand polymer decomposition kinetics (b) debinding and sintering profile for Al_2O_3 parts printed via bound ceramic MEX 3D Printing*

Complete removal of the binder is a crucial step in the entire process to ensure the desired final properties of the 3D printed parts. Following debinding, the parts underwent sintering in a tube furnace at a temperature of 1700 °C for 24 hours, in an air atmosphere at atmospheric pressure. The sintering environment was not controlled, as the material

system was chemically inert and stable, and the sintering process was conducted successfully without the need for specific atmospheric adjustments.

A.3.5   Microstructure and characterization

After debinding and sintering, four Al_2O_3 printed parts produced by bound ceramic MEX 3D printing were successfully transformed into dense final products. The sintered parts' cross-sections were polished and analyzed using Scanning Electron Microscopy (SEM), as illustrated in **Figure A.6(a)** and **Figure A.6(b)**. Notably, no printing-induced defects were observed in the microstructure, indicating the high quality of the bound ceramic MEX 3D printing process. Furthermore, the densification of the sintered parts appeared to be homogeneous across the entire cross-section. This homogeneity can be attributed to the uniform and homogeneous mixture of feedstock and filaments used during the bound ceramic MEX 3D printing process. The absence of any significant defects or inhomogeneities in the microstructure is a promising result, as it suggests that the chosen process parameters and the material composition were well-suited for achieving consistent and quality sintered parts. The SEM images provided valuable insights into the microstructural characteristics of the sintered parts, confirming their dense and defect-free nature.

The bulk densities of the sintered parts were accurately determined using the wax immersion technique, following ASTM standards, and were measured on four different samples to account for uncertainties and variations. Table 4 presents the post-sintering part properties obtained from these measurements. Under the current processing conditions, we achieved a bulk density of 3.55 ± 0.05 g/cm^3 for parts produced using spherical Al_2O_3

powder particles and 3.53 ± 0.08 g/cm^3 for parts produced using irregularly shaped Al$_2$O$_3$ powder particles.
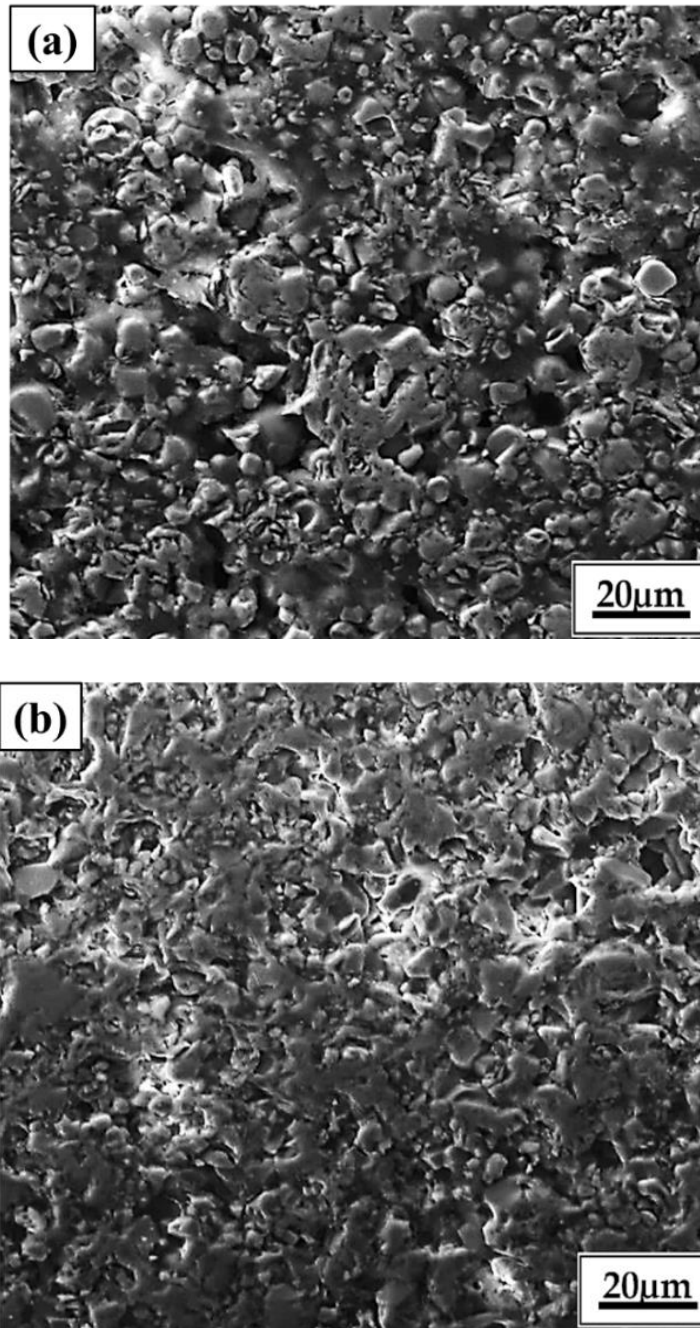
Figure A.6 : *Sintered microstructure of parts printed using (a) spherical alumina filament (b) irregular alumina filament*

Relative density measurements were also conducted to assess the level of densification achieved during the sintering process. The relative density was determined to be $93.10 \pm 1.25\%$ for parts produced using spherical Al_2O_3 powder particles and $89.82 \pm 1.93\%$ for parts produced using irregularly shaped Al_2O_3 powder particles. These results indicate that the sintered parts are highly dense, with relative densities above 89% for both types of powder morphology. While achieving these promising results, our future focus will be on fabricating even denser and mechanically stronger 3D printed parts. One potential approach is the use of smaller powder particles, which could lead to enhanced packing and densification during sintering. Additionally, the incorporation of suitable additives may assist in achieving even higher sintered densities if necessary. These advancements will further expand the capabilities and applications of bound ceramic MEX 3D printing in the production of high-quality ceramic components.

A.4 *Conclusions*

This study successfully demonstrated the bound ceramic MEX 3D printing technique for fabricating complex-shaped ceramic parts using Al_2O_3 powders of spherical and irregular morphologies. The XRD analysis confirmed that both powders primarily consisted of α-Al_2O_3 particles, making them suitable candidates for studying the isolated effect of powder morphology on feedstock properties and 3D printed part properties. The comparison of powder packing attributes revealed that spherical Al_2O_3 powders exhibited higher apparent density and tap density, indicating better flowability and packing density compared to irregular Al_2O_3 powders. This higher packing density of spherical powders allowed for greater incorporation of powder into the feedstock, reducing overall shrinkage during sintering. The feedstock preparation involved careful blending to achieve

homogeneity, ensuring uniform distribution of powder throughout the printed parts. The robust powder-polymer interface observed in the filaments contributed to smooth and consistent filament extrusion, vital for successful 3D printing. The dimensional analysis of the 3D printed parts highlighted the influence of powder morphology on the part properties. Parts printed with spherical powder filaments displayed higher positive deviations from CAD dimensions due to their lower viscosity values relative to irregular powder filaments. The debinding and sintering process resulted in dense final products without any noticeable defects or inhomogeneities in the microstructure. The achieved bulk densities and relative densities indicated highly dense sintered parts for both types of powder morphology.

Overall, the bound ceramic MEX 3D printing process showed great promise in producing high-quality alumina parts with controlled dimensional accuracy. The study sheds light on the importance of powder particle morphology and its impact on feedstock behavior, printability, and final part properties. Understanding these relationships will enable further optimization of the MEX 3D printing process, expanding its applicability in various industries such as electronics, aerospace, and biomedical fields. Future work will focus on achieving even denser and mechanically stronger 3D printed parts through the use of smaller powder particles and suitable additives, enhancing the overall capabilities and potential applications of bound ceramic MEX 3D printing.

B. Appendix B: Sinter-Based Materials Extrusion (MEX) 3D Printing of WC-Co 3D Cermet

This study attempts to identify the viability of fabricating highly-loaded tungsten carbide – cobalt (WC-Co) powder feedstocks and filaments for MEX 3D printing and sintering. The WC-Co powder samples received from Global Tungsten & Powders,

Towanda (GTP), PA, USA were characterized under a scanning electron microscope (SEM) to identify the size, shape, and morphology of these powders (**Figure B.1(a)(b)**). SEM images show the WC-Co powders to me mostly spherical in nature with an average powder particle size of 150 μm, which is in accordance with the specifications provided by the manufacturer. X-ray diffraction (XRD) was also performed on the as-received WC-Co powders to identify and validate the chemical composition of these powders (**Figure B.1(c)**).
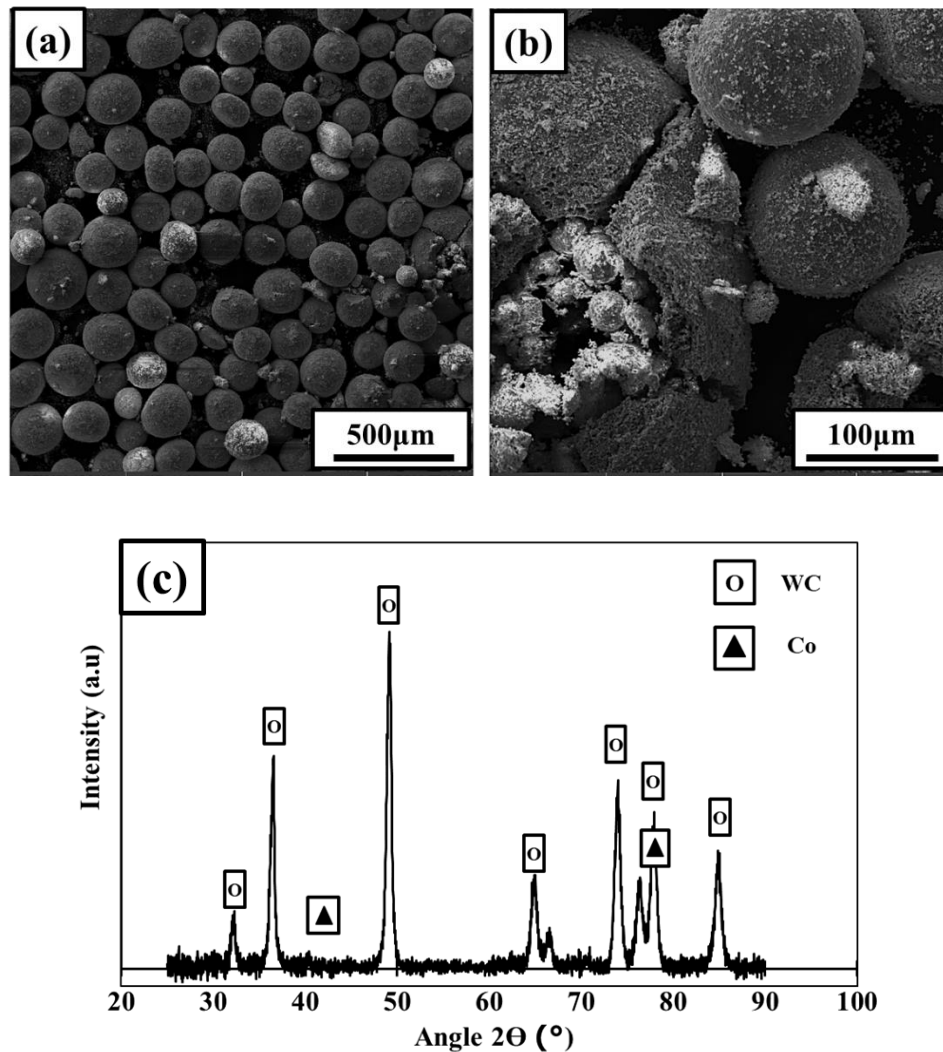
Figure B.1: *(a, (b). SEM images of as-received WC-Co powders at 150X and 800X respectively (c) XRD spectra of as-received WC-Co powders*

To understand the physical properties of these powders, helium gas pycnometry, tap density, and apparent density measurements were performed. As shown in Table B.1, the pycnometer density (true density) of these powders was found to be 11.06 g/cc whereas the apparent and tap densities were found to be 3.72 g/cc and 3.99 g/cc respectively.

The pycnometer density of the powder was measured to be 11.06 g/cm3, and two feedstock batches were mixed. The first batch was measured at 25 vol% (79 weight %) of the WC-Co powder and the second batch was mixed at 50 vol% (92 weight %). The ratio of tap density to pycnometer density was seen to be about 36%. This ratio provided insights on the ability of these powder particles to pack closely (packing fraction) after tapping. Although a critical solids loading measurement was necessary to quantitatively identify the maximum amount of powder loading that is feasible in a given feedstock while ensuring homogeneity, this ratio of packing fraction would provide qualitative information on the maximum powder loading in a feedstock.

Table B.1: *Pycnometer density, tap density, apparent density, packing fraction, and Hausners' ratio of as-received WC-Co powders*

	WC-Co Powder
Pycnometer Density (PD)	11.06 g/cc
Tap Density (TD)	3.99 g/cc
Measured Apparent Density (AD)	3.72 g/cc
Packing Fraction (TD/PD)	36.08 %
Hausner Ratio (TD/AD)	1.07

Additionally, Hausner ratio was calculated as a ratio of tap density to apparent density. Hausner's ratio is a qualitative measure of the powder flowability, where a value less than 1.2 typically suggests that the powder has acceptable flowability for powder-based AM applications. For the initial studies, feedstocks and filaments of two solids loading (25vol.% and 50vol.%) were prepared. **Figure B.2 (a)** shows the mixing torque observed while preparing these feedstocks (25vol.% and 5vol.%) as a function of time, where the torque experience by the equipment to mix the 50vol.% feedstock was clearly higher than that for the 25vol.% feedstock.
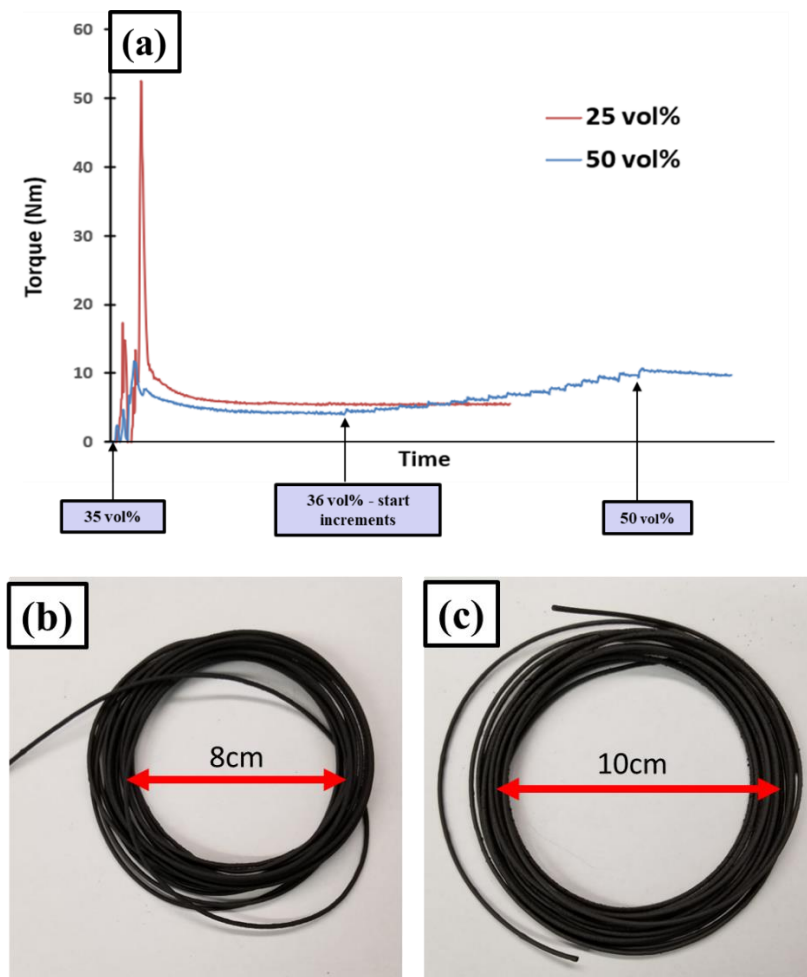
Figure B.2: *(a) Torque vs. time plot of 25vol.% WC-Co feedstock and 50vol.% WC-Co feedstock prepared in the lab (b) and (c) show bending radius of 25vol.% and 50vol.% filaments of WC-Co extruded using a capillary rheometer*

124

Filaments of both solids loadings (25vol.% and 50vol.%) were extruded using a capillary rheometer as shown in **Figure B.2 (b)(c)**. However, only the 25vol.% filaments were capable of being successfully 3D printed into green parts and density cubes, while the 50vol.% filaments were seen to be very fragile, unable to sustain the forces exerted by the drive gears of the 3D printer. Finally, a time-dependent viscosity measurement was performed on the 50vol.% WC-Co feedstock to validate the homogeneity of the feedstock (**Figure B.3**). A variation in viscosity of less than 0.5% affirmed that the feedstock is homogeneous, although the filaments were too fragile to be processed by a 3D printer.
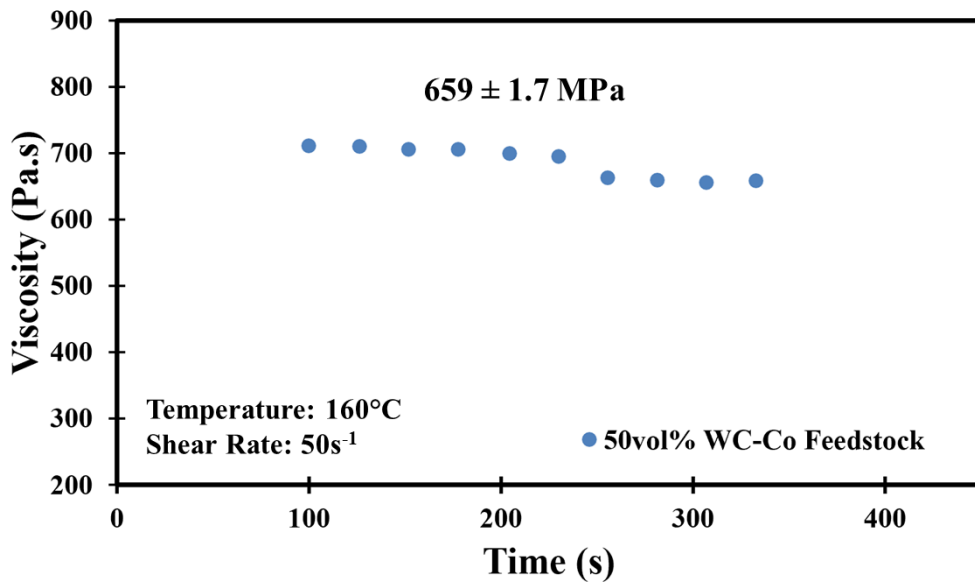
Figure B.3: Time dependent viscosity measurement of 50vol.% WC-Co feedstock depicting a variation of less than 0.5%, indicating a homogenous feedstock mixture

With these initial results, it is crucial to identify the sintering conditions and parameters required to achieve high density in pure WC-Co samples. This will provide us with baseline data on the sintered properties to expect from 3D printed and sintered parts. Additionally, parts printed using the 25vol.% WC-Co filaments could be subjected to similar sintering conditions to identify the ability to fabricate pure WC-Co 3D printed parts

using MEX technology. Finally, it is imperative that we identify the maximum optimal solids loading that can be processed into a feedstock and 3D printable filament to achieve highly dense final parts for commercial applications.

C. Appendix C: Sinter-Based Materials Extrusion (MEX) 3D Printing Of Ni-Ti Alloy

In this study, Ni-Ti powders were qualified for filament-based MEX 3D printing and sintering. The Ni-Ti powders used for this research were obtained from Dr. Sayed Ehsan Saghaian to understand the powder characteristics and their suitability to be 3D printed using this sinter-based technology.
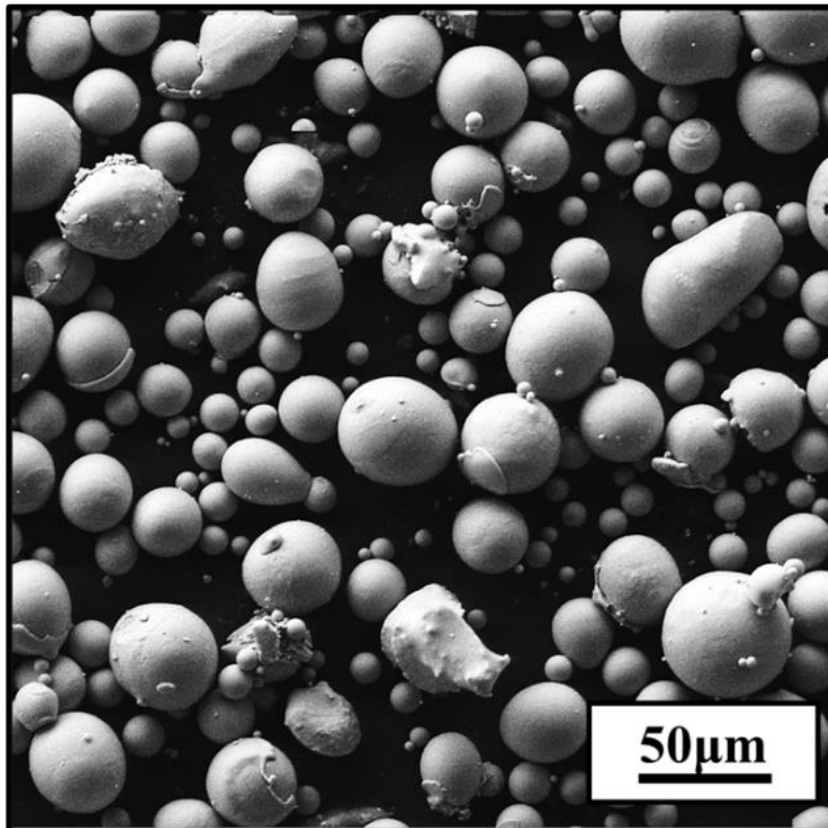
Figure C.1: *SEM image of as-received Ni-Ti powders*

Table C.1: *Particle size distribution of as-received Ni-Ti powders as specified by the manufacturer*

Ni-Ti Powder	Size (μm)
D10	16.1
D50	30.6
D90	52

The powder particle size distribution and chemical composition of the powders were acquired from the manufacturer as shown in **Table C.1** and **Table C.2**. SEM images of these powders (**Figure C.1**) were acquired to understand the size, shape, and morphology of the powder particles, followed by characterization for other physical properties such as pycnometer density, apparent density, and tap density (**Table C.3**).

Table C.2: *Chemical Composition of the as-received Ni-Ti powders as specified by the manufacturer*

Ni-Ti Powder	Composition (wt.%)
Ni	56.23
Ti	43.72
O	0.054
N	0.001

Table C.3: *Pycnometer density, apparent density, tap density, packing fraction, and Hausners' ratio of as-received Ni-Ti powders*

	Ni-Ti Powder
Pycnometer Density (PD)	6.52 g/cc
Tap Density (TD)	4.25 g/cc
Measured Apparent Density (AD)	3.93 g/cc
Packing Fraction (TD/PD)	65.08 %
Hausner Ratio (TD/AD)	1.08
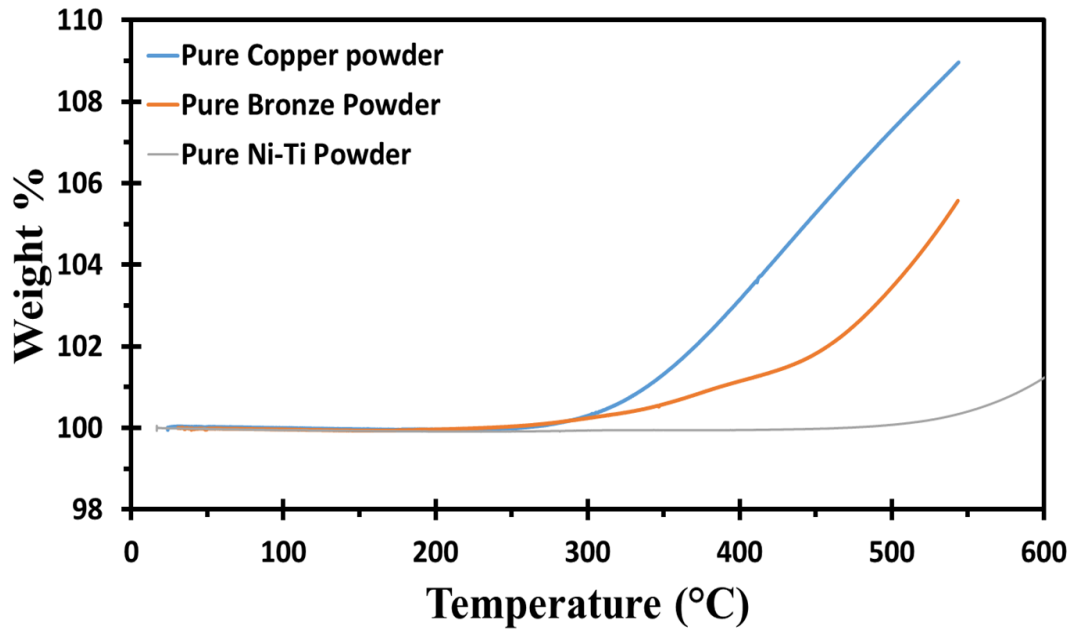
Figure C.2: *Thermogravimetric analysis of as-received Ni-Ti powders when heated in air at 5°C/min, as compared to pure copper and Cu-10Sn powders analyzed under similar conditions*
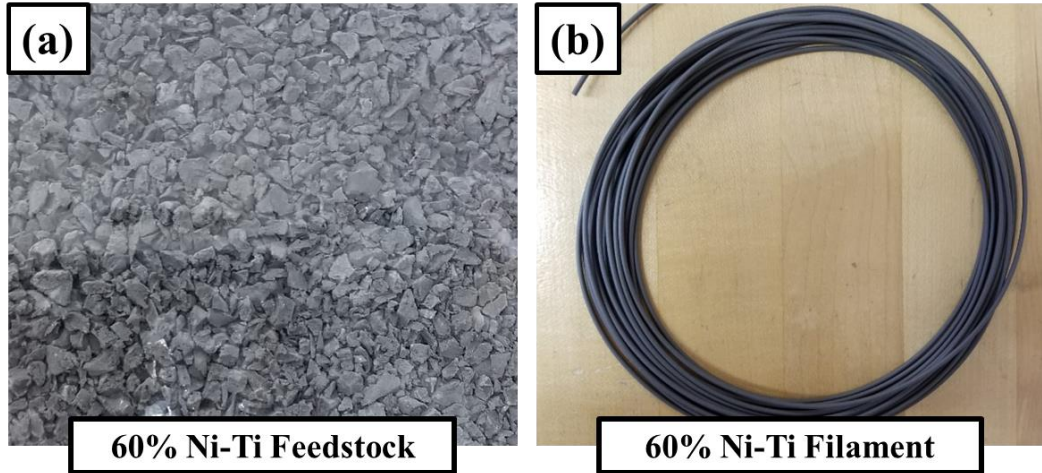
Figure C.3: *(a) 60vol.% Ni-Ti feedstock pellets (b) 60vol.% Ni-Ti filament used for 3D printing via FFF*

Additionally, these powders were subjected to thermogravimetric analysis under a constant flow of air (100m:/min) at a heating rate of 5°C/min (**Figure C.2**). These results helped identify the oxidation behavior of these powders under elevated temperatures and atmospheric pressures. This was especially important since all the processing steps (feedstock preparation, filament extrusion, and 3D printing) involve temperatures higher than room temperature, and it is essential to ensure that the powder particles do not oxidize during these steps.

Table C.4: *Pycnometer densities of 60vol.% Ni-Ti feedstock and 60vol.% Ni-Ti filaments fabricated in the lab, as compared to that of as-received Ni-Ti powders*

	Density
Ni-Ti powder	6.52 g/cc
60% Ni-Ti feedstock	4.25 g/cc
60% Ni-Ti filament	4.25 g/cc

Based on the packing fraction value for these powders (**Table C.3**) obtained as a ratio of the tap density to pycnometer density and based on past experience with preparing optimal solids loading feedstocks of pure copper powders, a solids loading of 60vol.% Ni-Ti feedstocks was prepared. These feedstocks were further extruded into a 1.75mm diameter filaments using a capillary rheometer, while constantly monitoring the extrusion force at the nozzle (**Figure C.3**). While extruding the filaments, time-dependent viscosity data was also collected and analyzed to ensure that the variation in viscosity is low, representing a homogenous feedstock. These viscosity values, as seen **Figure C.4**, are also compared to the values of a 58vol.% copper feedstock tested under similar conditions in the past. These readings provide assurance about the resistance to flow and the ability to successfully 3D print these filaments using an FDM 3D printer. Additionally, the pycnometer density of the 60vol.% powder-polymer feedstocks and filaments were measured to help calculate the relative density of the 3D printed green parts (**Table C.4**).
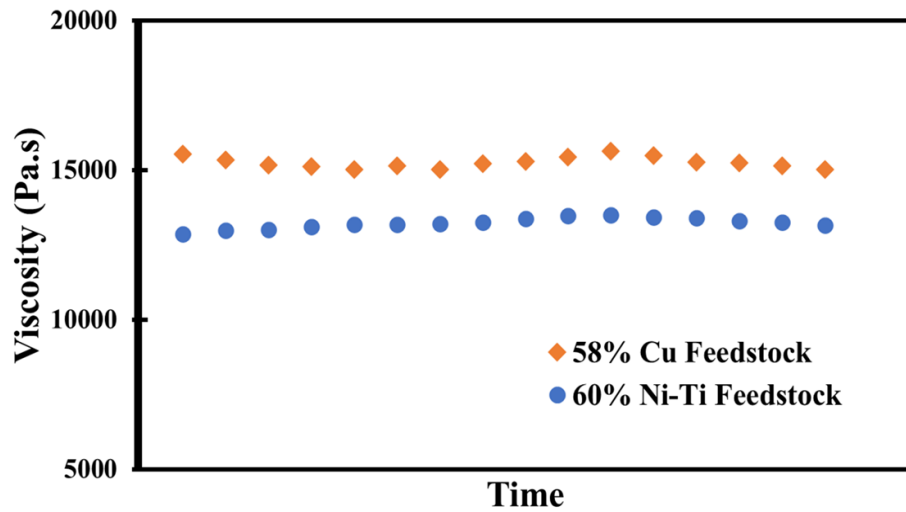
Figure C.4: *Time-dependent viscosity of 60vol.% Ni-Ti feedstock, as compared to that of 58vol.% copper feedstock (both feedstocks prepared in the lab)*

130

To summarize, this study identified the powder packing and flow characteristics of as-received powders, while validating their use for MEX 3D printing. 60vol.% feedstocks and filaments were prepared and tested for their printability on an FDM 3D printer. These 3D printed parts will now require additional debinding and sintering steps to obtain the final Ni-Ti parts. In the future, these filaments will be used to 3D print and sinter parts for mechanical testing and shape memory applications.

D. Appendix D: Sinter-Based Materials Extrusion (MEX) 3D Printing Of Cu-10Sn Alloy

In this work, a combination of Fused Filament Fabrication (FFF) and sintering were implemented, in an attempt to fabricate high density bronze (Cu-10Sn) parts via extrusion-based 3D printing technology.
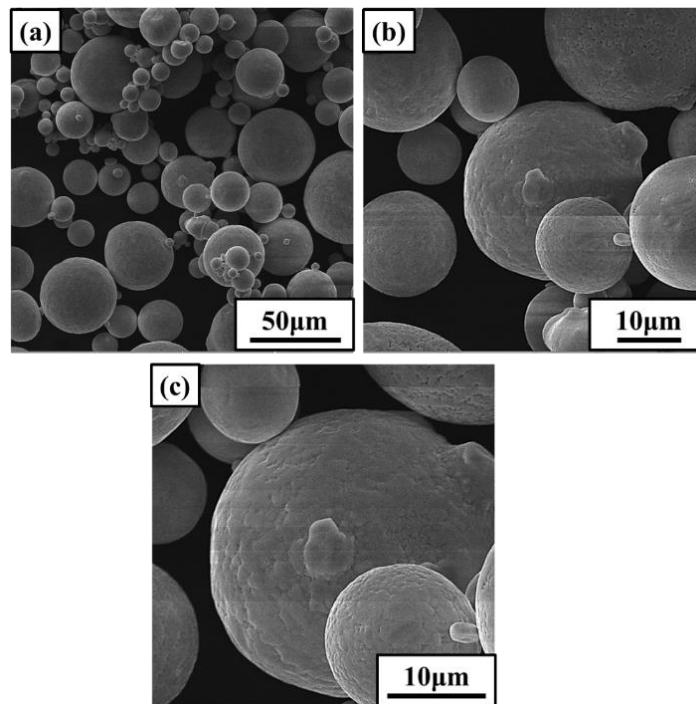
Figure D.1: *SEM images of as-received Cu-10Sn powders at (a) 1500X (b) 5000X (c) 8000X*

	Bronze Powder
Pycnometer Density (PD)	8.52 g/cc
Tap Density (TD)	5.65 g/cc
Measured Apparent Density (AD)	5.02 g/cc
Powder Packing Fraction (TD/PD)	66.25 %
Hausner Ratio (TD/AD)	1.13
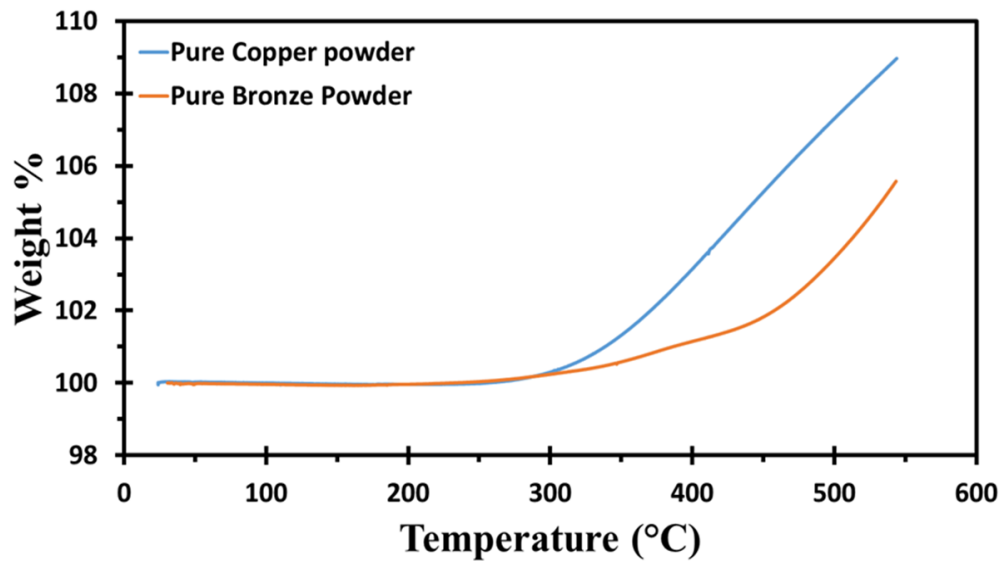
Figure D.2: *Thermogravimetric analysis of Cu-10Sn powders heated at 5°C/min under air, as compared to that of pure copper powders*

58vol.% Cu-10Sn powder-filled polymeric feedstocks and filaments were prepared and characterized for physical, thermal, and rheological properties. Subsequently, the filaments will be 3D printed and sintered to identify the optimal 3D printing and sintering

parameters to obtain highly-dense bronze parts, which in-turn will be characterized for physical and mechanical properties and compared to parts fabricated with the same material using traditional manufacturing techniques such as metal injection molding and other additive manufacturing techniques.
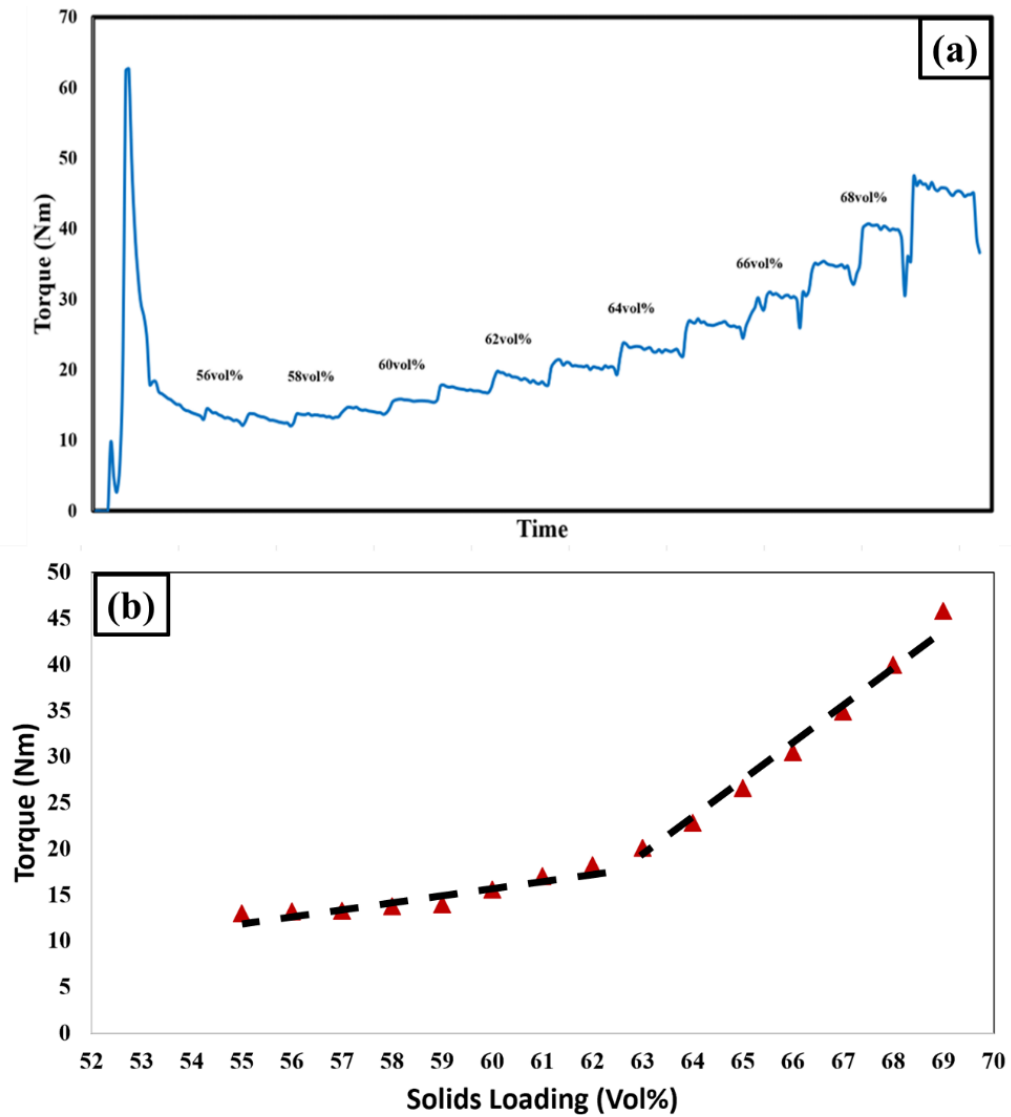
Figure D.3: *(a) Torque vs. time plot of critical solids loading measurement for Cu-10Sn feedstock with solids loading starting from 55vol.% and increasing up to 69vol.% (b) Average stable torque values plotted as a function of solids loading for Cu-10Sn feedstock to identify the optimal solids loading*
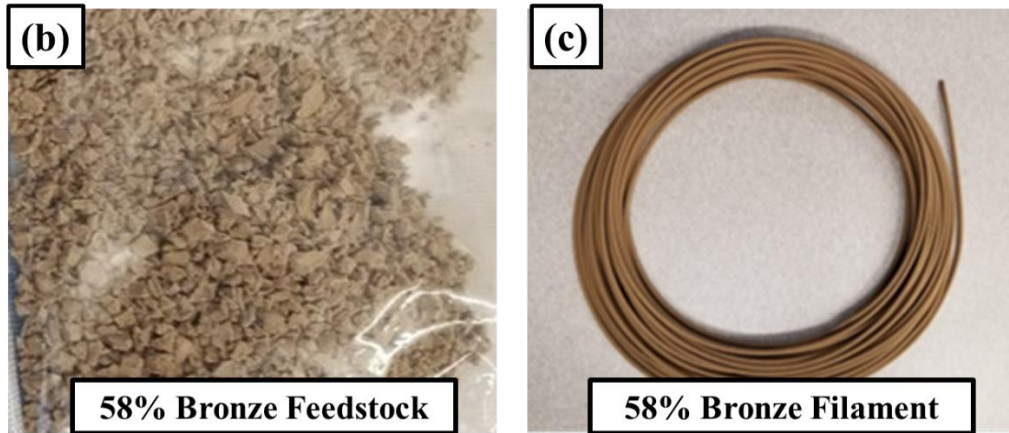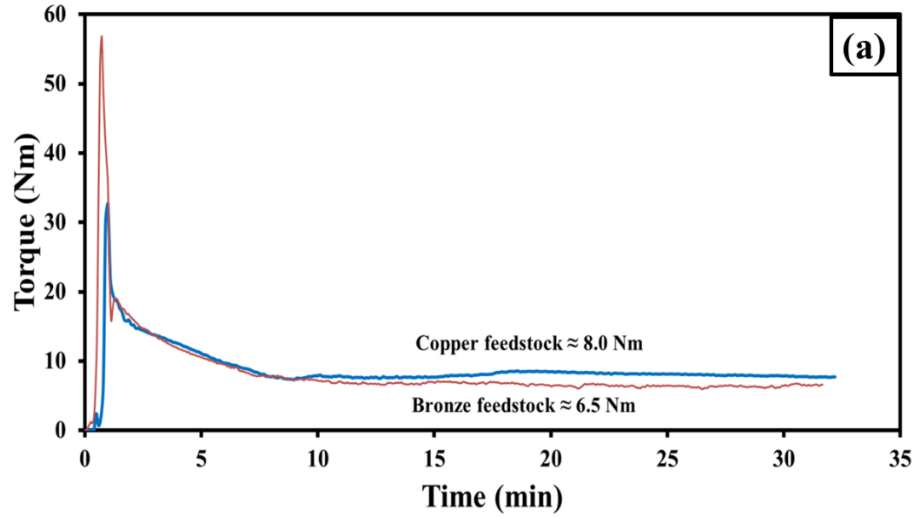
Figure D.4: *(a) Mixing torque as a function of time for 58vol.% Cu-10Sn feedstock compared to that of 58vol.% pure copper feedstock (b), (c) 58vol.% Cu-10Sn feedstock and filament respectively*
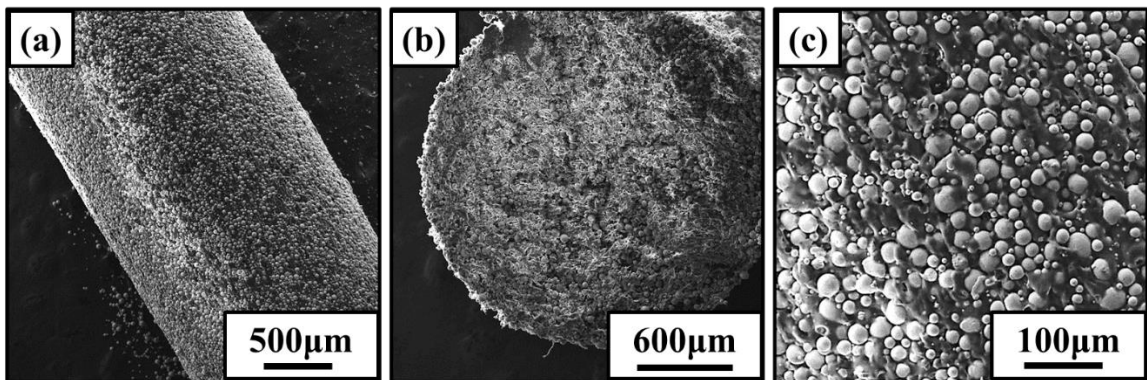
Figure D.5: *SEM images of 58vol.% Cu-10Sn filament's (a) surface (b) cross-section (low magnification) (c) cross-section (high magnification)*

134
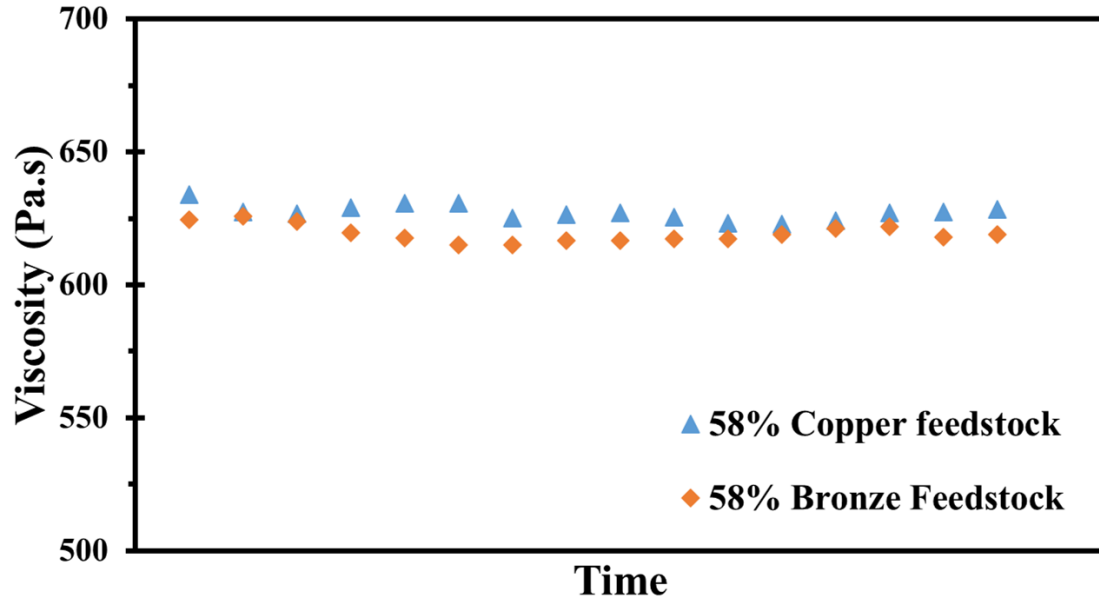
Figure D.6: *Time-dependent viscosity of 58vol.% Cu-10Sn feedstock as compared to that of 58vol.% pure copper feedstock (both prepared in the lab)*

E. Appendix E: Effect Of Thermal Debinding And Pre-Sintering Heat Treatment Holds On Lead Time And Microstructure Evolution

Material Extrusion (MEX) 3D printing using a filament is a multi-step process that is currently being tested for large-scale adoption by the metal manufacturing industries. This technology takes it's roots from the Metal Injection Molding (MIM) industry where a green part is fabricated by injection molding a highly-loaded powder-polymer feedstock, followed by debinding to remove the polymeric binder, and finally sintering to obtain the final dense metal component of desired shape and size. Although MEX 3D printing brings in the advantage of faster lead times with the ability to directly 3D print green parts without

the need for molds, it does suffer from longer post-printing heat treatment processes due to the higher polymeric binder content in the MEX feedstocks compared to MIM feedstocks.

The higher polymeric binder content, however, is necessary to ensure that the feedstock and the ensuing filament prepared from these feedstocks are flexible and processible enough to be passed through an FDM 3D printer without failing. This become a bottleneck when trying to use an industrial heat treatment furnace to debind and sinter green parts fabricated using MEX 3D printing. A good example of failed green parts when attempted to process using an industrial furnace at Kymera is seen in **Figure E.1**.
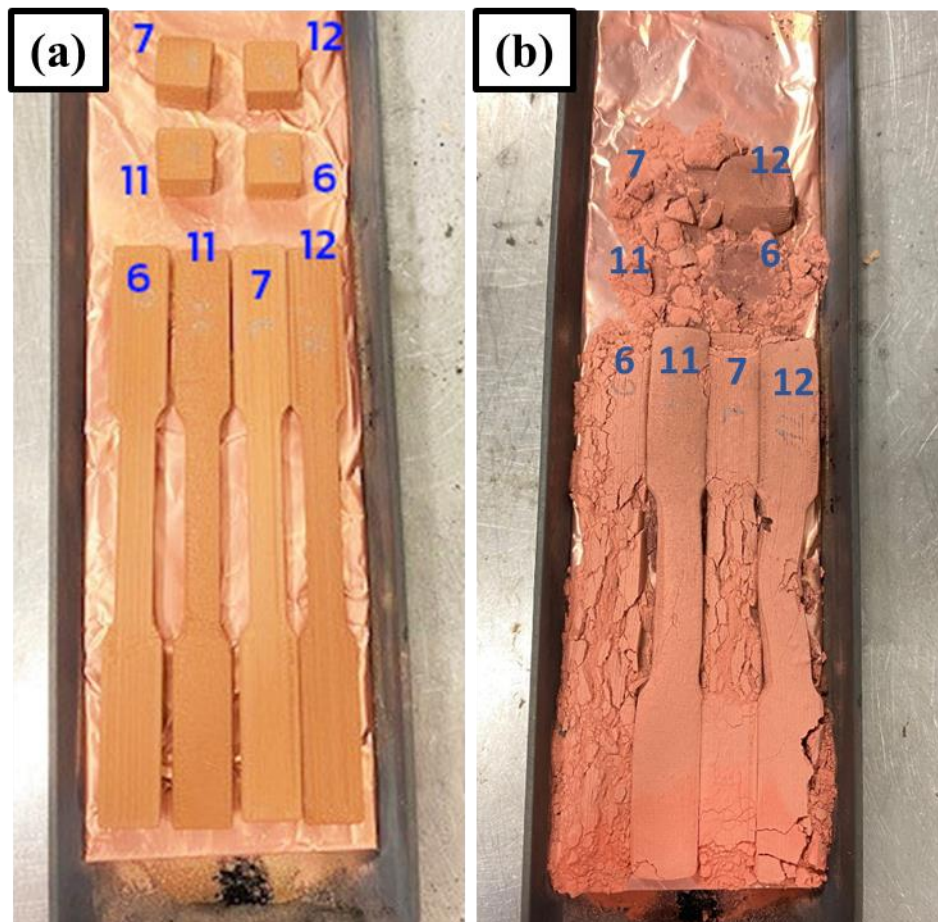
Figure E.1: *(a) 3D printer copper samples in green state (before sintering) (b) 3D printed copper samples post-sintering, where the samples were not subjected to thermal de-binding holds*

The MEX 3D printed green parts of copper were sent to SCM metal (Kymera International) for debinding and sintering. A heat treatment profile as seen in **Figure E.2** was suggested, where it was recommended that the green parts be thermally debound first with temperature holds at 280°C, 330°C, and 450°C respectively before continuing to sinter these samples at 1075°C. However, it was not feasible to change the temperature hold setting of a continuously functional industrial furnace, and hence these samples were subjected to the usual heat treatment profile that copper press and sinter parts are subjected to at Kymer International, leading to the failure of parts as seen in **Figure E.1 (b)**. Such occurrences are not unusual and neither is it unreasonable for an industrial production unit to face difficulties with changing the furnace setting for custom-made parts, especially at a small scale.
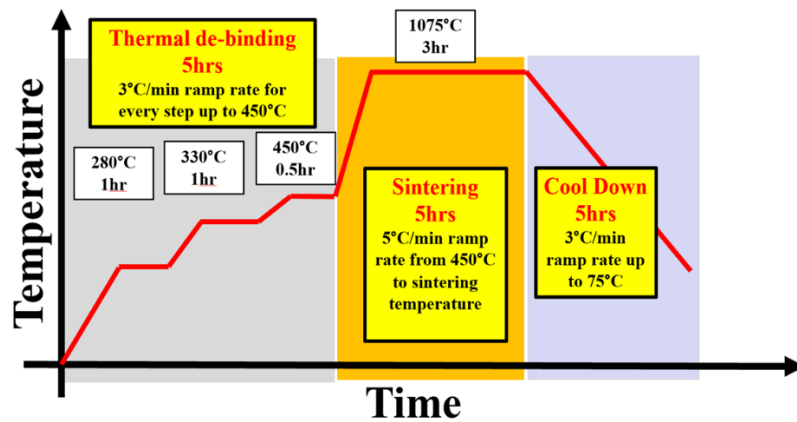
Figure E.2: Suggested heat treatment cycle involving thermal debinding and sintering for 3D printed copper samples

To resolve this problem and overcome the limitations in adapting MEX 3D printed parts for post-processing at industrial-scales, an innovative solvent-debinding step was proposed. Solvent debinding is a pre-heat treatment step typically performed by immersing the green part in a solvent, while ensuring partial removal of the polymeric binder system

and assisting in the creation of pathways for the remaining binder system to escape the part during thermal debinding.

A variety of solvents were tried and tested to analyze the effect of each solvent on the polymer binder system used and it's efficiency in eliminating parts of the multi-component binder system. As seen in **Figure E.3**, thermogravimetric analysis was performed on the green part as well as parts subjected to solvent debinding by heptane and heptane followed by methyl ethyl ketone (MEK).
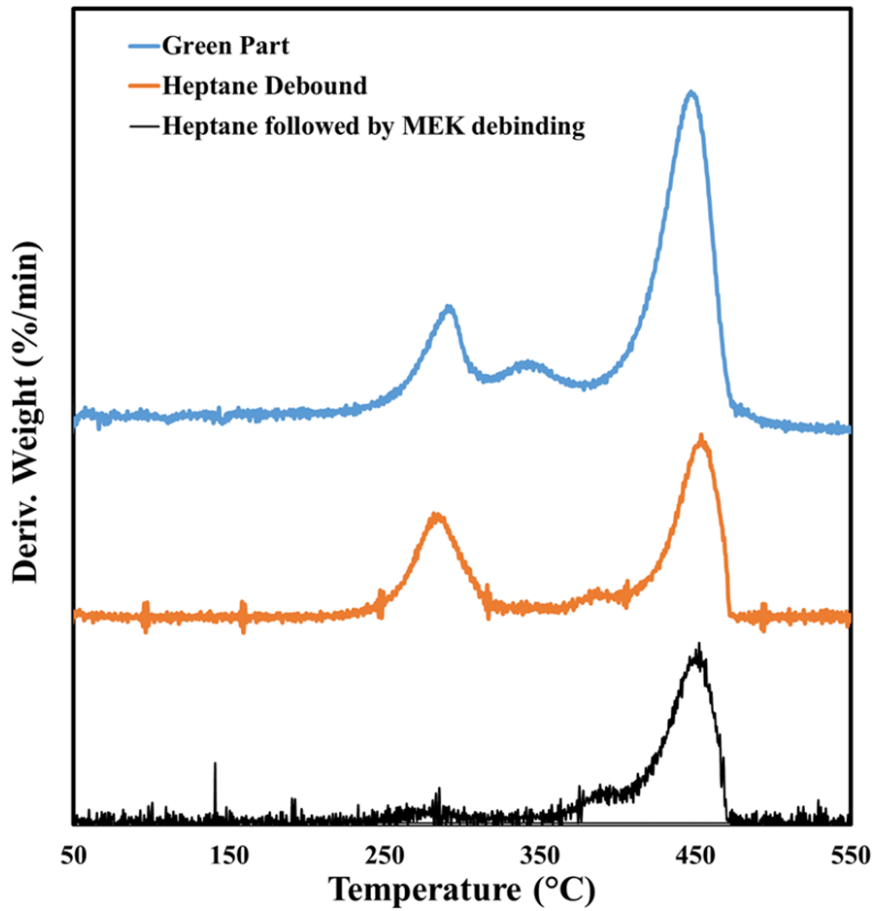
Figure E.3: Thermogravimetric analysis of 3D printed copper samples in their green state (blue), post solvent debinding in heptane (orange), and debinding in heptane followed by secondary debinding in MEK (black)

138

It was observed that the parts subjected to subsequently solvent debinding my heptane and MEK showed only one peak at 450°C, representing the need for a single step thermal debinding as opposed to a three-step thermal debinding for green parts without any solvent debinding. This was seen to have the potential to reduce the post-processing heat treatment lead times by up to 3hours, thereby making it feasible for this technology to be adopted for industrial heat treatment processes.

In addition to thermal debinding and sintering temperatures and holds during the post-printing heat treatment of 3D printed green parts, it was observed that the implementation of pre-sintering holds (after thermal debinding) could be crucial in densification and part property variations. This phenomenon was observed while processing pure copper feedstocks (58vol.% solids loading) under different heat treatment regimes. The addition of secondary debinding and pre-sintering holds as seen in **Figure E.4** was seen to change the grain refinement and densification, as opposed to samples that were heat treated without these additional pre-sintering holds (using the regime in **Figure E.2**).
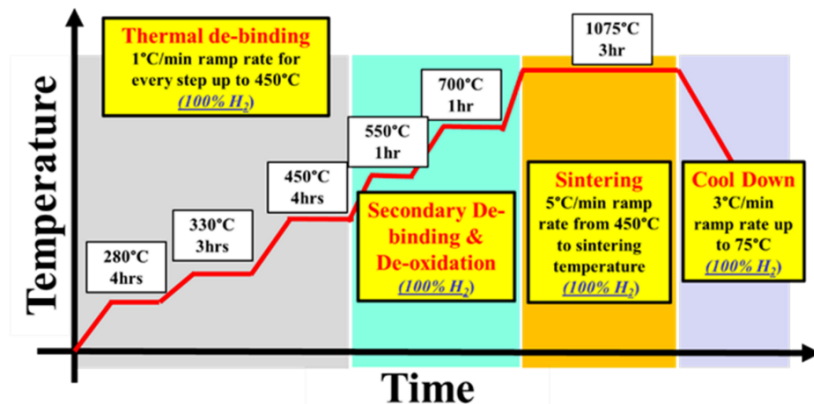
Figure E.4: *Heat treatment profile incorporating thermal debinding and intermediate pre-sintering holds for processing 3D printed copper samples*
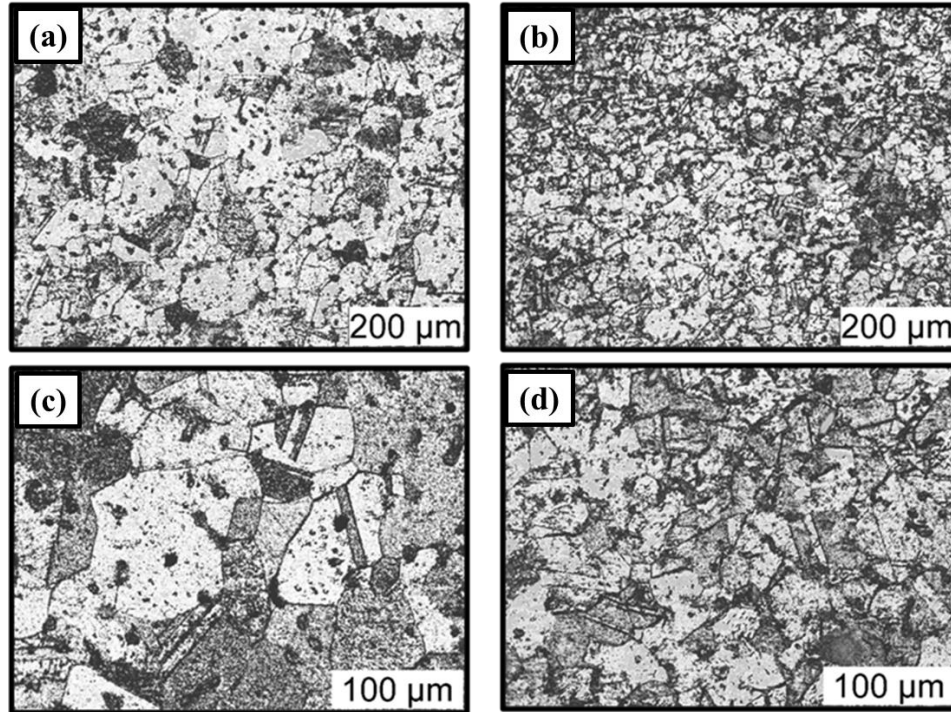
Figure E.5: *(a),(c) Microstructure of 3D printed and sintered copper samples heat treated without intermediate pre-sintering hold (b), (d) Microstructure of 3D printed and sintered copper samples heat treated with intermediate pre-sintering holds at 550°C and 700°C*

MEX 3D printing, although being a multi-step and process-intensive technology was found to offer control over the final part microstructure, which can in-turn help engineer the final part properties according to the required applications. Such control and understanding of the structure-property-processing co-relationships in metal 3D printing via MEX could help unfold novel applications for materials commonly used in the powder metallurgy (PM) and additive manufacturing (AM) industries.

F. Appendix F: Addressing Material Agnostic Challenges In MEX 3D Printing Using Infill-Based Design Strategies

Copper heat sinks are typically manufactured using conventional techniques such as bonding, forging, folding, skiving, or machining. Such heat sinks tend to have simple

fin/pin structures, partly attributed to the limitations of conventional processing technologies. In an effort to transform these traditional designs, intricate lattice designs of high surface area were 3D printed and sintered via Material extrusion additive manufacturing (MEX) process. MEX utilizes powder-filled polymer filaments with a combined Fused filament fabrication (FFF) and sintering processes to fabricate complex metallic or ceramic structures (**Figure E.1**).
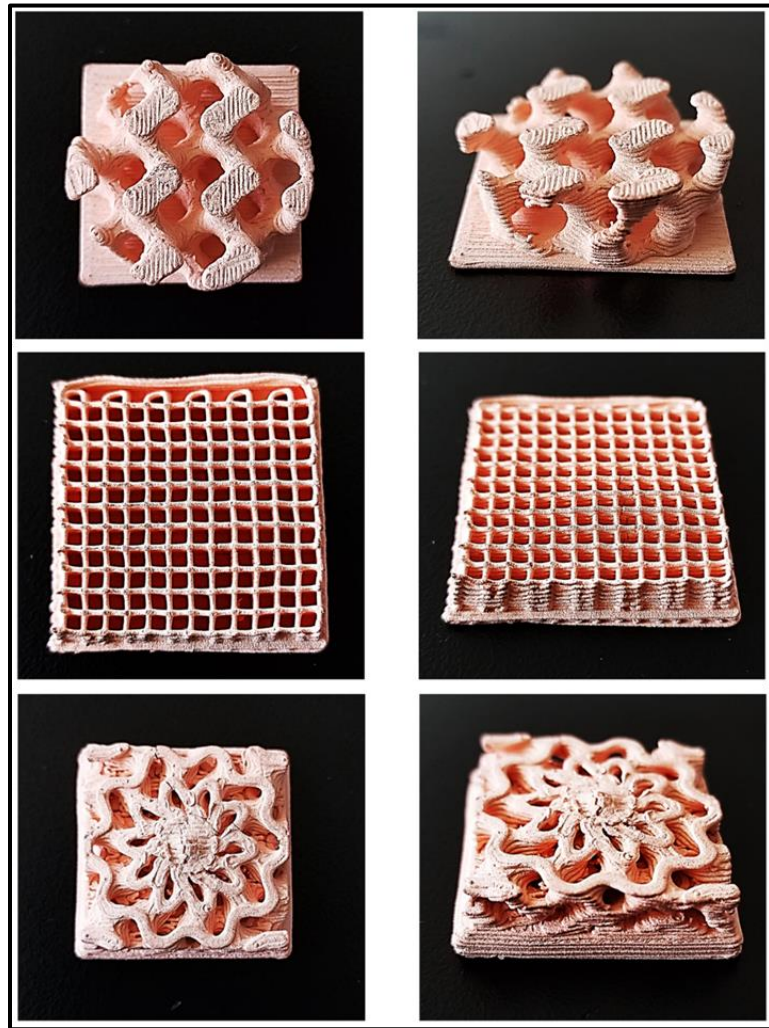
Figure F.1: *3D printed and sintered pure copper heat sinks of intricately designed lattice structures*

Although MEX 3D printing offers a great degree of design freedom as compared to it traditional manufacturing counterparts, it also suffers from certain limitation due to the nature of the processing technique involving post-printing debinding and sintering steps. It was identified that thick and thin features in parts such as heat sinks tend to debind at different rates causing cracking and part failure. This differential behavior posed challenges with retaining part integrity post debinding and sintering inspite of the ability to 3D print green parts of complex geometries (**Figure E.2**).
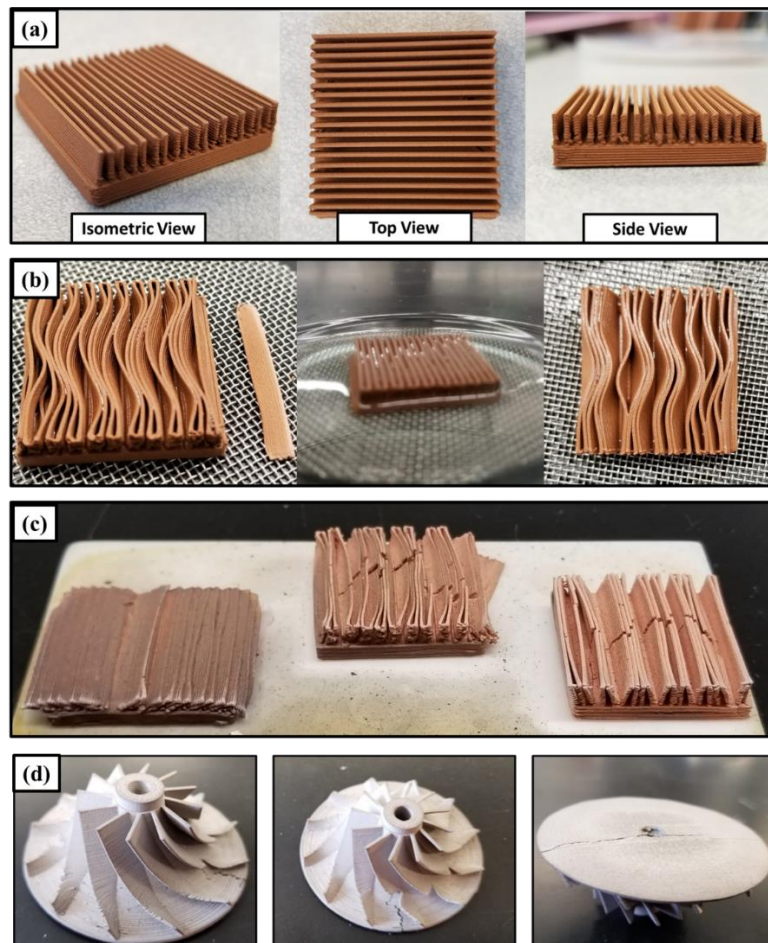
Figure F.2: *(a) MEX 3D printed fin-type copper heat sink in its green state (isometric, top, and side view) (b) MEX 3D printed green heat sink with thick base and thin fins after solvent debinding (c) MEX 3D printed copper heat sink with thick base and thin fins after sintering (d) Prototype of an MEX 3D printed Ti-6Al-4V impeller with thick base and thin fins, after sintering (part fabricated by Dr. Paramjot Singh)*

It was identified that such challenges in 3D printing, debinding, and sintering complex shaped parts successfully required implementation of design strategies and consideration while keeping in mind the post-printing processes involved with MEX 3D printing. Therefore, the reliability and scope of 3D printing infill structures using this technology was explored.
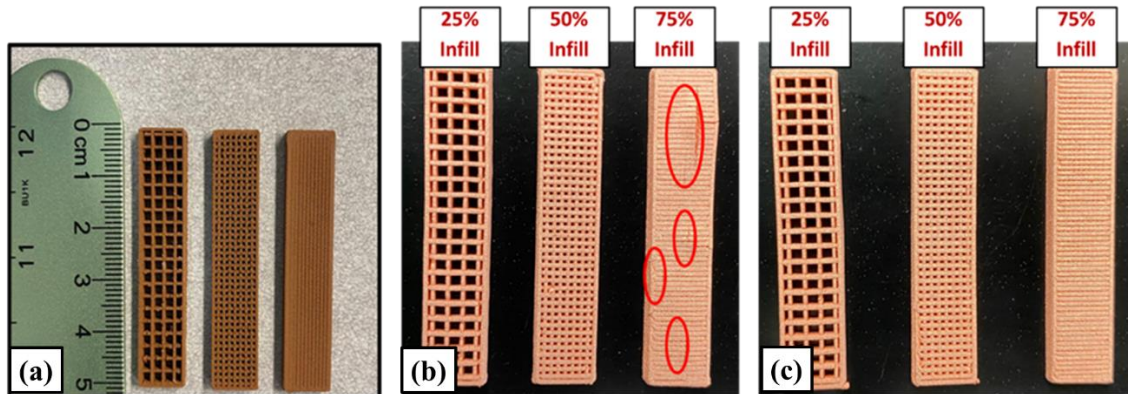
Figure F.3: *(a) 3D printed copper infill structures in their green state at 25%, 50% and 75% infill respectively (b) Copper infill structures sintered directly without prior solvent/thermal debinding (c) Copper infill structures that underwent solvent debinding followed by thermal debinding and finally sintering*

The objectives of this study were to check if the density, shrinkage, and mechanical properties of the coupons processed via the direct sintering route (without solvent and thermal debinding) and with solvent + thermal debinding followed by sintering route for the same infill were the same. Additionally, the effect of change in infill density leading to part warpage and defects (incomplete binder removal or part cracking post-sintering) in direct sintering versus solvent and thermal debinding before sintering was studied.

Table F.1: *Amount of binder lost in 3D printed copper infill structures during solvent debinding*

	25% Infill		50% Infill		75% Infill	
	Solvent + Thermal	Direct Thermal	Solvent + Thermal	Direct Thermal	Solvent + Thermal	Direct Thermal
Binder Loss %	46.10%	N/A	45.50%	N/A	45.30%	N/A

Table F.2: *Table outline relative density and part shrinkage after sintering 3D printed copper infill structures processed via different processing techniques*

		% Relative Density	% X Shrinkage	% Y Shrinkage	% Z Shrinkage
25% Infill	Direct Thermal	75.5 ± 11.0%	14.6 ± 0.3%	15.0 ± 1.8%	17.2 ± 2.6%
	Solvent + Thermal	83.8 ± 2.9%	15.2 ± 0.5%	16.6% ± 1.5%	16.5 ± 3.3%
50% Infill	Direct Thermal	81.8 ± 2.1%	14.8 ± 0.1%	17.3 ± 1.4	17.3 ± 1.2%
	Solvent + Thermal	84.9 ± 1.9%	15.3 ± 0.4%	14.2 ± 3.7%	13.6 ± 3.1%
75% Infill	Direct Thermal	75.1 ± 1.9%	12.8 ± 0.5%	-0.6 ± 1.9%	-29.5 ± 7.5
	Solvent + Thermal	87.0 ± 1.9%	14.9 ± 0.4%	15.2 ± 0.6%	12.9 ± 1.4%
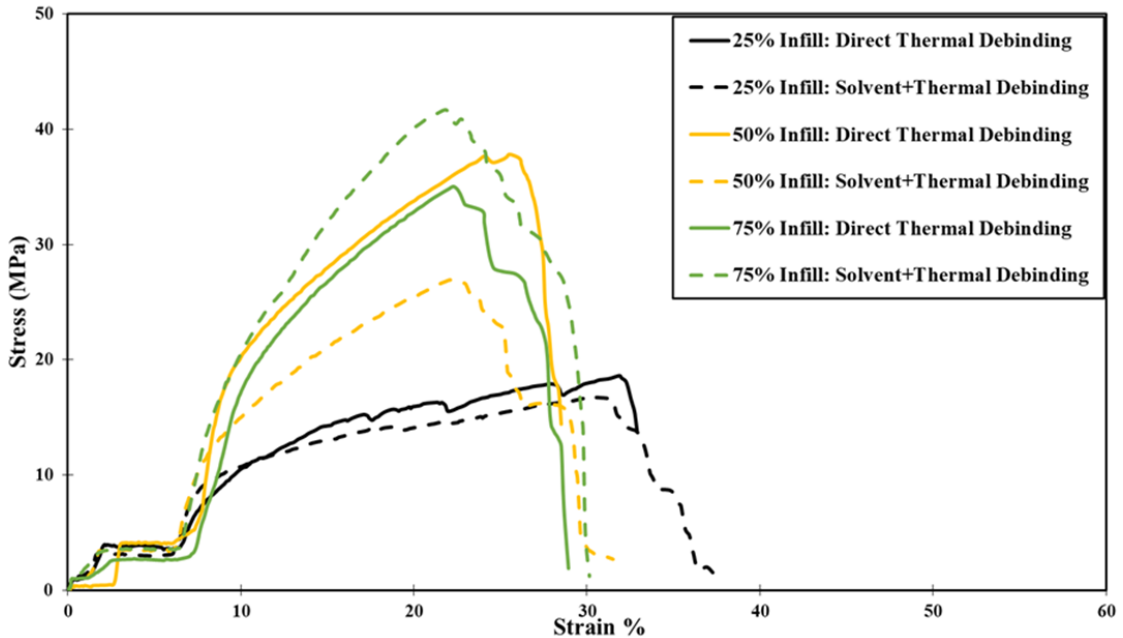
Figure F.4: *Stress vs. strain plot from tensile testing 3D printed and sintered copper infill structures processed under different conditions*

G. Appendix G: NASA-FabLab Project: Microstructure Analysis and Fractography of 3D printed and Sintered Ti-6Al-4V Density Cubes and Spent Tensile Dog-Bones

This work was performed as a part of the NASA-FabLab project, in collaboration with Techshot (now acquired by Redwire). In this project, Ti-6Al-4V parts were 3D printed using a paste-based technology by Techshot, while studying the feasibility of on-demand manufacturing of metal parts in-space. The 3D printed parts were then subjected to different sintering regimes – samples sintered at 1050°C and 1150°C, and these sintered samples were sent out to the University of Louisville for further characterization.

These as-received samples were tested characterized using XRD analysis for chemical composition and phase analysis, as well as polished, etched and looked under a

microscope to understand the grain structure and it's variation with different sintering profiles. Additionally, sintered dog-bones that were tensile tested by Techshot were sent to UofL for fractography analysis to identify the type of fracture and the presence of any abnormalities along the crack wake.
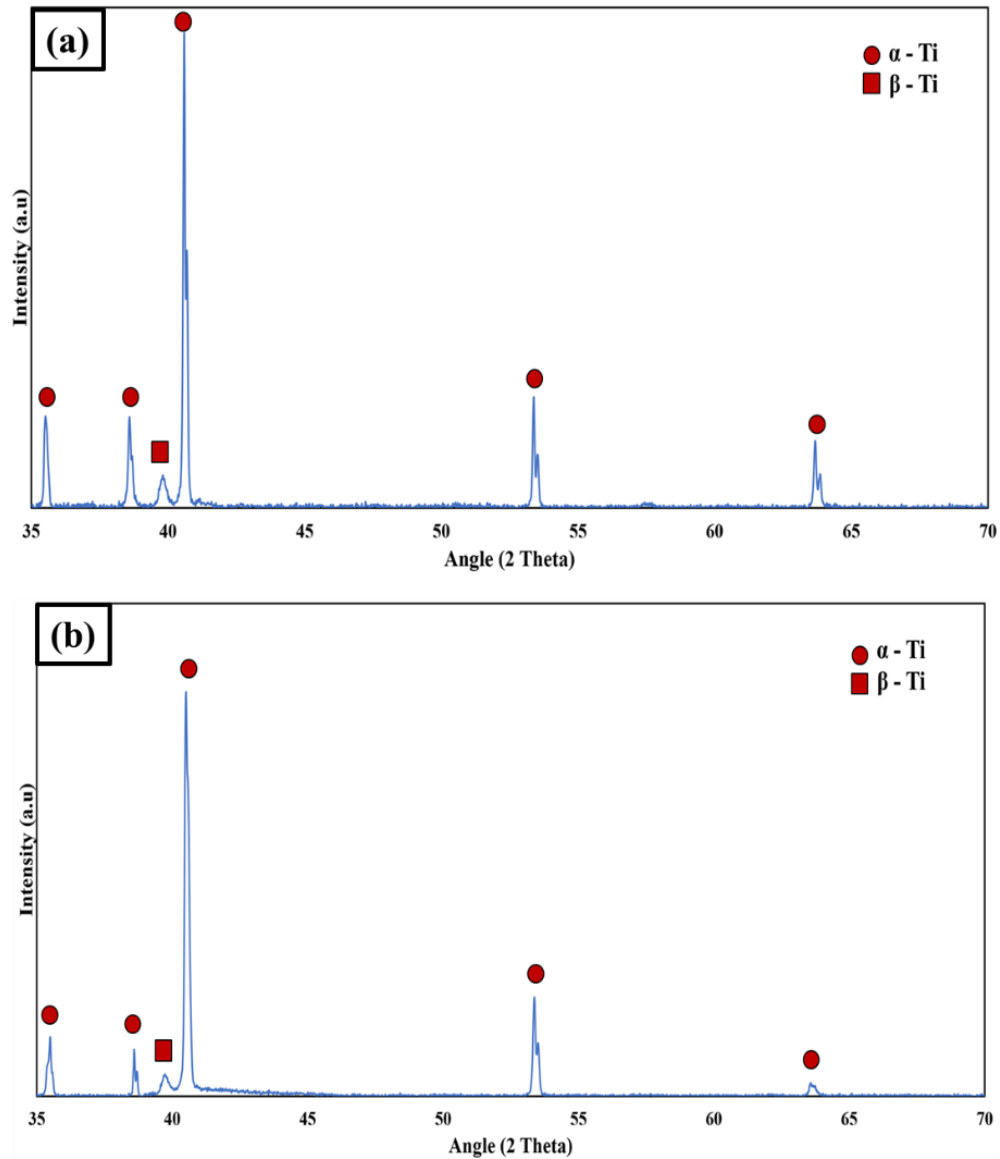
Figure G.1: *XRD analysis of 3D printed Ti-6Al-4V samples sintered at (a) 1050°C and (b) 1150°C*
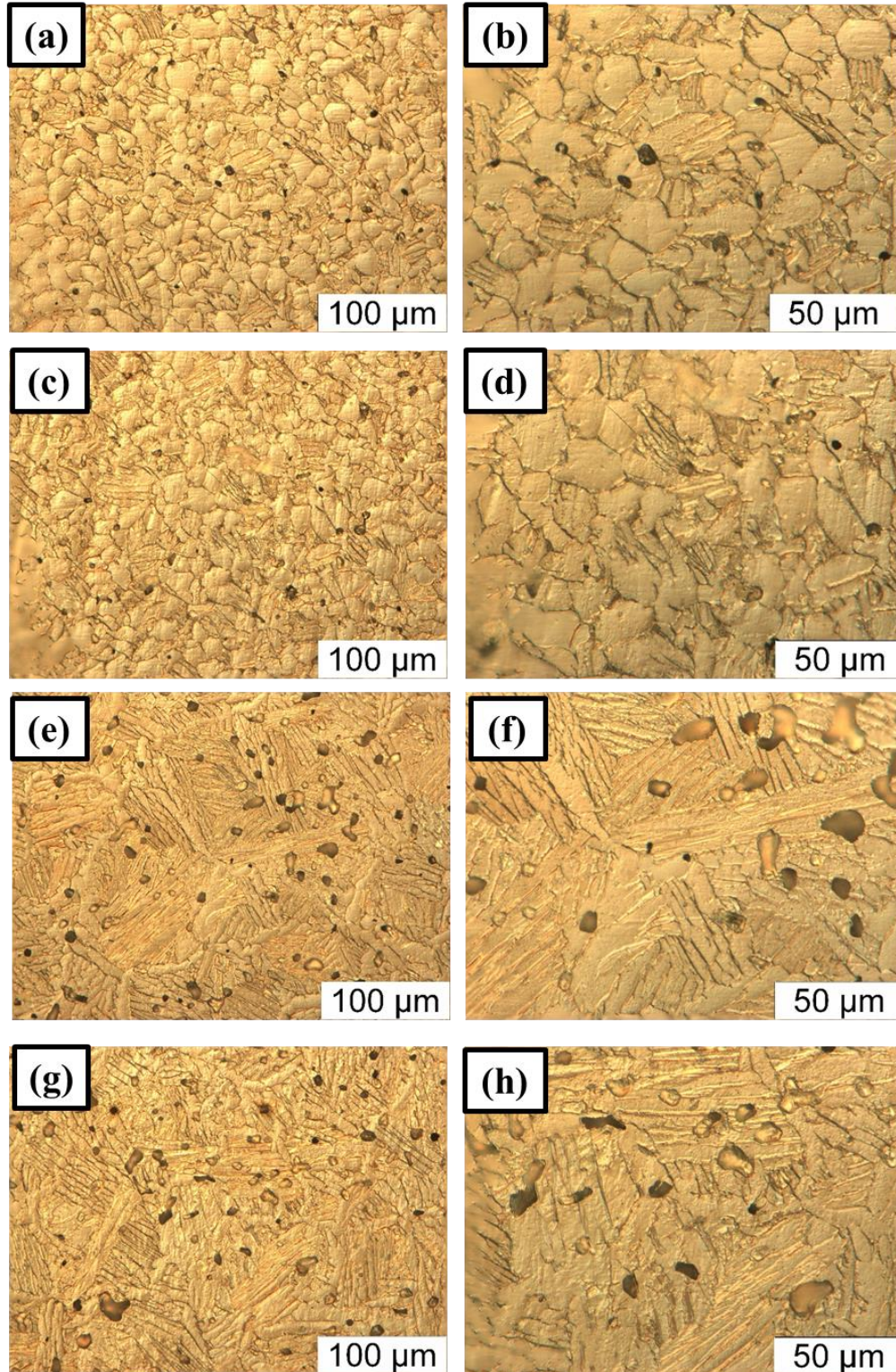
Figure G.2: *Etched microstructure of 3D printed Ti-6Al-4V samples sintered at (a, b)*
1050°C; XY cross-section (c, d) 1050°C; XZ cross-section (e, f) 1150°C; XY cross-section
(g, h) 1150°C; XZ cross-section
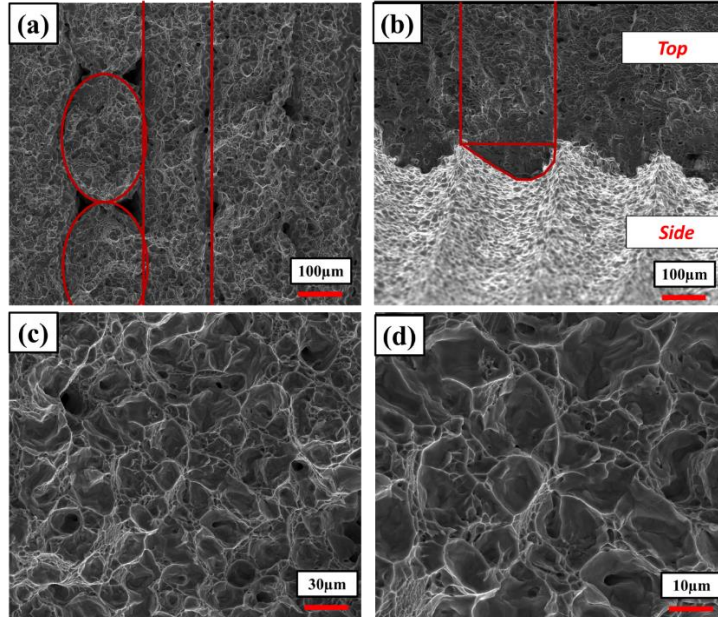
Figure G.3: (a) SEM image depicting struts and layers from 3D printing (b) SEM image showing the side and top of the fractured 3D printed sample (c, d) Fracture surface of spent tensile dog-bones of 3D printed Ti-6Al-4V samples at 1500X and 3000X respectively (all images are from samples sintered at 1150°C)
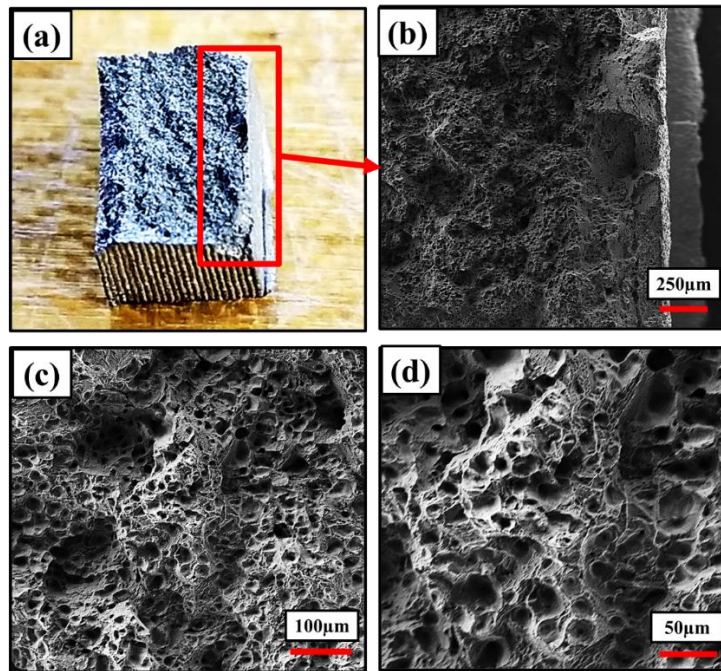
Figure G.4: (a) Photograph of the fracture surface of 3D printed Ti-6Al-4V spent tensile dog-bone sintered at 1150°C (b, c, d) SEM images of the fracture surface at 150X, 500X, and 1000X respectively

H. Appendix H: Soy-Terrazzo Project: Bio-Based Alternatives To The Carbon-Intensive Petroleum-Based Flooring And Construction Industry

Thermoset resins found applications in multiple industries over the last century, with construction industry being the leading consumer. Terrazzo is one such thermoset resin that is abundantly used for construction today. A majority of these thermoset resins are petroleum-based with high carbon footprint, which is not only detrimental to environment but also not sustainable. Moreover, COVID-19 pandemic along with other unfortunate events in world politics had its effect on the global supply chain, thereby demanding more sustainable and renewable raw materials. One such bountiful and under-utilized natural resources: soybean-based resins, were found to be promising.

In this work soy-based coatings/sealers were seen to perform better mechanically (2-10times) and chemically, compared to petroleum-based coatings/resins. Additionally, soybean-based resins were successfully used instead of petroleum-based epoxy resins in tiles filled marble chips. Finally, marble chips were also replaced with 3d printed chip-shaped geometries made of soybean-based resin. American market research projects that epoxy resins market will hit 12.8 billion in 2030 [108,109]. Every year 10 billion tons of petroleum-based resin is needed for construction projects [108,109]. Incorporating even 1 million tons of soybean-based resin this translates into soyhulls derived from 60 million bushels of soybean. Soybean-based resins are economically viable at a low cost of $0.36/kg to acquire them. Additionally, they are EN 71-3:2013 safety standard compliant, because of no VOCs, BPAs, or harmful chemicals. The technological findings from this work, along

with results from cost & market analysis opens-up a viable, sustainable, and lucrative business opportunity for utilization of soybean-based resins in the construction industry.
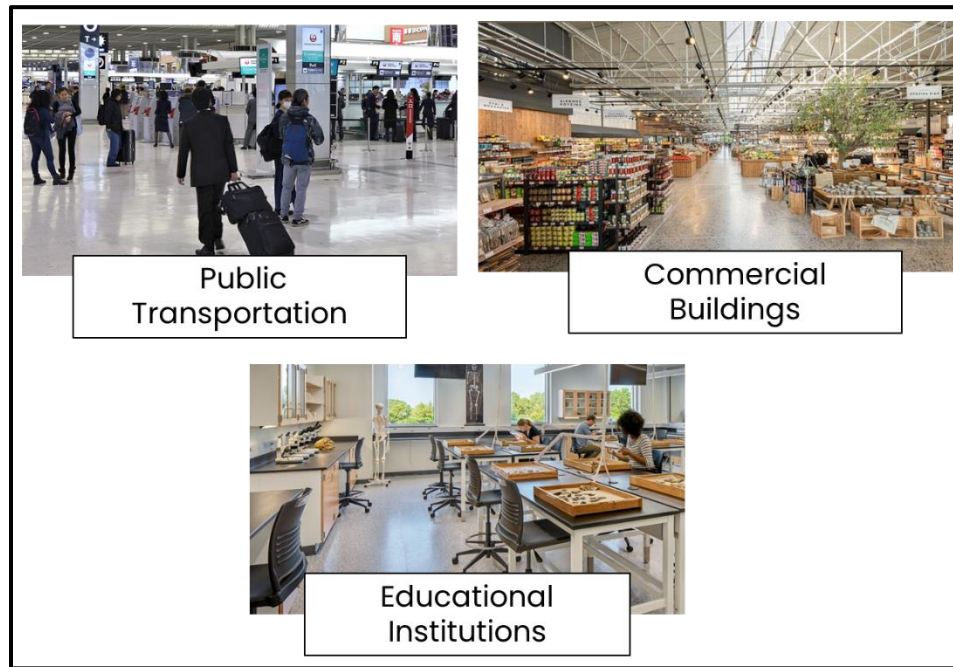
Figure H.1: Representative image depicting the widespread use of petroleum-based terrazzo tiles in transportation, commercial, and educational infrastructure

Epoxy resin extracted from soybean have possible applications beyond traditional terrazzo tiles due to its renewability, sustainability, physically properties modifiability and its wide range manufacturability. The product portfolio includes, but is not limited to:

- Sealers and coatings from soybean oil

- Epoxy resin from soybean oil

- Terrazzo tiles from soybean resin

- 3D Printing Artistic Geometries for structure applications from soybean UV

On a broad level, tiles used for floorings are comprised of the coating/sealent that protects the surface of the tile, an epoxy-based resin that hardens with curing and holds the individual marble chips and other decorative materials, as shown in **Figure H.2**.
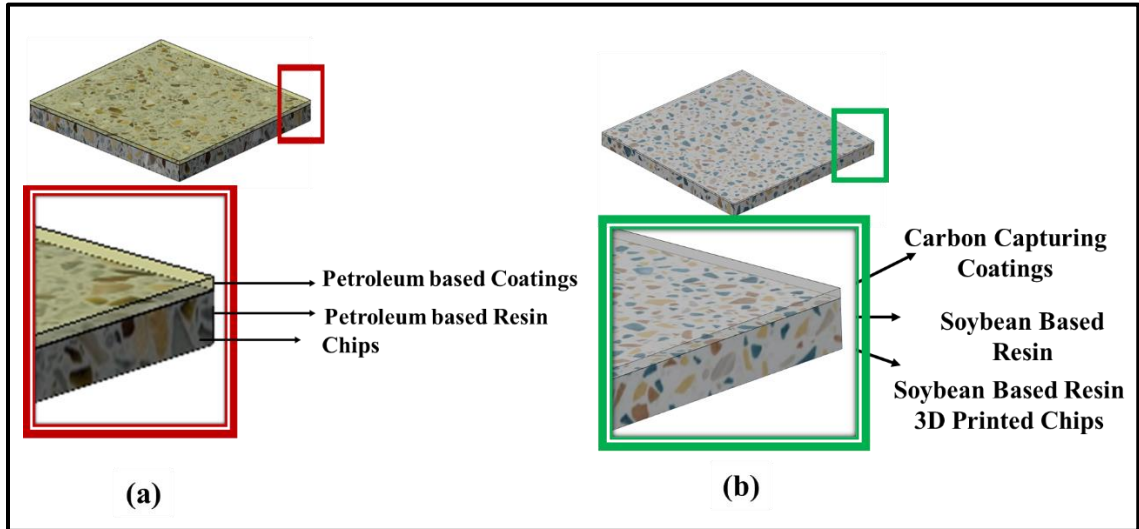
Figure H.2: *Simplified depiction of the major components in a flooring tile – coatings, resins, and decorative chips for (a) petroleum-based terrazzo tiles that are currently in use (b) bio-based soy resin tiles proposed in this study*

The effect of epoxidized soybean oil (ESO) to Terrazzo resin and hardener mixture was studied. Addition of different amounts of ESO was performed to identify the limiting capability (if any) and also to understand the effect of higher ESO content. Initially, 5% and 10% (by weight) of ESO was added to the epoxy and hardener mixture acquired from Venosa LLC. The ratio of petroleum-based epoxy and hardener that was used was kept consistent to the usual concentrations of each component used to prepare cast tiles. Considering the huge volume of petroleum-based epoxies and hardeners that are used in the construction industry, a 5-10% share of the market amounts to a huge chunk of soybean-based resin consumption.

Curing time plays a crucial role in casting two-component resins as the epoxy hardener mixture generate a lot of heat because of the exothermic reaction during curing. The (reasonably) longer it takes to cure a mixture of epoxy and hardener, the lower the amount of heat generated. Moreover, the extra time provides an opportunity for the solution

151

to take shape and release any bubbles or air pockets that might have formed during casting. This essentially helps in the production of defect-free casting, reducing the overall wastage and overhead charges, although it might take slightly longer for part production. Addition of ESO in amounts as small as 5% was seen to slow down the curing process (**Figure H.3**), providing ample time for setting the mixture and giving it the required shape. It would be interesting to analyze the increase in curing time with addition of ESO and identify a limiting ESO content beyond with the curing time stabilizes.
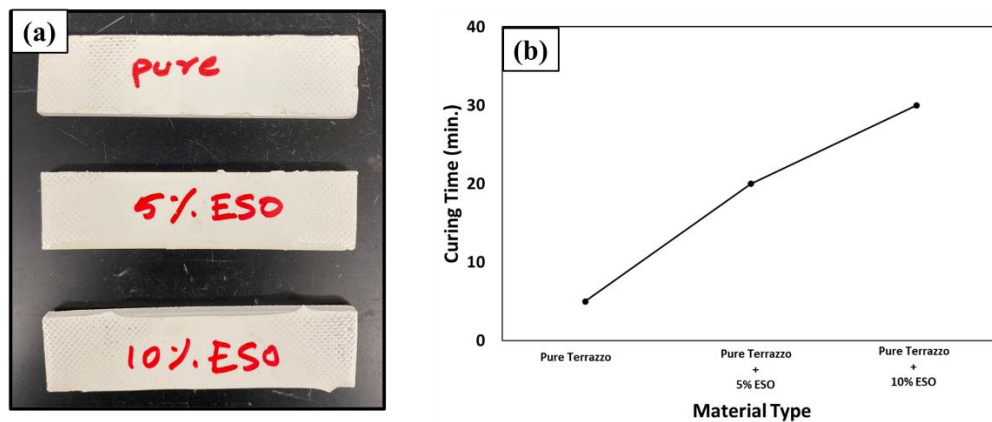
Figure H.3: (a) cast samples of pure terrazzo (resin + hardener), Terrazzo mixture with 5wt.% epoxified soy bean oi (ESO)l, and terrazzo mixture with 10wt.% ESO (b) Plot depicting the curing time for each sample

Mechanical testing of coupons cast using different mixtures of pure Terrazzo formulations and Terrazzo mixed with ESO was performed and analyzed. It was observed that the Modulus, Maximum Strength, and Maximum Strain that a sample can withstand increased slightly with an addition of 5% ESO (**Figure H.4**). The stress-strain plots of all three types of mixtures clearly indicate that an addition of 10% ESO has a distinct effect on the stiffness and the ultimate strength of the cured material. The increase in stiffness is evident in reduction in % Strain or elongation of the samples before failure. All three materials were seen to fail abruptly, indicating brittle fracture which is characteristic of most

152

thermoset resins and ceramics. The sudden drop in force/stress after a certain amount of deformation is identical to these samples. However, the area under the curve that signifies toughness of the material, or the amount of energy absorbed by the material before failure is seen to be highest for 5% ESO addition. This opens a whole new area of research that can be performed to engineer materials based on applications and fabricate products with desired properties.
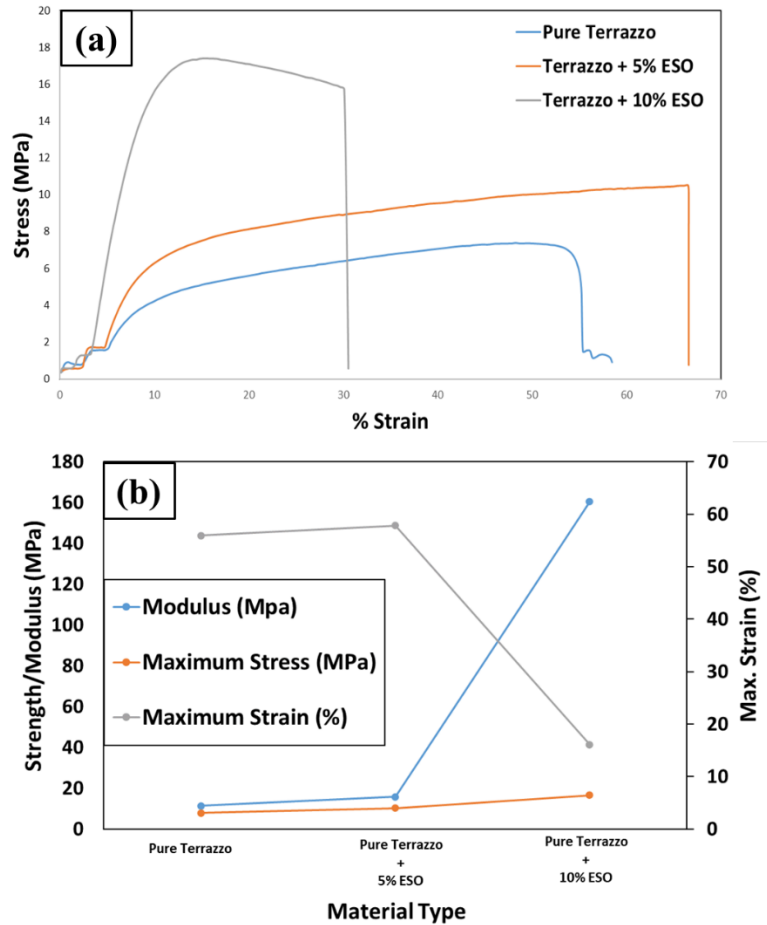
Figure H.4: (a) Stress-strain plot from tensile testing cast terrazzo and terrazzo-ESO samples (b) Plot depicting the change in elastic modulus, maximum tensile stress and maximum elongation (% strain) with addition of ESO to pure terrazzo samples

Figure H.5 summarizes the diverse end-use applications of soy-based resins in the flooring and construction industry. With soybean-based resins showing encouraging results

in potential applications as sealers and coating for terrazzo tiles, efforts were focused towards implementing soybean-based resin mixtures for fabricating and processing tiles. This will prove to be a huge step towards reducing the carbon footprint in the construction industry, considering the enormous amounts of petroleum-based resins and epoxies utilized for making tiles every year across the globe. UV curable soybean resin is utilized instead of petroleum-based resin to create terrazzo tiles. Terrazzo tiles formulation consist of epoxy resin, marble chips and sand filler. Two different approaches were conducted first approach was by simply replacing the petroleum-based epoxy resin with soybean resin and utilizing conventional marble chips and sand fillers.
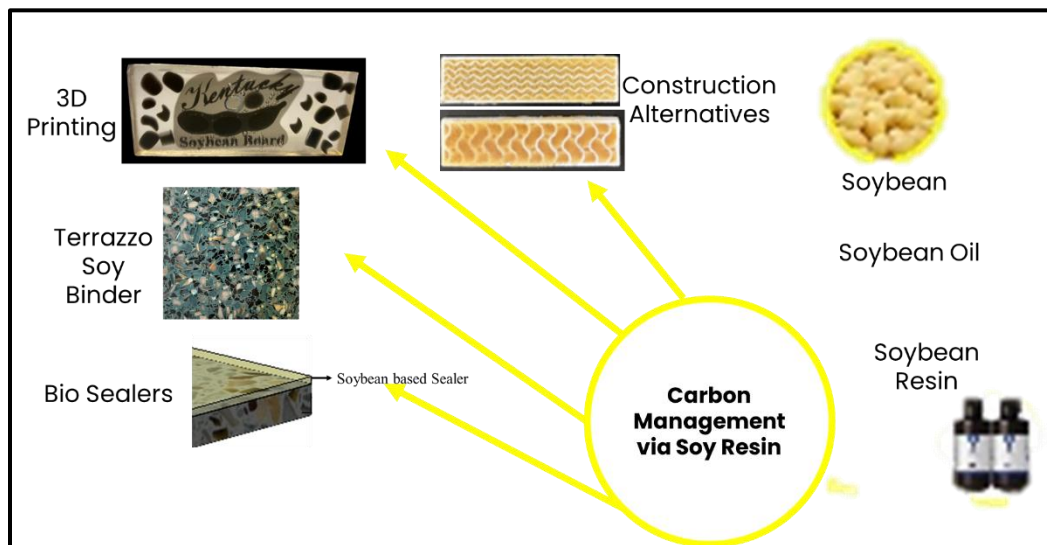
Figure H.5: *Schematic summarizing the bio-based alternative solutions proposed in this study for applications in the flooring and construction industry*

Second approach is more innovative by utilizing soybean resin in addition to replacing marble chips with stereolithography 3d printed geometries mimicking the shape of marble chips along with architectural geometries such as logos embedded in terrazzo tiles. Initial results showed abundant promise, with the ability to 3D print marble chips, logos and even intricately shaped structures with soybean-based resins. This could

154

potentially pave way for innovative designs and structures that can very easily be molded or casted into different thermoset resins at a later stage. Additionally, to take this a step further, soybean-based resins were also used to cast them into molds made using 3D printed structures with silicone castings. Since the soybean-based resins were photosensitive and can be cured using UV light, processing these tiles essentially becomes a single-step cast/cure process without the need to pre-mix epoxies and hardeners. Proper care was taken during casting to minimize air pockets and ensure adhesion between the 3D printed chips, logos, and the epoxy resin that was casted into the mold. However, tiny air bubbles did make way, especially around intricate structures such as the logo. This, however, is very easily fixable with the use of a vacuum mixer and casting equipment that we do not have access to at this point of time. Finally, this ability to fabricate tiles with such photosensitive soybean-based resins not only reduces the lead time and processing steps by half, but also aids in reducing the labor cost and post-processing treatments that typically add up to higher overhead costs in conventional tile making.

CURRICULUM VITAE
Pavan Ajjarapu

pavanajjarapu9@gmail.com / linkedin.com/ajjarapupavan / Google Scholar /

Education

University of Louisville	**2020-2023**

Louisville, KY
Doctor of Philosophy in Mechanical Engineering

University of Cincinnati	**2017-2019**

Cincinnati, OH
Master of Science in Materials Science Engineering

Visvesvaraya National Institute of Technology	**2013-2017**

Nagpur, India
Bachelor of Technology in Metallurgy and Materials Engineering

Technical Skills

Manufacturing: 3D-printing, Polymer processing, Vacuum Arc Melting, Heat treatment, Wire EDM machining.

Characterization: SEM, EDS, XRD, DSC, TGA, Metallography, Microscopy, Hardness, Pycnometry, Rheology, Tensile, Compression & 3-point bend mechanical testing, Fractography.

Tools & Software: MATLAB, Minitab, LabVIEW, ImageJ, CES Granta Edupack, BlueHill, TA Universal Analysis, Simplify3D, Repetier, Slic3r, Solidworks.

Analytical: Design of experiments (DOE), DMAIC, Taguchi Analysis, Greys Relational Analysis Analysis of variance (ANOVA), Response Surface Methodology, Statistical Process Control (SPC), and Control Plan.

Project Management: Lean Principles, 5S Standards, Phase/Stage Gate Approach, HSE Management, 5Why, 8D, FMEA, Root Cause Analysis.

Projects & Research

University of Louisville
Jul. 2020 – Present

- *On-demand manufacturing of metals for in-space applications in ISS (NASA-Techshot)*
  - · Evaluated microstructure, phase composition, & mechanical properties of sintered parts fabricated by Techshot using paste-based 3D printing for in-space manufacturing via extrusion-based 3D printing
  - · Characterized the effect of sintering temperature and brazing on mechanical properties and fracture type via microstructure and fractographic analysis

- *Adapting metal injection molding feedstocks for 3D printing non-ferrous alloy structures*
  - · Elucidated the effect of MIM parameters on homogeneous powder-filled filament properties by establishing viscosity as a function of time, temperature & shear rate.
  - · Quantified printability based on powder characteristics, packing fraction, flowability, binder properties & filament stiffness.
  - · Applied MIM feedstocks to 3D printing using models that predict material properties critical for process simulations.

- *Characterizing novel ceramic-polymer mixtures for injection molding applications (SABIC)*
  - · Performed viscosity measurements at different temperatures and shear rates for pure polymer, SABIC patented ceramic-polymer powder mixture and an admixed ceramic powder polymer pellet mixtures for potential use in injection molding applications.
  - · Investigated how feedstock homogeneity and critical solids loading of ceramic powders dry blended with a polymeric material system in various forms such as pellets and powders affect feedstock extrusion and quality using SEM and optical imaging.
  - · Discussed with SABIC for a potential future project where identification of critical solids loading, use of a multi-material binder system with low and high molecular weight polymers to achieve process-able and mixing experiments for obtaining homogeneous feedstock for SABICs patented technology ceramic-polymer powder mixture for injection molding applications.

- *Statistical analysis & predictive modeling to aid material innovation in 3D printing*
  - · Conceptualize material flow rate measurement in FFF 3D-printing to accurately estimate pressure across the nozzle by fundamental experiments & implementing mathematical models that simulate actual process conditions.
  - · Performed N-way ANOVA to investigate the effect of processing parameters on flow characteristics required to achieve high-density 3D printed parts.
  - · Developing an artificial neural network that predicts green density and feedstock viscosity with a 99% coefficient of determination, facilitating new material development.

University of Cincinnati

Aug 2017 - Jul 2019

- · Fabricated geometrically complex Ni-TiC cermet scaffolds using liquid ink extrusion 3D printing technique, with 60% macro-&micro-scale porosity attained via quartz-encapsulated vacuum sintering to assist diffusion across interfaces.
- · Conducted EDS 2D mapping and line scans to validate the elemental analysis of sintered structures and verify oxidation susceptibility in the final part.

Bhabha Atomic Research Centre

May 2015 - Jul 2015

- · Fabricated Ni-Ti alloy strips by vacuum arc melting and hot rolling, followed by characterization to study microstructure, phase transformations & shape memory behavior for application in TEJAS (India's first Light Combat Aircraft).

Patents, Publications & Conference Talks

- **Low attenuation soft and stretchable elastomeric optical waveguides (Patent pending) [Link]**
  R Uppal, **KPK Ajjarapu**, K Kate, CK Harnett —Materials Letters, Elsevier, 299, 130079

- **Addressing Powder Morphology and Filament Properties for Extending PIM Feedstocks to Fabricate Green and Sintered Alumina Parts via Ceramic Fused Filament Fabrication (CF3)**
  KPK Ajjarapu, K Sudan, P Singh, K Kate —Additive Manufacturing with Powder Metallurgy, 227-240

- **Characterization of Industry Grade Soybean Wax for Potential Applications in Natural Fiber Reinforced Composite (NFRC) Filaments**
  A. Surendran, **KPK Ajjarapu**, AA Akilan, K Kate, J Satyavolu —Industrial Crops and Products, Elsevier, Vol.186

- **Barocaloric Properties of Thermoplastic Elastomers.**
  N. Weerasekera, **KPK Ajjarapu**, K. Sudan, G. Sumanasekera, K. Kate, B. Bhatia - Frontiers in Energy Research 10, 887006

- Adapting Metal Injection Molding Feedstocks for 3D Printing of Ti-6Al-4V Alloy Structures via Metal Fused Filament Fabrication (MF3). Metal Injection Molding Association (MIMA), Feb 2021

- Process Maps and Models For Highly Filled Polymers in Powder Fused Filament Fabrication (PF3) 3D Printing. Materials Science and Technology (MS&T), Oct 2021.

- Effect of Particle Morphology & Green Part Density on Microstructure Evolution & Mechanical Properties of Sintered Alumina Fabricated via CF3. Materials Science and Technology (MS&T), Oct 2021.

- Adapting Metal Injection Molding (MIM) Feedstocks for 3D Printing of Non-Ferrous Alloys via Metal Fused Filament Fabrication (MF3). Metal Injection Molding Association (MIMA), Feb 2022.

- Generative Design and Topology Optimization based 3D printing via Metal Fused Filament Fabrication (MF3). Additive Manufacturing and Powder Metallurgy (AMPM), Jun 2022.

Leadership & Awards

- Materials selection & processing consultant at the Advanced Manufacturing Center (AMC) for Minority Business Development Agency (MBDA) in Kentucky.
- Winner of the 2022 Soy Innovation Challenge, organized by the Kentucky Soybean Board, hosted in conjunction with the Conn Center for Renewable Energy Research.
- Graduate student representative of the Mechanical Engineering department in the student council at UofL.
- NSF Graduate Student Award recipient for PowderMET2022 conference.
- Two-time recipient of the Metal Injection Molding Association Graduate Student Conference Grant (2021 and 2022).
- Six Sigma Green Belt certification granted by IISE (ID: 48708528).